

# Logic gates realized with spin dependent tunneling elements

Dissertation zur Erlangung des Doktorgrades  
der Naturwissenschaften (Dr. rer. nat.)  
der Fakultät für Physik  
Universität Bielefeld

Vorgelegt von  
Ralf Richter

September 2002

Gedruckt auf alterungsbeständigem Papier °ISO 9706

# Acknowledgements

I express my thanks to all friends and colleagues which accompanied me in the last years and which contributed to the success of this work.

First of all I express my thanks to Prof. Dr. Günter Reiss for his guidance and advice on this thesis. I thank also my supervisor at Siemens, Dr. Joachim Wecker, for giving me the opportunity to make this unique work. Furthermore I thank Prof. Dr. Herbert Schewe from Siemens in Erlangen, who supported this work financially and who made it possible for me to present most of this work at conferences.

My special thanks goes to Dr. Hugo van den Berg, Dr. Hans Boeve and Dr. Manfred Rührig for stimulating discussions during the last three years.

I am especially grateful to Dr. Ludwig Bär for supporting me with the fabrication of logic gates.

I also appreciate the valuable collaboration at Siemens with Dr. Günther Gieres, Dr. Günther Rupp and Mr. Michael Vieth and the technical support by Mr. Karl-Heinz Rojek and Ms. Elena Volkova.

I acknowledge very much the discussions and encouragement from my friends and colleagues in Erlangen: Dr. Silviu Colis, Dr. Theodoros Dimopoulos, Dr. Karin Eggers, Mrs. Laurence Esparbé, Dr. Ulrich Klostermann, Mr. Olivier Mathieu and Dr. Stephane Zoll. I am also grateful to all my colleagues from the University of Bielefeld, the University of Strasbourg and the University of Nijmegen.

I am very much indebted to Kursat Bal from the University of Nijmegen for initiating my work on programmable magnetic layers (Ru/CoFe).

Special thanks goes to Sonja Heitmann at the University of Bielefeld for providing me with X-ray measurements on the Ru/CoFe samples. I am also grateful to Dr. Hubert Brückl for AFM measurements, to Mrs. Liliana Roch for supporting me during the MOKE measurements, to Mr. Ramana Jelda for programming in Lab-View, to Mr. Ralf Kinder for the support in measurement issues and to Dr. Joachim Bangert for unbelievable discussions.

Thanks goes also to my colleagues from other groups in Erlangen: Dr. Jens Hauch, Mr. Karl Hauser, Mrs. Agathe Hempel, Dr. Rainer Leuschner and Dr. Gotthard Rieger.

Finally, I thank my parents and all my family who were always present when I needed them.



# Contents

|          |  |           |
|----------|--|-----------|
| <b>1</b> | <b>Introduction</b>  | <b>1</b>  |
| <b>2</b> | <b>Theory</b>  | <b>5</b>  |
| 2.1      | Theory of spin dependent tunneling . . . . .   | 5         |
| 2.1.1    | Quantum mechanical tunneling . . . . .   | 5         |
| 2.1.2    | Spin dependent tunneling and magnetoresistance . . . . .                                 | 7         |
| 2.1.3    | Major loop and minor loop . . . . .  | 11        |
| 2.2      | Switching behaviour of thin magnetic films . . . . .                                     | 12        |
| 2.2.1    | The total free energy of a ferromagnetic body . . . . .                                  | 12        |
| 2.2.2    | Single domain switching behaviour . . . . .  | 14        |
| 2.2.3    | Magnetic coupling in SDT elements . . . . .  | 15        |
| 2.3      | Design of SDT stacks . . . . .   | 18        |
| <b>3</b> | <b>Magnetic logic</b>  | <b>23</b> |
| 3.1      | Programmable logic based on magnetoresistance . . . . .                                  | 24        |
| 3.1.1    | Mask programmable logic . . . . .  | 25        |
| 3.1.2    | Astroid-logic . . . . .  | 28        |
| 3.1.3    | PML-logic . . . . .  | 30        |
| 3.1.4    | Spin-logic . . . . .   | 32        |
| <b>4</b> | <b>Sample patterning and Measurement</b>   | <b>39</b> |
| 4.1      | Fabrication process of spin-logic gates . . . . .  | 39        |
| 4.2      | Electrical transport measurement . . . . .   | 46        |
| 4.2.1    | 2-point and 4-point measurements . . . . .   | 46        |
| 4.2.2    | Experimental setup . . . . .   | 47        |
| <b>5</b> | <b>Spin-logic based on SDT elements</b>  | <b>49</b> |
| 5.1      | Requirements for the feasibility of spin-logic . . . . .                                 | 49        |
| 5.2      | The first working spin-logic gate . . . . .  | 50        |
| 5.3      | The feasibility of spin-logic gates realized with micron sized SDT<br>elements . . . . . | 54        |

|          |   |            |
|----------|---|------------|
| 5.4      | Judgement on tunneling systems with respect to working spin–logic gates . . . . .                               | 58         |
| 5.4.1    | Monte–Carlo simulation . . . . .  | 61         |
| <b>6</b> | <b>Aspects of the switching behaviour</b>   | <b>65</b>  |
| 6.1      | Shape anisotropy . . . . .  | 65         |
| 6.1.1    | Theoretical aspects . . . . .   | 65         |
| 6.1.2    | Impact of the shape on the minor loops . . . . .  | 68         |
| 6.1.3    | Impact of the reference layer system . . . . .  | 71         |
| 6.2      | Measurement of astroids . . . . .   | 72         |
| 6.2.1    | Determination procedure of an astroid . . . . .   | 72         |
| 6.2.2    | Deviations of the measured astroids from the Stoner and Wohlfarth theory . . . . .                              | 73         |
| 6.2.3    | Impact of the shape anisotropy on the astroid . . . . .   | 76         |
| <b>7</b> | <b>Programmable reference layer</b>   | <b>81</b>  |
| 7.1      | Calculation of magnetic fields versus currents on–chip . . . . .  | 81         |
| 7.1.1    | Cross–talk in spin–logic gates . . . . .  | 84         |
| 7.2      | Programmable reference layer system Ru/CoFe . . . . .   | 87         |
| 7.2.1    | Finite thickness effect of the Co <sub>50</sub> Fe <sub>50</sub> reference layer on the Néel coupling . . . . . | 93         |
| <b>8</b> | <b>Magnetic stability</b>   | <b>97</b>  |
| <b>9</b> | <b>Summary and outlook</b>  | <b>105</b> |
|          | <b>References</b>   | <b>107</b> |
|          | <b>Curriculum Vitae</b>   | <b>114</b> |
|          | <b>List of publications and presentations</b>   | <b>117</b> |





# Chapter 1

## Introduction

The use of magnetoresistive thin film magnetic structures is expected to improve existing electronic devices. In contrast to purely semiconductor based devices, magnetoelectronics utilizes the charge and the spin of the electrons.

There are several magnetoresistive effects, of which some are already used in industrial products.

The anisotropic magnetoresistance (*AMR*) was first observed in 1857 [1]. The resistance of an anisotropic thin magnetic film is a function of the angle between the current and the magnetic moment, with typical maximal resistance changes  $\frac{\Delta R}{R}$  of up to 2 %. Commercial sensors and disk drive read heads based on the *AMR* effect were developed in the past.

In 1988 the giant magnetoresistance (*GMR*) was discovered [2] [3] at 4.2 K and was found later at room-temperature [4]. In its simplest version, the *GMR* effect occurs in a stack consisting of two ferromagnetic layers separated by a nonmagnetic conducting material. The resistance depends on the relative orientation of the magnetizations of the two layers, with a resulting  $\frac{\Delta R}{R}$  up to 20 % at room-temperature. For multilayer systems,  $\frac{\Delta R}{R}$  values of up to 80 % at room-temperature are typical. These high values are the obvious reason, why *GMR* found its fast introduction in industrial products, like *GMR*-based disk drive read heads. Galvanic isolators, sensors [5] and magnetoresistive random access memory (*GMR*-MRAM) [6] have been introduced in the past. New applications are being developed in interdisciplinary fields, like *GMR* based biosensors, for instance [7].

A significant amount of spin dependent tunneling (SDT) between two ferromagnetic electrodes through an isolator at room-temperature was first reported in 1995 [8] [9] and tunneling magnetoresistance (*TMR*) values of up to 60 % at room-temperature have been achieved until now. Spin dependent tunneling is considered to replace the *GMR* in magnetoelectronic devices, the high resistance of the SDT elements makes them especially advantageous for MRAM [10] with first commercial products

proposed in the next years.

There are more areas of research with the goal to benefit from the spin of the electrons in electronic devices like the colossal magnetoresistance (*CMR*) [11], ferromagnetic semiconductors and spin transport in semiconductor–ferromagnet heterostructures, for instance [5]. The major challenge is to find materials which exhibits magnetoresistance or spin conserving transport, respectively, at room–temperature and at low magnetic fields.

In the past, a physical principle considered for a memory was mostly accompanied by a corresponding concept for a logic. Among the ideas based on magnetism, bubble memory [12] (but not logic) made it to a commercial product, for instance.

Less emphasized till now are logic circuits based on the magnetoresistive (*MR*) effects. There are a number of concepts for logic devices based on the *MR* effects [13] [14] [15] [16] [17] [18] [19] [20] [21], even the idea for one concept was published more than 40 years ago [22]. These concepts have in common that the logic inputs are magnetic fields at the locations of *MR* elements and that the logic output is sensed via the resistance states of *MR* elements. High and low resistance states of a *MR* element form the basis of the digital logic, the Boolean 0 and Boolean 1. The need of a semiconductor based circuitry to amplify an output to be available as a new input is the other common point. Even for the low resistive *GMR* based logic a magnetoresistance of at least 800 % would be needed to make the amplifier circuitry unnecessary [7]. Compared to usual semiconductor–based logic, there is no advantage. The main features which make a hybrid *MR*–semiconductor logic device worth to look on, are the freedom to program its logic function and the nonvolatility of the logic output and inputs (for some concepts). Programmable *MR*–logic can be categorized in two parts: (a) mask programmable logic [13] [15], in which the logic function is defined in one process step during the fabrication process, and (b) field programmable *MR*–logic [14] [16] [17] [18] [19] [21], which can be programmed on chip.

This work deals with the basic logic gates based on spin dependent tunneling elements, where the emphasize is put on field programmable spin–logic gates [14]. The vision is to build up a field programmable gate array (FPGA) based on spin–logic gates. Arranged within an array, the inputs and the outputs of the spin–logic gates are connected to each other and to the global input and output pins. These connections are part of the programming information. Within spin–logic gates, the logic operations are performed and the other part of the programming information is stored.

In state–of–the–art FPGA's, semiconductor–based central logic blocks (CLB's) correspond to spin–logic gates. CLB's exist in various designs and with a variable

number of logic inputs. The number of programmable logic functions is a reasonable property for a comparison of CLB's and spin-logic gates. Indeed, a three input one-output spin-logic gate does correspond to a CLB of a commercial FPGA [23] with respect to the number of programmable logic functions.

The judgement if spin-logic gates are capable to replace CLB's cannot be done by a direct comparison of the logic blocks, a reliable judgement must be based on the comparison of complex FPGA-like circuits. Since the basic architecture and functionality of semiconductor based logic and spin-logic are different, it is not possible to use the tools developed for semiconductor based FPGA's (e. g. programming- and routing-software) for magnetic FPGA's. Henceforth a reliable judgement on spin-logic is not possible, since it would require software tools which do not exist nowadays.

The advantage of a magnetic FPGA results from the inherent properties of spin-logic gates:

- a.) High operating frequency (the principal physical limit is 5 Ghz) [24]
- b.) No practical limitation of programming cycles
- c.) Programming within one clock cycle
- d.) Nonvolatility of the programing information
- e.) Nonvolatility of the logic outputs
- f.) Nonvolatility of the logic inputs
- g.) Radiation hardness
- h.) Compatibility to nonvolatile memory (MRAM)

State-of-the-art FPGA's are capable to fulfill these properties separately, exemplarily there is no semiconductor-based FPGA which fulfills properties a-c. The combination of properties a, b and c makes a magnetic FPGA useful for reconfigurable computing [25]. Within this application, the FPGA is used as a processor with its programming optimized for a given task to achieve improved computational results [25]. Rapid programming is essential for reconfigurable computing.

A magnetic FPGA with the main part of its programming information stored in the spin-logic gates holds much promise for reconfigurable computing [25].

This thesis is organized as follows. First, the physical principles of spin dependent tunneling which are important for logic gates are reviewed.

Then the principle of digital logic based on SDT elements is explained. Beside the discussion of concepts known from literature, own concepts are introduced.

The feasibility of mask programmable [15] and field programmable [14] [17] logic gates based on SDT elements with a minimal feature size of 600 nm is shown.

Characteristics of single SDT elements with impact on logic gates are investigated.

The in-plane switching behaviour of the SDT element's soft magnetic (storage) layer is investigated for different shapes and aspect ratios down to a width of 600 nm. A systematic study on so-called astroids of micron-sized SDT elements is presented. Magnetostatic interactions of the magnetic layers within SDT elements are identified from these measurements.

For the spin-logic gates, critical factors for working logic gates are identified. The measured statistical fluctuations of the resistance-area product (*RAP*) and *TMR* of the SDT elements forming a spin-logic gate are measured and the corresponding yield of working spin-logic gates is calculated.

Furthermore, the benefit of the introduction of a reference layer system which is switchable (programmable) by a current on-chip is discussed. Concretely, the reference layer system Ru/CoFe is investigated. The physical origin of the increase of the CoFe coercivity with increasing thicknesses of the Ru-buffer is investigated.

Finally, the magnetic stability, which is a prerequisite for a working spin-logic, is investigated for different designs of the tunneling stack.

The thesis ends with a summary of the work and an outlook.

# Chapter 2

## Theory

### 2.1 Theory of spin dependent tunneling

#### 2.1.1 Quantum mechanical tunneling

Within the picture of classical physics, tunneling does not exist. It is described by the concept of quantum mechanics. Tunneling is the phenomena of a not vanishing transmission probability of particles (e. g. electrons) through a potential barrier (e. g. isolator) with an energy level higher than the energy of the particle.

Nowadays, the tunneling effect is utilized in electronic components like the resonant tunneling diode, for instance, and in measurement equipment like the superconducting quantum interference device (SQUID) magnetometer or the scanning tunneling microscope (STM).

The tunneling effect can be calculated from the stationary Schrödinger equation:

$$H\Psi = E\Psi \quad (2.1)$$

Figure 2.1 shows an one dimensional potential well with emerging particles from the left, described by the wave function  $\Psi_0$ . In classical physics, the particle is reflected by the potential well since its energy  $E$  is smaller than the height of the potential  $V_0$ . But the solution of equation 2.1 is not zero within the potential barrier and right of it. The phenomena of the not vanishing transmission coefficient (or tunneling

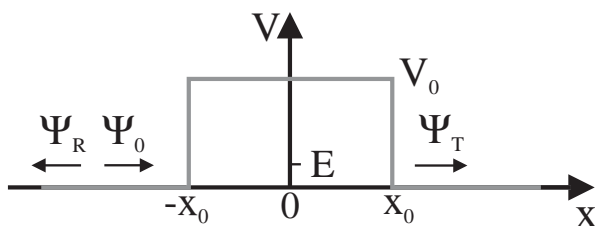


Figure 2.1: Potential well centered around  $x = 0$ . The wave function  $\Psi_0$  describes emerging particles with an energy  $E$  smaller than the height of the potential well ( $V_0$ ),  $\Psi_R$  describes the reflected particles with energy  $E$  (assuming elastic scattering), and  $\Psi_T$  describes the transmitted particles with energy  $E$ .

probability)  $T(E) = \frac{|\Psi_T|^2}{|\Psi_0|^2}$  is called quantum mechanical tunneling. For the cases relevant in spin dependent tunneling,  $T(E)$  is well approximated by [26]:

$$T(E) \approx \exp \left[ -\frac{8\pi}{h} \sqrt{2m \cdot (V_0 - E)} \cdot x_0 \right] \quad (2.2)$$

In most cases, potentials involved in tunneling are a continuous function of  $x$ .  $T(E)$  is approximated in these cases by the WKB method (Wenzel-Kramers-Brillouin) [27] [26]:

$$T(E) \approx \exp \left[ -\frac{4\pi}{h} \int_{-x_0}^{x_0} \sqrt{2m \cdot (V(x) - E)} dx \right] \quad (2.3)$$

Regarding itinerant electrons of two metals separated by an insulating material, the potential well in Fig. 2.1 corresponds to the isolator which does not exhibit electron states in the energy regime of the metal's occupied electron states. Figure 2.2 shows an idealized profile of the electron's potential of a metal–isolator–metal (M–I–M) contact at a voltage  $V$  applied across the isolator. For the tunneling process in the M–I–M contact, both electrons to tunnel and free electron states at corresponding energies in the other metal are requested. With no external voltage applied, the net tunneling current density is zero:

$J_T = J_{1 \rightarrow 2} - J_{2 \rightarrow 1} = 0$ . When applying a voltage, the Fermi levels of the metals are shifted with respect to each other which results in a net tunneling current, because the electrons in the regime of the Fermi level of metal 2 face free electron states in metal 1 at the same energy, but not vice versa. Hence for the technical current density  $J_i$ ,  $J_{1 \rightarrow 2} > J_{2 \rightarrow 1}$ .

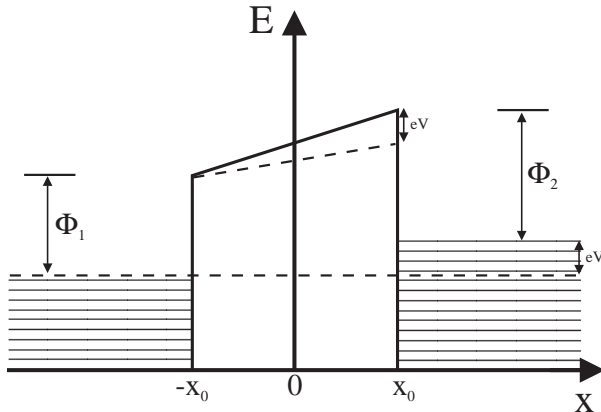


Figure 2.2: Idealized potential energy profile of electrons in a M–I–M contact. The occupied electron states in the metals are indicated by the dashed area. The distance of the Fermi level to not occupied electron states in the insulator is  $\Phi_1$  for metal 1 and  $\Phi_2$  for metal 2. A voltage  $V$  is applied across the isolator, hence the Fermi levels of the metals are shifted by  $eV$  with respect to each other.

With the simplification of the electronic band structure by that of a free electron gas, the net tunneling current is approximated for a generalized potential well at  $T = 0$  K by [28]:

$$J = \frac{e}{2\pi h \beta^2 (2x_0)^2} \left( \bar{\varphi} \exp \left[ -\frac{8\pi \beta x_0 \sqrt{2m_e}}{h} \sqrt{\bar{\varphi}} \right] - (\bar{\varphi} + eV) \exp \left[ -\frac{8\pi \beta x_0 \sqrt{2m_e}}{h} \sqrt{\bar{\varphi} + eV} \right] \right)$$

(2.4)

$m_e$  is the electron mass,  $\bar{\varphi}$  is the mean of the barrier height above the Fermi level of the negatively biased electrode and the correction term  $\beta$  is given by:

$$\beta = 1 - \frac{1}{16\bar{\varphi}^2 x_0} \int_{-x_0}^{x_0} [\varphi(x) - \bar{\varphi}]^2 dx \quad (2.5)$$

The arbitrary shape of the potential well is considered by  $\bar{\varphi}$  and the correction term  $\beta$  in equation 2.4. The theoretical consideration of image force and temperature on equation 2.4 do not change its qualitative characteristic [28] [29]. Asymmetric M-I-M contacts, e. g. with different metals, lead to an asymmetry of the  $J$ - $V$  characteristic [30]. Brinkman performed an approximation for a trapezoidal potential well as shown in Fig. 2.2 [31]. In contrast to equation 2.4, his result does not neglect the asymmetry of the potential well  $\Delta\varphi = \phi_2 - \phi_1$ . The conductance  $G(V)$  at T=0 K expanded in powers of the voltage is approximated by [31]:

$$\frac{G(V)}{G(0)} = 1 - \left( \frac{\pi\sqrt{2m_e}x_0\Delta\varphi}{3h\bar{\varphi}^{\frac{3}{2}}} \right) eV + \left( \frac{2(\pi\sqrt{2m_e}x_0)^2}{h^2\bar{\varphi}} \right) (eV)^2 \quad (2.6)$$

For a typical potential well height in the order of 1 eV and an isolator thickness in the order of 1 nm, the  $RAP$ -value of M-I-M contacts lies in a regime ( $k\Omega \cdot \mu\text{m}^2$ ), which is reliable for magnetoelectronic devices.

The approximations presented here describe qualitatively the experimentally observed  $J$ - $V$  characteristics in SDT elements (Ferromagnet-Isolator-Ferromagnet, FM-I-FM).

The commonly accepted criterion to check for tunneling is the measurement of the temperature dependence of the tunneling resistance [32].

### 2.1.2 Spin dependent tunneling and magnetoresistance

Spin dependent tunneling was first observed by Tedrow and Meservey [33] [34] in a superconductor (Al) – isolator ( $\text{Al}_2\text{O}_3$ ) – ferromagnet (Ni) structure.

The first magnetoresistance measurement on a FM-I-FM structure was reported by Jullière (at 4.2 K) and was interpreted by spin dependent tunneling [35]. The tunneling resistance was observed to depend on the relative orientation of the magnetic layer's magnetizations. This phenomena is discussed so far in conjunction with the consideration of the magnetic exchange interaction of the conduction electrons [35]. Figure 2.3 (a) shows a model of the energy versus density of states (DOS) profile of the conduction bands of two ferromagnetic electrodes with parallel alignment of the magnetizations. The exchange interaction leads to an exchange splitting  $\Delta$  of the parabolic energy profiles between electrons with their magnetic moment parallel

(down to lower energies) and antiparallel (up to higher energies) to the magnetization. The parabolic profile is a consequence of the free electron gas approximation. Fig. 2.3 (b) shows the band structure for antiparallel alignment of the two magnetizations.

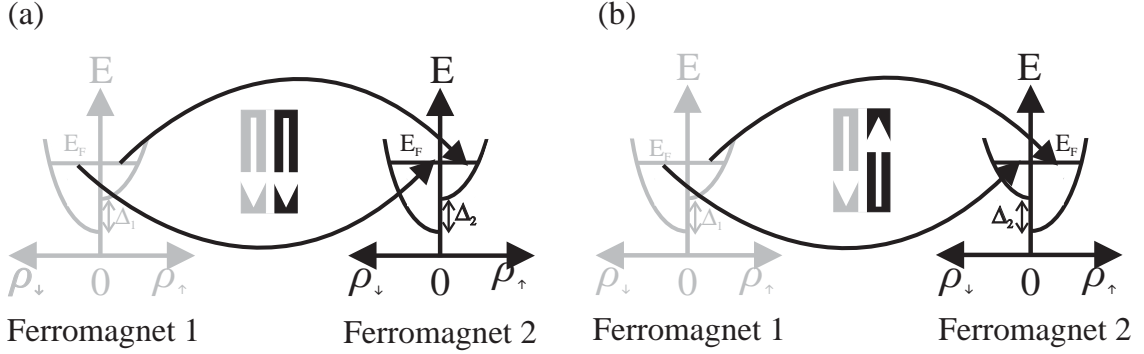


Figure 2.3: Model proposed by Jullière to explain magnetoresistance in Ferromagnet–Insulator–Ferromagnet structures by spin-dependent tunneling. The diagrams show the electron energy in the conduction band versus the density of states  $\rho_{\uparrow\downarrow}$  for the free electron gas. ( $\uparrow\downarrow$ ) indicates the direction of the electrons magnetic moment. In order to take account for the exchange interaction of the electrons, the bands are shifted with respect to each other with a resulting, material dependent shift  $\Delta$ . Due to the preservation of the spin in the tunneling process, there are two independent spin channels, indicated by the arrows, through which tunneling takes place. (a) Parallel alignment of the magnetizations. Since only the electrons in the regime of the Fermi level tunnel to unoccupied states at the same energy in the other electrode, the current density of each spin channel is assumed to be proportional to the corresponding DOS at the Fermi level. Due to the shift  $\Delta$ , there are, defined by the spin, majority and minority electrons at the Fermi level. For parallel alignment, the two spin channels are majority–majority and minority–minority. (b) For antiparallel alignment of the magnetizations, the two spin channels are majority–minority and minority–majority. The different configurations of the spin channels lead to different tunneling resistances in (a) and (b).

As a consequence of the exchange splitting, the DOS at the Fermi energy ( $E_F$ ) are different for both spin (respectively magnetic moment) directions. Since only the electrons with energy in the regime of the Fermi level contribute to tunneling, more electrons with magnetic moment parallel to the magnetization (majority) than electrons with magnetic moment antiparallel to the magnetization (minority) are available for tunneling. Furthermore it is assumed that the spin direction is preserved in tunneling. Thus there are, as shown in Fig. 2.3, two different paths for the tunneling current, so-called spin channels, namely electrons with spin up (down) tunneling from one electrode to unoccupied spin up (down) states in the other electrode. Furthermore it is assumed that the transmission probability  $T(E_F)$  is the same for the two spin channels. Jullière assumed the tunneling current density



of each spin channel to be proportional to the corresponding DOS (majority and minority) near the Fermi level.

The current densities for parallel (P) and antiparallel (AP) alignment of magnetizations in a SDT element are given in terms as used in Fig. 2.3 by:

$$\begin{aligned} j_P &\propto T(E_F) \cdot (\rho_{1\uparrow}^{Min}(E_F) \cdot \rho_{2\uparrow}^{Min}(E_F) + \rho_{1\downarrow}^{Maj}(E_F) \cdot \rho_{2\downarrow}^{Maj}(E_F)) \\ j_{AP} &\propto T(E_F) \cdot (\rho_{1\uparrow}^{Min}(E_F) \cdot \rho_{2\uparrow}^{Maj}(E_F) + \rho_{1\downarrow}^{Maj}(E_F) \cdot \rho_{2\downarrow}^{Min}(E_F)) \end{aligned} \quad (2.7)$$

With no voltage applied across the isolator or tunneling barrier, respectively, there is a dynamical equilibrium with tunneling currents flowing from FM 1 to FM 2 and vice versa. By applying a voltage across the tunneling barrier, a net tunneling current proportional to equation 2.7 flows. Thus, the magnetoresistance measured first by Jullière and its dependence on the alignment of the magnetic layers is explained by spin dependent tunneling within this simple model. Generally, the  $TMR$  is defined by ( $R_{AP}$ : tunneling resistance when the SDT elements reference layer magnetic moment is antiparallel to that of the soft magnetic layer.  $R_P$ : tunneling resistance for parallel alignment of the magnetic moments.):

$$TMR = \frac{R_{AP} - R_P}{R_P} \quad (2.8)$$

Within Jullière's model, the  $TMR$  is given by:

$$TMR = \frac{\rho_{1\uparrow}^{Min}(E_F) \cdot \rho_{2\uparrow}^{Min}(E_F) + \rho_{1\downarrow}^{Maj}(E_F) \cdot \rho_{2\downarrow}^{Maj}(E_F)}{\rho_{1\uparrow}^{Min}(E_F) \cdot \rho_{2\uparrow}^{Maj}(E_F) + \rho_{1\downarrow}^{Maj}(E_F) \cdot \rho_{2\downarrow}^{Min}(E_F)} - 1 = \frac{2P_1P_2}{1 - P_1P_2} \quad (2.9)$$

$P$  is the spin polarization of the corresponding electrode at the Fermi level and is defined as ( $\rho \propto wavenumber k$  in the free electron gas model):

$$P(E_F) = \frac{\rho^{Maj}(E_F) - \rho^{Min}(E_F)}{\rho^{Maj}(E_F) + \rho^{Min}(E_F)} = \frac{k^{Maj}(E_F) - k^{Min}(E_F)}{k^{Maj}(E_F) + k^{Min}(E_F)} \quad (2.10)$$

The spin polarization of magnetic materials was measured by tunneling in FM-I-S structures [36] and in S-FM structures by Andreev Reflection [37].

Even though the one-dimensional model of Jullière explains the basic mechanism of  $TMR$ , namely spin dependent tunneling, it is too simple. A simplifying assumption is, in particular, the simple parabolic band structure of the ferromagnets. The free electron gas model does not take into account the interactions of conduction electrons in a metal, e. g. with the lattice. A calculation on the conduction band structure of Nickel [38], for instance, exhibits a complex shape of the band structure and, in contrast to the Jullière model, more minority than majority electrons are at the Fermi level.

Recent experiments on Co-Isolator-La<sub>0.7</sub>Sr<sub>0.3</sub>MnO<sub>3</sub> structures showed the impact

of the metal–oxide interface on *TMR*: For  $\text{Al}_2\text{O}_3$  as the tunneling barrier, the *TMR* was positive, for  $\text{SrTiO}_3$  or  $\text{Ce}_{0.69}\text{La}_{0.31}\text{O}_{1.845}$ , the *TMR* turned out to be negative [39]. The change in sign of the *TMR* was explained by a variation of the transmission probabilities  $T(E_F)$  of the two spin directions through the Co–Isolator interface for different isolators. Alternatively, the spin polarization can change at the interfaces.

Beside the spin-dependence,  $T(E)$  is in general not momentum and energy independent as assumed by Jullière. Furthermore the model cannot explain the dependencies of *TMR* on barrier height and barrier thickness or more complex situations [40]. Also temperature effects are not included. More lacks of the model are discussed in Ref. [40].

Slonczewski considered the fact, that the two ferromagnets separated by an isolator which allows tunneling are not independent systems [41]. He treated FM–I–FM contacts as one system and described the two ferromagnets by two simple parabolic bands separated by the exchange splitting. He assumed also the momentum parallel to the interface plane to be conserved in the tunneling process and approximated the isolator by a potential well of height  $\Phi$ . The principal result is that  $P$  and hence the *TMR* depends on the height  $\Phi$  of the barrier ( $h\kappa = \sqrt{4\pi m(\Phi - E_F)}$ ):

$$P(E_F) = \frac{k^{Maj}(E_F) - k^{Min}(E_F)}{k^{Maj}(E_F) + k^{Min}(E_F)} \cdot \frac{\kappa^2(E_F) - k^{Maj}(E_F)k^{Min}(E_F)}{\kappa^2(E_F) + k^{Maj}(E_F)k^{Min}(E_F)} \quad (2.11)$$

Up to now, there is no model that explains the whole experimentally determined phenomena of *TMR*.

The important breakthrough of *TMR* with respect to its application in magnetoelectronics was in 1995. Both, Miyazaki [8] and Moodera [9], reported on *TMR* at room–temperature in  $\text{Fe}/\text{Al}_2\text{O}_3/\text{Fe}$  elements and  $\text{CoFe}/\text{Al}_2\text{O}_3/\text{Co}$  (NiFe), respectively.

### 2.1.3 Major loop and minor loop

Major and minor loop refer to transport measurements on SDT elements during a scan of the external magnetic field. The simplest SDT element consists of two ferromagnetic layers separated by a tunneling barrier. The magnetization of the so-called reference layer reverses at higher magnetic fields than the magnetization of the so-called soft magnetic layer. In the ideal case the magnetization of the reference layer is not affected by the switching of the soft magnetic layer which leads to maximal *TMR*. Figure 2.4 explains the difference of the minor and major loop measurement. While during a minor loop measurement the magnetic field is scanned in a regime such that only the soft magnetic layer switches, within a major loop measurement the reference layer is reversed, too.

Figure 2.4 shows an idealized switching behaviour of the magnetic layers that assumes the magnetizations to be in single domain states. However this is not the scenario one encounters right away during the investigation of SDT elements. Some measures one can perform on the SDT elements to achieve the desired switching behaviour are discussed in the next section.

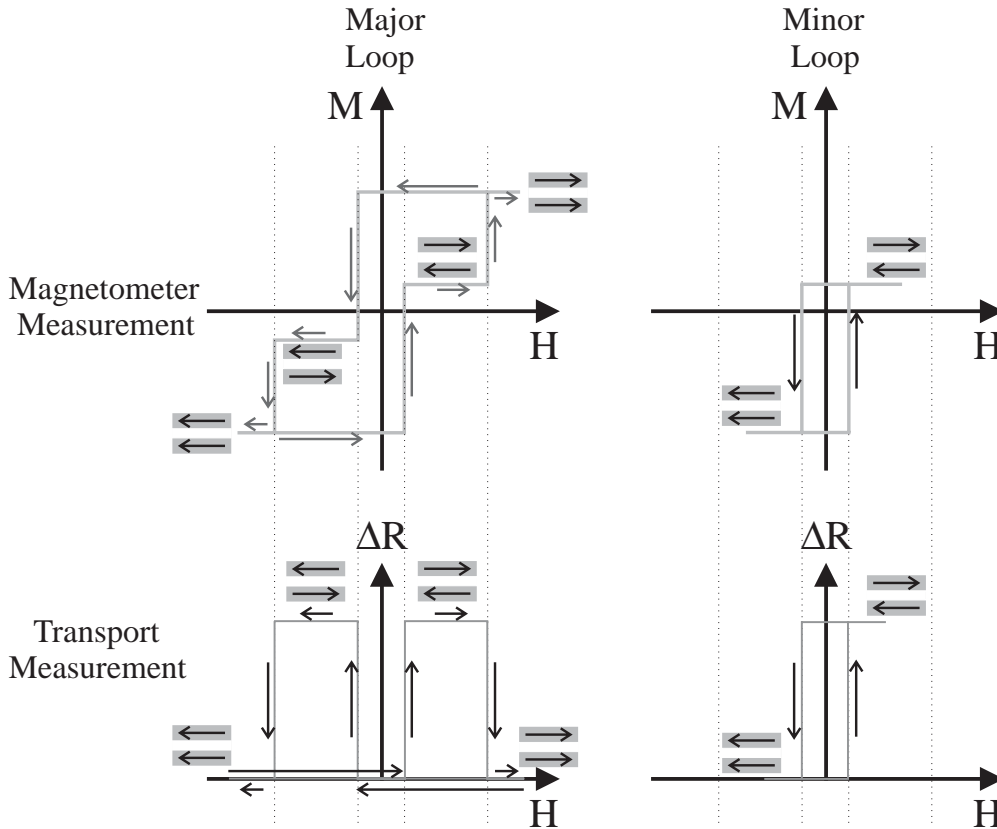


Figure 2.4: Major loop and minor loop measurement. The top row shows the hysteresis of the magnetization of a SDT element versus the external magnetic field  $H$ , the bottom row the change of the tunneling resistance with respect to the minimal tunneling resistance with both magnetizations orientated parallel to each other. The arrows indicate the course of the measurement.

## 2.2 Switching behaviour of thin magnetic films

### 2.2.1 The total free energy of a ferromagnetic body

The principle of the theory on the magnetization configuration of a magnetic body is the minimization of the free energy that describes the system [42]. When changing the external magnetic field, the magnetic body system responds with a change of the magnetization towards a configuration in which the free energy exhibits a relative or absolute minimum. At  $T = 0$  K, the magnetization remains in this energetic minimum. Thermal fluctuations (thermal activation) opens the path for the magnetization configuration to leave a relative minimum by climbing the energy barrier and relaxing towards an energetically lower lying configuration. The experimental observation of such thermal fluctuations in sub-micrometer sized SDT elements are reported in references [43] and [44].

The magnetic system "SDT element" consists of at least two magnetic layers, storage (soft) and reference (hard) magnetic layer. The reference layer interacts with the soft magnetic layer magnetically and hence influences its magnetic switching behaviour. For simplicity, a single magnetic layer is first discussed and then the interactions of the magnetic reference layer system and its impact on the switching behaviour of the soft magnetic layer.

The total free energy ( $E_{Total}$ ) of a single magnetic layer is given by an integral over the volume of the sample [12]:

$$E_{Total} = \int [E_{Exchange} + E_{Anisotropy} + E_{ExternalField} + E_{StrayField} + E_{Stress}] dV \quad (2.12)$$

$E_{Exchange}$  is the volume exchange stiffness energy due to the exchange coupling between the spins.

$E_{Anisotropy}$  is the anisotropy energy due to the spin-orbit interaction of the electrons.

$E_{ExternalField}$  is the Zeeman energy which describes the interaction energy of the magnetization with an external magnetic field.

$E_{StrayField}$  is the energy stored in the magnetic field which is generated by the magnetic body itself.

$E_{Stress}$  describes the energy due to stress acting on the magnetic body.

The energy stored in the magnetic stray field ( $E_{StrayField}$ ) is decreased when the magnetization of a magnetic layer is changed from a single domain state to a multiple domain state. In a multiple domain state, the magnetization of the magnetic body splits up in regions (domains) with not aligned magnetizations separated by domain walls. A multiple domain configuration of the magnetization of a magnetic

layer is favorable, if the increase of the other energies (e. g. energy stored in domain walls) in equation 2.12 is less than the decrease of the stray field energy.

The micromagnetic differential equations are a mathematical tool to model the magnetic switching behaviour of a magnetic body. The magnetic body is discretized into small volumes whereby each volume is associated by a magnetic moment. Micromagnetic equations describe the torque acting on the magnetic moments localized in the magnetic body. They are derived from the total free energy (equation 2.12) by the variational principle [45]. The so-called Landau–Lifshitz equation is given by [12]:

$$\frac{d}{dt}\vec{M} = -\gamma\vec{M} \times \vec{H}_{eff} - \frac{\gamma\alpha}{M_s}\vec{M} \times (\vec{M} \times \vec{H}_{eff}) \quad (2.13)$$

$$with \quad \vec{H}_{eff} = -\mu_0^{-1} \frac{\partial E}{\partial \vec{M}}.$$

$\vec{M}$  is the pointwise magnetization,  $\vec{H}_{eff}$  is the pointwise effective magnetic field,  $\gamma$  is the gyromagnetic ratio of the magnetic material and  $\alpha$  is the damping coefficient. The first term in equation 2.13 describes the precession of the magnetization around the effective magnetic field, the second term takes the experimentally observed damping (e. g. due to eddy currents) into account.

There is a number of numerical codes available which calculate the magnetization configuration of a magnetic body on the basis of the micromagnetic equations [46] [47].

Magnetic layers of SDT elements exhibit a typical thickness below 10 nm which is small compared to their lateral dimensions. The stray field energy  $E_{StrayField}$  associated with a magnetization perpendicular to the magnetic layer plane is big compared to an in-plane magnetization, hence SDT elements exhibit in-plane magnetizations. For the same reason, domains are separated by so-called Néel walls where the transition between domains is accomplished by an in-plane tilt of the spins, respectively magnetic moments. For micromagnetic simulations, the magnetic layer has to be discretized in finite elements. The spatial extend of the finite elements has to be smaller than the smallest feature in the configuration of the magnetization which is for thin magnetic layers the core of the Néel wall. A finite element size smaller than 7 nm turned out to consequence in reliable simulations for NiFe. Nevertheless, the goal of making exact predictions of a real system like a SDT element by micromagnetic simulation is hard to reach, since the magnetic system of a magnetic layer is complex and exhibits many parameters to be considered in a simulation (e. g. granularity of magnetic layers, exchange coupling of grains, impact of defects, magnetic coupling of reference and storage electrode, reference layer systems,...).

A magnetization configuration and its response to an external magnetic field which

can be treated analytically is the single domain state. Such a magnetic switching behaviour is sometimes called small-particle switching since one expects a single domain state if the magnetic body is smaller than the typical size of a domain wall. The switching behaviour of a single domain particle is favorable for SDT elements used in magnetoelectronic devices, since a coherent reversal of a magnetization is fast (up to 5 GHz [24]), reproducible and, according to the Stoner and Wohlfarth theory [48], offers a mechanism for addressing a SDT element. The discussion of experimentally found single domain like switching behaviour starts at page 72, the Stoner and Wohlfarth theory is recapitulated in the next section.

### 2.2.2 Single domain switching behaviour

The magnetization of an uniform in-plane magnetized particle can be described by an angle  $\varphi$ . According to Stoner and Wohlfarth, the total free energy of a single domain particle is given by [12]:

$$E_{Total} = \int [g(\varphi) - \mu_0 H_{\parallel} M_S \cos \varphi - \mu_0 H_{\perp} M_S \sin \varphi] dV \quad (2.14)$$

$g(\varphi)$  is a generalized anisotropy functional and the remaining two parts form the external field energy.  $\varphi$  is defined as the angle between the magnetization and the positive  $H_{\parallel}$ -axis.  $H_{\parallel}$  is the external magnetic field parallel to the easy anisotropy axis (axis of anisotropy energy minimum) as defined by  $g(\varphi)$ ,  $H_{\perp}$  is the corresponding in-plane component perpendicular to the easy axis and is called bias magnetic field. Here a simple second-order uniaxial anisotropy defined by  $g(\varphi) = K \cdot \sin^2 \varphi$  is considered. The magnetization reversal along the easy axis of such a magnetic particle is accomplished by coherent rotation since the magnetization is assumed to be uniform. The magnetic field parameters ( $H_{\parallel}, H_{\perp}$ ) at which the reversal of the magnetization happens are given by the stability limit  $\frac{\partial^2 E_{Total}}{\partial \varphi^2} = 0$  [12]. The graphical representation of the stability limit, the so-called astroid curve, is shown in Fig. 2.5 for a uniformly magnetized NiFe ellipsoid exhibiting an uniaxial shape anisotropy. For comparison, a measured astroid of the soft magnetic layer of a SDT element is also shown (A more detailed discussion on the measured astroids starts at page 72).

Within the Stoner and Wohlfarth theory, the anisotropy field  $H_k = \frac{2K}{\mu_0 M_s}$  is equal to the coercivity  $H_c$  when no bias magnetic field is applied.

The drastic differences between theory and experiment are explained by the deviations from the single domain state in real particles.

Not considered until now within the discussion of the switching behaviour of the soft magnetic layer and hence the magnetoresistance curve are the magnetic interactions

between the soft magnetic layer and the reference layer system which are discussed next.

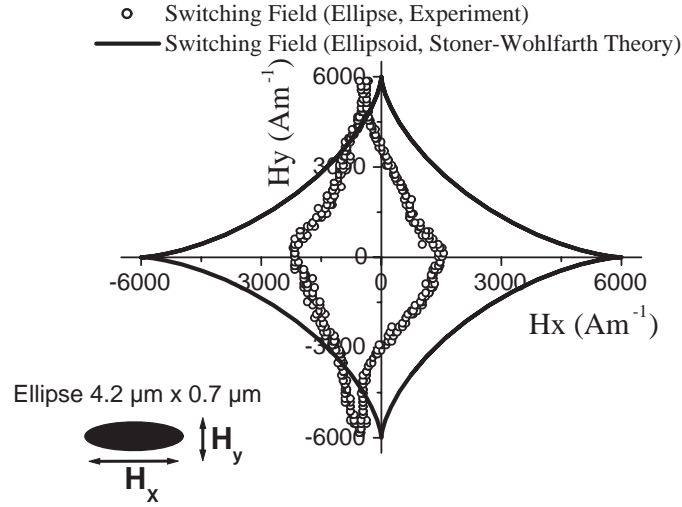


Figure 2.5: – Switching behaviour of a magnetic particle with a uniaxial shape anisotropy according to the Stoner and Wohlfarth theory. The theoretical astroid curve is calculated for an ellipsoid (4200 nm × 700 nm × 6 nm) of NiFe ( $M_S = 800 \text{ kAm}^{-1}$ ).

○ Measured astroid of a 6 nm thick, 4200 nm × 700 nm elliptical shaped NiFe layer forming the detection layer of a SDT element. The difference to theory is explained by a multiple domain behaviour of the NiFe layer.

### 2.2.3 Magnetic coupling in SDT elements

The magnetic layer systems in a SDT element are separated by  $\text{Al}_2\text{O}_3$  with typical thickness of 1–2 nm. The two most important magnetostatic coupling mechanism, Orange Peel (Néel) and edge stray field coupling, are explained in this section.

Effects of domain walls in the reference layer system causing magnetic stray fields which act on the soft magnetic layer are not discussed here, these effects have to be prevented in applications. Nevertheless such effects were encountered in the measurements (Fig. 6.4) and can be prevented by a special design of the tunneling stack (page 18). Exchange interactions through the tunneling barrier are minimized because of its band structure. If pinholes are present in the tunneling barrier, exchange interactions are mediated through these conduction centers associated with a tiny or not measurable  $TMR$  in such SDT elements.

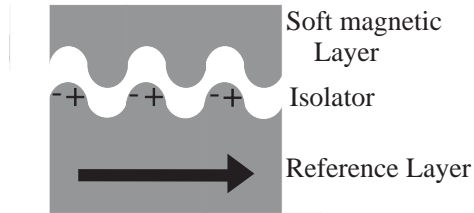
The theory on the ferromagnetic so-called Orange Peel coupling between magnetic layers that exhibit interface roughness and are separated by a nonmagnetic spacer material was introduced by Néel. The theory is based on assumptions which are reliable for SDT elements. Firstly a correlation between the roughnesses of soft and reference electrode as shown in Fig. 2.6 is assumed. Secondly the roughness

is assumed to be sinusoidal and is modeled with a peak to peak amplitude  $h$  and wavelength  $\lambda$ . Furthermore the ferromagnetic reference electrode is assumed to be of infinite thickness and the roughness on top of the soft magnetic electrode is neglected. Both magnetic electrodes are assumed to be rigidly and homogeneously magnetized. In magnetostatics, discontinuities of the magnetization at the boundaries of the magnetic material act as plus or minus poles of the magnetic field. The magnetic stray field points from plus to minus. With the correlated roughness of the magnetic layers as shown in Fig. 2.6 (columnar growth of subsequently sputtered magnetic layers), the mean stray magnetic field originating from the reference electrode at the location of the soft magnetic electrode (mainly its valleys) points in the direction of the reference electrodes magnetization. Hence the mean coupling is ferromagnetic, expressed as a magnetic field, the Néel coupling is given by [49]:

$$H_{0N\acute{e}el} = \frac{\pi^2}{\sqrt{2}} \left( \frac{h^2}{\lambda d_S} \right) M_R \exp \left[ \frac{-2\pi\sqrt{2}d_I}{\lambda} \right] \quad (2.15)$$

$d_S$  is the thickness of the soft magnetic electrode,  $d_I$  the thickness of the isolator (separating material in general).

### Ferromagnetic Coupling



### Antiferromagnetic Coupling

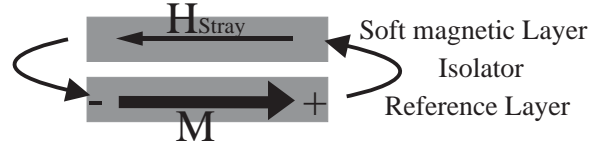


Figure 2.6: Left: Mechanism of the Néel coupling. Due to the correlated roughness at the isolator interface, magnetic dipoles are present at the magnetic parts of the interfaces isolator–magnetic layers. Considering the reference layer, the mean of the magnetic stray field due to the dipoles at the interface over the volume of the soft magnetic layer couples the magnetic moment of the soft magnetic layer ferromagnetically to the magnetic moment of the reference layer system.

Right: Magnetic poles at the edges of the SDT element respectively reference layer system cause a magnetic stray field at the location of the soft magnetic layer which tends to align the magnetic moment of the soft magnetic layer antiparallel to that of the reference layer. The net coupling is the sum of both contributions.

The other important magnetostatic interaction between the magnetic electrodes in SDT elements is the edge magnetic stray field coupling as shown in the right part of Fig. 2.6. A homogeneously magnetized reference layer is associated with an in–plane



magnetic stray field at the location of the soft magnetic electrode which is orientated antiparallel to the magnetic moment of the reference electrode. Its magnitude and in-plane direction does vary within the location of the soft magnetic layer. The strength of the edge magnetic stray field depends on the geometry of the reference layer system.

The net magnetic coupling of the soft electrode is given by the sum of both, the Néel coupling field and the edge magnetic stray field.

## 2.3 Design of SDT stacks

SDT elements have to fulfill a number of requirements to be usable for logic gates. Many of these requirements match with these for memory applications which are temperature stability, magnetic stability, centered minor loops, a single domain like switching behaviour which is reproducible, reproducibility of  $R$ ,  $TMR$  and astroids of nominal identical SDT elements and high yield in production.

Since state-of-the-art concepts for memory and logic rely on CMOS (complementary-metal-oxide-semiconductor) circuitry, the SDT element circuitry has to be connected to the underlying CMOS circuitry. The fabrication process ends with a backend process in order to heal out damages and impurities of the silicon. Standard backend technology requires annealing at 400 °C – 450 °C [50]. Thus the SDT elements must exhibit stability to these temperatures for the time of backend process. The temperature stability has been investigated for different material systems and has been improved [51] [52] [53].

Magnetic stability of a SDT element means the preservation of the reference layers magnetization with switching cycles of the soft magnetic layer. From magnetic stability, the preservation of the SDT element's  $TMR$  in a magnetoelectronic device with operation time is concluded. The magnetic reference layers system must be stable up to  $10^{15}$  switching cycles of the soft magnetic layer for MRAM [54], which corresponds to about 3 years of operation. For spin-logic a higher cycling number is requested, since the operation frequency is higher.

A magnetic domain structure in the magnetic electrodes has to be prevented. The switching behaviour of the soft magnetic layers of the SDT elements must be such that it gives a minor loop as shown Fig. 2.4.

There must be two remanent ( $H = 0 \text{ Am}^{-1}$ ) resistance states (e. g. for storing the programming information in a nonvolatile way) and the separation of the states (respectively voltage signals) has to be maximized. In fact, magnetic stability and the characteristic of the minor loop result from the geometry of the SDT element and the design of the tunneling stack.

The resistance of a SDT element must be in the order of tens of  $\text{k}\Omega$  to allow MRAM with improved performance compared to DRAM [50]. The lower the tunneling resistance, the higher are the signal to noise ratio and the power consumption of a MRAM bit. The cut-off frequency (and hence the operation frequency) of a MRAM bit, however, decreases with increasing tunneling resistance.

The requirements on  $R$  and  $TMR$  for logic devices are qualitatively the same as for MRAM. Especially the concept of spin-logic benefits more from a high  $TMR$  than MRAM. The higher the  $TMR$ , the more logic inputs a basic spin-logic gate can have, as explained later (page 32). One difference between spin-logic and MRAM

with a consequence on the tunneling stack design is the choice of the reference layer system, as explained in the section on spin–logic (page 32), too.

The functional groups of the principal tunneling stack design are shown in Fig. 2.7



Figure 2.7: Sketch of a standard spin dependent tunneling stack. The different functional groups drawn may consist of sub–groups. The thicknesses correspond not to a real system.

The tunneling stack is deposited on a thermally oxidized Si substrate. The  $\text{SiO}_2$  on top of the Si prevents parasitic current flows through the substrate.

The first buffer system does have several functionalities. One is to provide a strong adhesion of the tunneling stack on the  $\text{SiO}_2$  which is necessary for the fabrication process (several ultrasonic treatments). Secondly, the first buffer influences the growth of the subsequent deposited layers and may have impact on the magnetic properties of the reference layer system. Fe in  $\text{Si}/\text{SiO}_2/\text{Fe6}/\text{Cu30}/\text{Co1.0}/\text{Cu1.0}/\text{Co1.5}$  (numbers correspond to thickness in nm) leads to an enhanced texture of the subsequent Cu/Co which consequences in better magnetic properties of the Co/Cu/Co system, for instance. Ta is used for its good adhesive properties and offers with its amorphous like surface a starting point for the growth of the subsequent layer with its preferred texture.

The bottom electrode is deposited next. The thickness and the material have to be chosen such that the resistance of the bottom electrode below the SDT element is small compared to the tunneling resistance of the corresponding SDT element. For spin–logic, the resistance of the patterned electrode must be small compared to the tunneling resistance of the SDT element. Cu30 ( $\rho_{\text{Cu},30\text{nm}} = 10\mu\Omega \cdot \text{cm}$ ) and Ru30 ( $\rho_{\text{Ru},30\text{nm}} = 20\mu\Omega \cdot \text{cm}$ ) were used.

Buffer system 2 is optional and is used to improve (e. g. by introducing a special texture) the magnetic reference layer system.

The simplest reference layer system is a magnetic layer grown on the bottom electrode. The drawback of such a system is the lack of magnetic stability [55] [56] [57]. Not reported so far and of interest to be investigated is the magnetic stability of a single magnetic reference layer with high uniaxial anisotropy (shape or intrinsic anisotropy).

An alternative for the hard magnetic system is the artificial antiferromagnet (AFi) [58].

It consists of two magnetic layers, separated by, and antiferromagnetically coupled through, a thin, nonmagnetic spacer layer. The strength and the sign (ferromagnetically or antiferromagnetically) of the coupling depends on the material composition of the AFi and on the thickness of the metallic spacer layer [59] [60]. The anticipated antiferromagnetic coupling strength between the magnetic layers of an AFi can thus be optimized via the thickness of the metallic spacer layer. At external field  $H_S$  (saturation field of an AFi), all the magnetizations are aligned parallel.

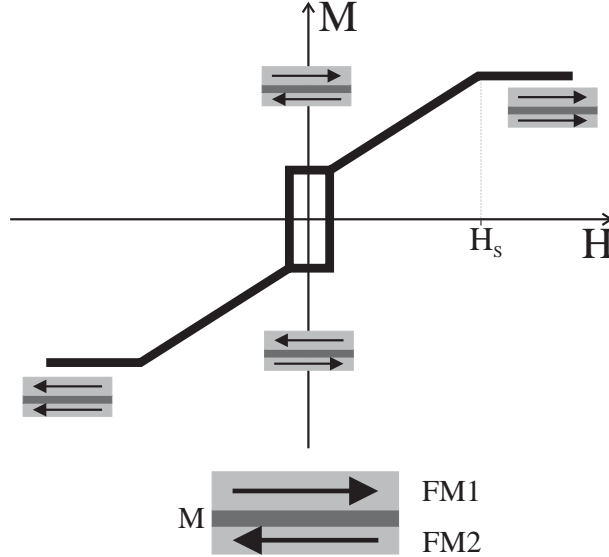


Figure 2.8: An AFi consists of two ferromagnetic layers (FM) separated by a metallic spacer (M). At zero external magnetic field, the two layers are coupled antiferromagnetically. The hysteresis curve is shown for the AFi in the single domain model. At saturation field  $H_S$  applied to the AFi, the antiferromagnetic coupling is overcome and the magnetic layers are aligned parallel to each other.

Within a simple model of single domain state and coherent rotation of the AFi's magnetic layers, the AFi system acts in an external magnetic field (for external magnetic field  $H$  small compared to the coupling field  $H_S$  of the two magnetic layers) as a rigid magnetic body with reduced magnetic  $m_R$  moment (difference of the two antiferromagnetically coupled magnetic moments) [58]. Furthermore the total friction per unit area  $T^{AFi}$  [58] against rotation of the magnetizations is proportional to the total thickness of the two magnetic layers. Thus the coercivity of an AFi is proportional to  $T^{AFi}$  and antiproportional to  $m_R$  and is hence in principle adjustable by the design of the AFi.

Furthermore, the net edge stray field coupling of the soft magnetic layer can be adjusted by the net magnetic moment of the AFi with respect of centering the minor loop. Due to the granularity of real magnetic films accompanied by local anisotropy axes within the AFi, the magnetizations exhibit a so-called ripple structure throughout the film [12] [61]. The consequence of the ripple structure in the

AFi is an additional mean magnetic stray field parallel to the corresponding net magnetization of the magnetic layers which act on the soft magnetic layer [62], too. Measurements on the magnetic stability of a micron sized SDT element with a CoFe/Ru/CoFe AFi showed improved magnetic stability compared to SDT elements with a Ru/CoFe reference layer system (page 97).

Another possibility to stabilize the magnetic reference layer system is exchange biasing. The magnetic moment of a magnetic layer is pinned by an adjacent antiferromagnetic layer through an exchange interaction. The directed pinning of the magnetic layer to the antiferromagnet is achieved by heating up and a subsequent cooling of the magnetic multilayer (MML) in a high magnetic field which aligns the magnetization. The pinning of the magnetic layer to the antiferromagnet starts when crossing the so-called blocking temperature of the antiferromagnet and is preserved at room-temperature. The pinning acts as an internal magnetic field on the magnetic layer, i. e. the hysteresis loop is shifted on the field axis. A significant improvement of magnetic stability of a single magnetic layer by exchange biasing was reported [55]. An investigation of exchange biased AFi's is given in Ref. [63].

The tunneling barrier follows the magnetic reference layer system. We deposited Al metal followed by a plasma oxidization process [9] [64]. Other techniques for forming the tunneling barrier are reported in literature [65] [66]. The growth of a tunneling barrier on top of a rough interface may lead to thickness variations which lead to a degeneration of the spin dependent tunneling and to a strong Néel coupling. The interface should be nearly atomically smooth. This has to be considered for the growth of the buffers and bottom electrodes, the roughness of these underlying system contributes to the roughness of the magnetic reference layer system.

The material and the thickness of the subsequent soft magnetic layer is chosen with the consideration of low coercivities within SDT elements.  $\text{Ni}_{81}\text{Fe}_{19}$  was used in this work. The thinner the magnetic layer, the smaller the shape anisotropy of a SDT element and the higher the Néel coupling. In order to increase the  $TMR$ , a CoFe (higher spin polarization than NiFe) layer was sometimes inserted between the tunneling barrier and the NiFe. The two magnetic layers couple ferromagnetically and switch as one magnetic layer.

The nonmagnetic layer on top (e. g. Ta, Ru) of the soft magnetic layer protects the tunneling stack from the atmosphere and from reactants during the fabrication process.

The requested temperature stability of the tunneling stack determines important aspects of its design like additional layers acting as diffusion barriers which prevents the mixture of magnetic and nonmagnetic materials at high temperatures. Furthermore the choice of materials is restricted by the demands of the temperature stability.



# Chapter 3

## Magnetic logic

In the past a physical principle considered for a memory was mostly accompanied by a corresponding concept for a logic. Concepts for a digital logic which utilizes the spin of the electrons are called here magnetic logic. Without claiming completeness, some concepts are mentioned.

Magnetic bubble logic [12] makes use of the stability of cylindrical domains (bubbles) in soft magnetic films with perpendicular (out-of-plane) anisotropy and the magnetostatic interaction between bubbles. Digital 1 and 0 correspond to the presence or absence of a bubble, respectively. A summary of basic bubble logic circuits is given in Reference [67].

Domain tip propagation logic [68] [12] makes use of the controlled growth and interaction of domain tips confined to narrow channels defined by a high-coercivity environment. Examples of the basic logic gates are given in Reference [69].

A concept proposed by Cowburn [70] makes use of the magnetostatic interaction of giant single spins each formed by circular shaped magnetic thin film elements. The circular magnetic dots are arranged in chains with an elongated, elliptic dot at one end serving as a logic input and a circular dot at the other end serving as the logic output. The contrast between the nucleation field and the propagation field of the circular dots magnetic moment direction is the basis of the logic gate.

Such a contrast has also been shown for the nucleation and propagation of domain walls in 5 nm thick and 100 nm wide  $\text{Ni}_{80}\text{Fe}_{20}$ -wires accompanied by reproducible switching (nucleation) fields [71]. This physical effect is suggested as a basis for magnetic logic devices (similar to the domain tip propagation logic). Recently the feasibility of a NOT gate has been demonstrated [72].

The concepts mentioned so far are complete magnetic logic devices, meaning the output of a logic gate can be directly used as the input for following logic gates. In principle, complete calculations can be performed just by changing magnetizations. The readout of the final result, e. g. via an inductive signal, the hall effect or via magnetoresistance requires finally some semiconductor based electronics.

The use of patterned thin magnetic films for logic circuits was proposed in 1959 [22]. The currents which produce the magnetic fields needed to switch a magnetic layer determine the function of the logic gate. The logic output is sensed via an induced voltage due to a switching of the element's magnetization. The concept can be regarded as the predecessor of the concept proposed by Shen (page 25) [15].

A so-called hall effect device [73] has recently been proposed to build the basis of a digital logic [74]. Magnetic stray fields from a magnetic stripe generates a Hall voltage in a semiconducting material which is sensed as the output. The sign of the Hall voltage is determined by the magnetization of the magnetic stripe.

Till now none of these concepts made it to a commercial product. The fact that the advantages of a magnetic logic, namely radiation hardness, nonvolatility of the information, high integration density and low power consumption are differently emphasized in the different concepts might be an explanation. Additionally, the feasibility of complex logic circuits across a wafer has never been shown for some concepts (e. g. bubble logic). On the other hand, work in this field is still in progress. Some results based on the tunneling magnetoresistance are discussed in this thesis.

Remarkable is a concept developed by Goto, a resonant electrical circuit called the parametron [75]. In 1959, about 50 % of the Japanese computers in operation were based on the parametron. Taking along the fact, that semiconductor based circuits are not the only concepts for a digital logic with the potential for a commercial product, the next section addresses digital logic based on the magnetoresistance effects.

### **3.1 Programmable logic based on magnetoresistance**

Apart from the exploration of giant magnetoresistance and spin-dependent tunneling (SDT) for use in read heads, sensors and memory devices, different concepts have been proposed to develop magnetic logic circuits using these physical effects [13] [15] [14] [16] [17] [20]. In these schemes thin magnetic film devices are used in conjunction with semiconductor based circuits to amplify the output signals to use as new inputs. For this magnetoresistive-logic (MR-logic) one gains the advantages of magnetic thin film elements, e. g. nonvolatility, low power consumption, the possibility of fast operation, radiation hardness and non-destructive readout. Furthermore, programming such a semiconductor-thin magnetic film hybrid into a particular function is straightforward. Programmable MR-logic can be categorized in two parts: (a) mask programmable MR-logic, in which the logic function is defined in (ideally) one process step during the fabrication process, and (b)



field programmable MR–logic, which can be programmed on–chip in a nonvolatile way. Future possibilities could also include the use of such circuits either as memory or as logic depending on the specific needs of the operations to be performed.

The digital character of the resistive states of the MR elements is essential for the logic principle. Fluctuations in the input signal do not change the resistance state of a (suitable, see later) MR element and hence do have no impact on the amplified output signal. Thus these principally not preventable fluctuations do have no impact on complex logic circuits based on MR–logic gates connected in series.

The amplifier circuitry is needed to convert the output signal of the magnetoresistive part of a logic gate to a signal which can serve as logic inputs for subsequent logic gates. These inputs are magnetic fields sufficiently large to switch the soft magnetic layers of the MR elements (for one concept the reference layer is switched, too). For a *GMR* based logic a magnetoresistance of at least 800 % at room–temperature would be needed to make the amplifier unnecessary (*TMR* is worse) [7]. Hence state of the art magnetoresistive systems without semiconductor amplifiers at the output of each logic gate are not capable to built up a digital logic.

Worth to mention is a concept for programmable logic gates proposed by S. D. Bader and coworkers [76]. Theoretically, the magnetic layers of a SDT like element can be switched by applying a voltage across the tunneling barrier. In principle, the output of such a gate could be directly used for new logic inputs. There is an experiment reported on the voltage dependence of the magnetic state in SDT elements, but a logic device has not yet been realized.

### 3.1.1 Mask programmable logic

Mask programmable devices are programmed only by the manufacturer. An example is the Programmable Read Only Memory (PROM). The programming of the logic function is often done by defining the connections between inputs, logic gates (OR/AND gates in the simplest cases) and outputs of the logic circuit. For instance, the Mask Programmable Gate Array (MPGA) was developed to handle larger logic circuits. Again the definition of the interconnections is used to implement desired logic function.

Shen [15] and Frank [22] suggested a concept for a mask programmable magnetic logic, in which the function of the fundamental logic gates (OR, AND level) are programmed via one mask used in the fabrication process. A single MR element with sharp switching transitions between the low and high resistance states which are typical for coherent rotation of the corresponding magnetic layer forms the basis of the logic gate.

In Figure 3.1 (a), the basic logic gate is shown. A so called word line runs on top of

the MR element and is insulated from it. When a current passes through that line, the generated magnetic field can switch the magnetizations of the magnetic layers and thus switch between the two resistance states of the MR element. The two resistance states of the MR element form the Boolean 0 and the Boolean 1 output of the logic gate. In operation, a constant voltage or current is applied across the MR element. An amplifier circuitry sensing the current/voltage across the MR element converts then the Boolean output to the current/voltage value of the corresponding Boolean input. The Boolean input is a magnetic field generated by a current in the word line. Before a logic operation, the resistance of a logic gate is set to a

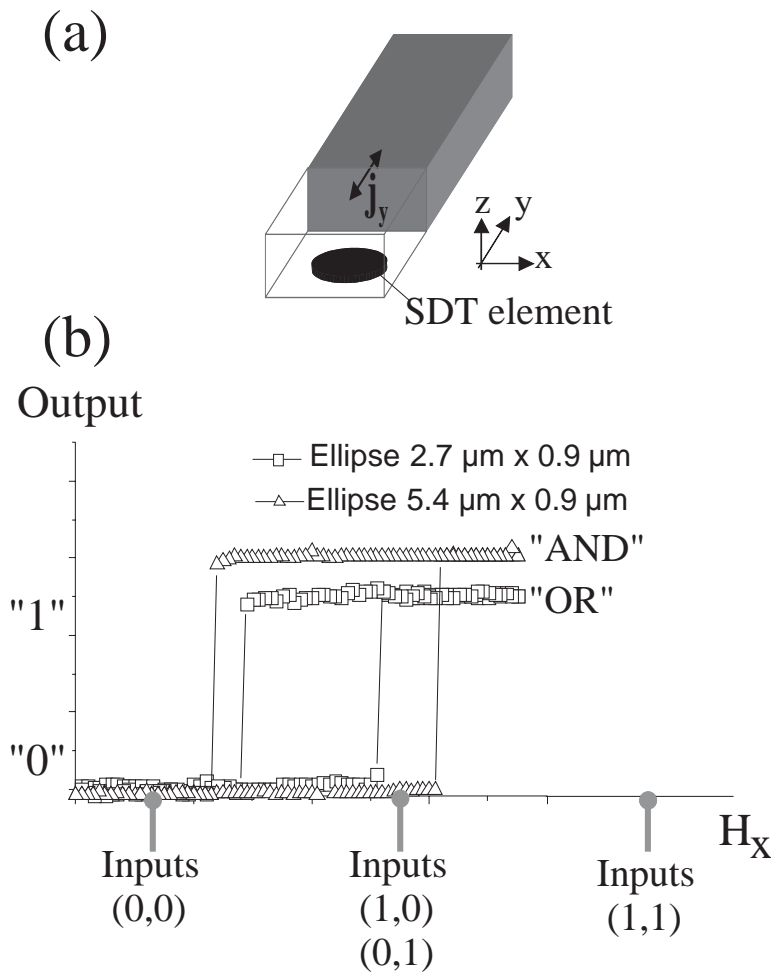


Figure 3.1: (a) Geometry word line (logic inputs) – SDT element of a logic gate. The current line is electrically isolated by  $\text{SiO}_2$  from the SDT element. All inputs (currents) flow through the word line, hence a resulting magnetic field is generated at the location of the SDT element. The current line for the bias magnetic field, the electrical contacts of the SDT element and the subsequent amplifier circuitry are not shown. (b) Minor loops of two elliptically shaped SDT elements. The presentation is shown in terms of a logic gate: High and low resistance states correspond to logic output 1 and 0, respectively. The magnetic field is expressed in terms of the logic inputs. The switching field of the soft magnetic layer and thus the logic function is adjusted by the shape anisotropy of the SDT element.

defined state by a reset signal (e. g. Boolean 0). Subsequently the logic inputs are applied to the logic gate via currents through the word line. Principally, the design of the fundamental logic gate can be chosen such that each logic input is applied via a separate word line. The logic function of a fundamental gate is determined by the combinations of Boolean inputs (currents) applied simultaneously to the word line which lead to a change of the resistance state (Output) of the logic gate (then Boolean 1). Once the currents/voltages corresponding to Boolean 0 and 1 are defined for a chip, the logic function of a fundamental gate is programmed by adjusting the coercivities of the magnetic layers that form the MR element. If this adjustment can be performed while keeping all other parameters (magnetoresistance, resistances of element, its contact lines, word lines, etc.) the same, one prevents more semiconductor periphery per fundamental logic gate.

The coercivity of a given thin magnetic film with fixed thickness can be adjusted by the shape and the aspect ratio of the MR element. A detailed experimental study on the impact of the shape anisotropy on the switching behaviour of typical NiFe-layers as used in MR elements and on the material stack is described on page 65.

Figure 3.1 (b) shows exemplarily for SDT elements the feasibility of programming a two input logic gate via the shape anisotropy. With defined magnetic field values for input and output Boolean 1 and Boolean 0, an elliptically shaped  $5.4 \mu\text{m} \times 0.9 \mu\text{m}$  SDT element forms an AND gate, an elliptically shaped  $2.7 \mu\text{m} \times 0.9 \mu\text{m}$  SDT element forms an OR gate. In Figure 3.1 (b), input Boolean 0 correspond to a current with opposite polarity than the current that corresponds to Boolean 1.

The verification of the feasibility of the mask programmable logic is not yet complete. So far it was shown that the switching field of the soft magnetic layer can be adjusted by choosing the aspect ratio of elliptically shaped SDT elements or defining one mask, respectively. From the measurements described in the section concerned with the shape anisotropy (page 65) it is concluded, that the switching fields can be adjusted while keeping the tunneling area (hence resistance of the MR element) constant. A problem is the reproducibility of the switching fields of nominal identical SDT elements. For nominal identical SDT elements, there is a significant fluctuation of the measured coercivities (Figures 6.3 and 6.4). For a working digital logic based on the fundamental logic gates discussed with global uniform definitions of inputs and outputs, the degree of fluctuations has to be decreased. Possible sources are the fabrication process (e. g. boundaries of the SDT elements) and the material system (e. g. reference layer) itself.

Shown so far is the programming of the AND/OR functions. For the INVERTER–NOR–NAND group, Shen [15] suggests the inversion of the current flow in the word line (change the polarities of the word line contacts). That means that the programming is not only performed via the mask that defines the MR elements. Additional

mask(s) have to be redesigned for a special programming. For the (NOT) EXclusive-OR ((N)XOR) gate a on-chip-switchable (programmable) reference layer is needed. As discussed for spin-logic gates (page 32) magnetic stability (page 97) of the programmable reference layer is a problem.

Finally two ideas/improvements for the concept: Once a working programmable reference layer is established, its magnetic moment could be used to program between AND/OR and INVERTER/NAND/NOR groups.

Instead of adjusting the coercivities for programming, one could also vary the cross-sectional area of the word lines with the consequence of a variation of the current densities and hence a variation of the magnetic field acting on the magnetic layers at constant current (see Figure 7.2). When the logic inputs are defined by currents this is a way to (mask)program a logic gate.

### 3.1.2 Astroid-logic

The Astroid logic device [17] [18] [19] utilizes the switching behaviour of single domain (like) particles which is characterized by a so-called astroid [48]. The fundamental logic gate is shown in Figure 3.2 (a) and consists of a MR element and two current lines orientated perpendicular to each other and electrically insulated from the MR element. With currents through these lines one can address the magnetic layers of the MR element with an in-plane magnetic field. Logic inputs and output are defined as for the concept of the mask programmable logic namely by easy anisotropy axis magnetic fields and the resistance state of the MR element. To serve as new inputs for subsequent logic gates, the output signal has to be amplified by semiconductor based circuitry.

The astroid-logic is a user programmable (field programmable) concept. Programming is performed via the bias magnetic field as explained in Fig. 3.2. Details about the tunneling system are given on page 65.

The number of adjustments of the bias magnetic field (number of programming cycles) is in principle not limited. The programming information could be stored in an additional MRAM cell in a nonvolatile way. The definition of the bias magnetic fields for programming are freely eligible with the boundary condition that the switching of the soft magnetic layer must be performed by rotation, since this leads to magnetic stability and faster switching.

The NXOR function could be implemented with a programmable reference layer and a third (biggest) bias magnetic field that ensures switching of both the soft magnetic layer and the reference layer when Boolean (0,0) and (1,1) are applied to the inputs. Such a programmable reference layer could also be utilized to (field)program between the INVERTER/NAND/NOR and AND/OR groups.

Problems of the concept are similar to those discussed for the previous mask programmable concepts like the reproducibility of switching behaviour, respectively astroid for nominal identical MR elements.

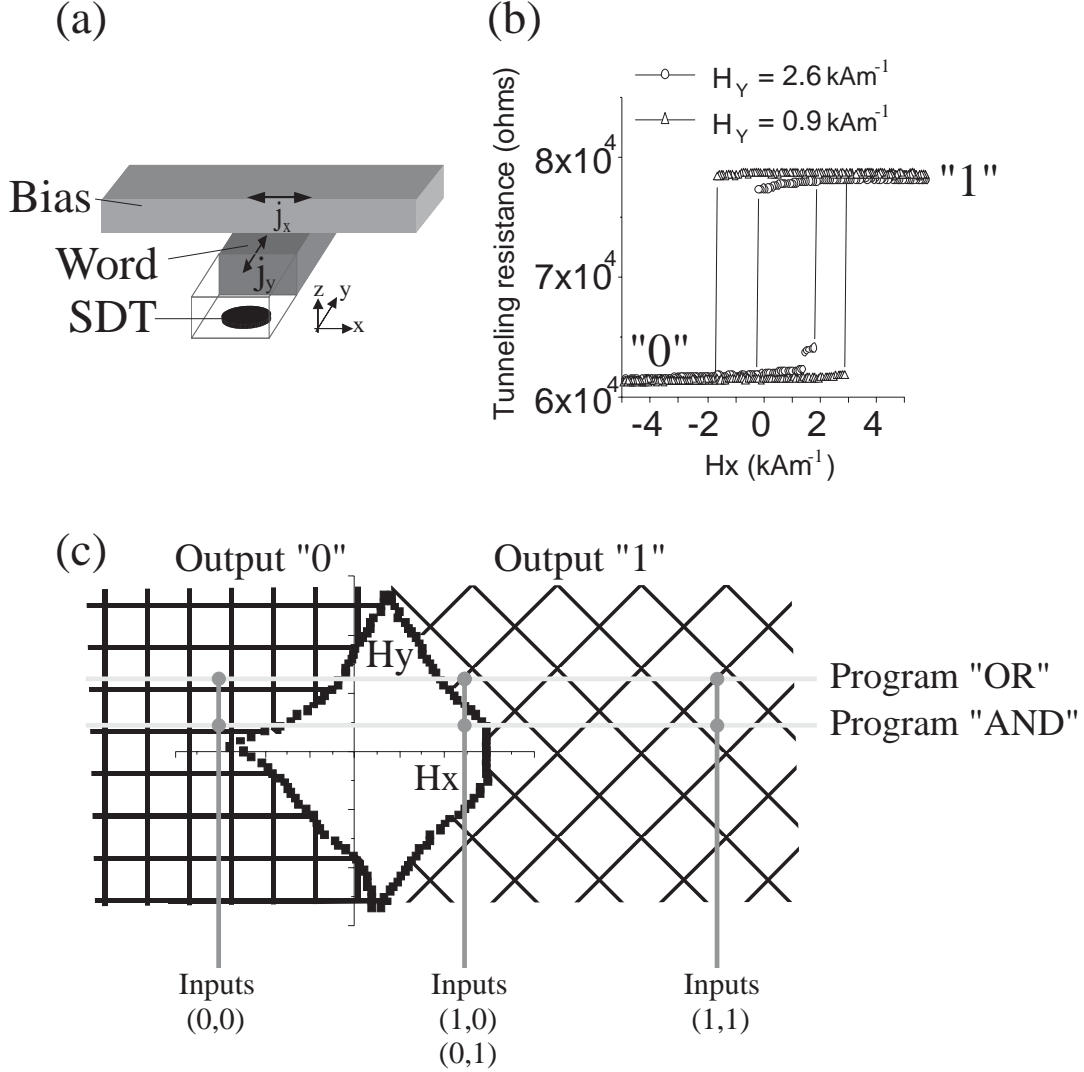


Figure 3.2: (a) Geometry word line (logic inputs) and bias magnetic field line – SDT element of a logic gate. The current lines are electrically isolated by  $\text{SiO}_2$  from the SDT element and from each other. (b) Minor loops of an  $2.8 \mu\text{m} \times 0.7 \mu\text{m}$  elliptically shaped SDT element for two bias magnetic fields of different magnitude. The switching field of the 6 nm thick, soft magnetic NiFe layer is adjustable via the bias magnetic field. Hence the logic function of the fundamental logic gate can be programmed via the bias magnetic field. (c) Measured astroid of the SDT element in (b) in the presentation of a logic gate: high and low resistance state correspond to logic output 1 (area right from the astroid) and 0 (area left from the astroid), respectively. The magnetic field  $H_x$  along the long (easy) axis of the SDT element is expressed in terms of the logic inputs. The switching field of the soft magnetic layer and thus the logic function is adjusted by the bias magnetic field. The magnetic field scan of the minor loop measurements shown in (b) are visualized in (c) by the grey lines ( $H_y = \text{constant}$ ). Changing the bias magnetic field from  $0.9 \text{ kAm}^{-1}$  to  $2.6 \text{ kAm}^{-1}$  programs the logic gate from the AND to the OR function in this example.

### 3.1.3 PML–logic

The PML–logic (Programming Magnetic Layer) [21] utilizes the impact of the edge magnetic stray field from an additional magnetic layer in the tunneling stack on the switching fields of the magnetic layers that form the MR element for programming. Figure 3.3 explains the principle of the fundamental PML–logic gate.

For distances typical in MR elements discussed here (thickness of the complete stack  $\ll$  width and length of the element), the in–plane magnetic stray field scales with the demagnetizing field (page 65) and scales hence linearly with the magnetic moment ( $\propto M_s \cdot \text{thickness}$ ) of the magnetic layers. A 1 nm thick,  $1.5 \mu\text{m} \times 0.9 \mu\text{m}$  elliptically shaped  $\text{Co}_{50}\text{Fe}_{50}$  layer ( $M_s=1800 \text{ kAm}^{-1}$ ), magnetized along the long axis, causes an in–plane magnetic stray field of  $0.8 \text{ kAm}^{-1}$  and shifts the minor loop by that amount.

The coercivity of the PML must be bigger than the coercivity of the soft magnetic layer, because its magnetic stray field must cause a shift of the minor loop. On the other hand, the PML must be switchable by a current on–chip for a field programmable PML–logic. These boundary conditions vary with the geometric parameters of the MR element and geometry MR element–magnetic field generating current lines (Fig. 7.2).

From the typical magnitudes of coercivities, stray fields and magnetic fields generatable by a current on–chip, a PML–logic gate should be possible. The system  $\text{Ru}/\text{Co}_{50}\text{Fe}_{50}$  (Fig. 7.4) for the PML offers the possibility to adjust the coercivity between  $5 \text{ kAm}^{-1}$  and  $45 \text{ kAm}^{-1}$  with reliable freedom to choose the thickness of the  $\text{Co}_{50}\text{Fe}_{50}$ .

Similar to the concepts discussed so far, a programmable reference layer opens the possibility to program between the NAND/NOR group and the AND/OR group within the magnetic part of a logic gate.

An NXOR function can also be realized with an programmable reference layer.

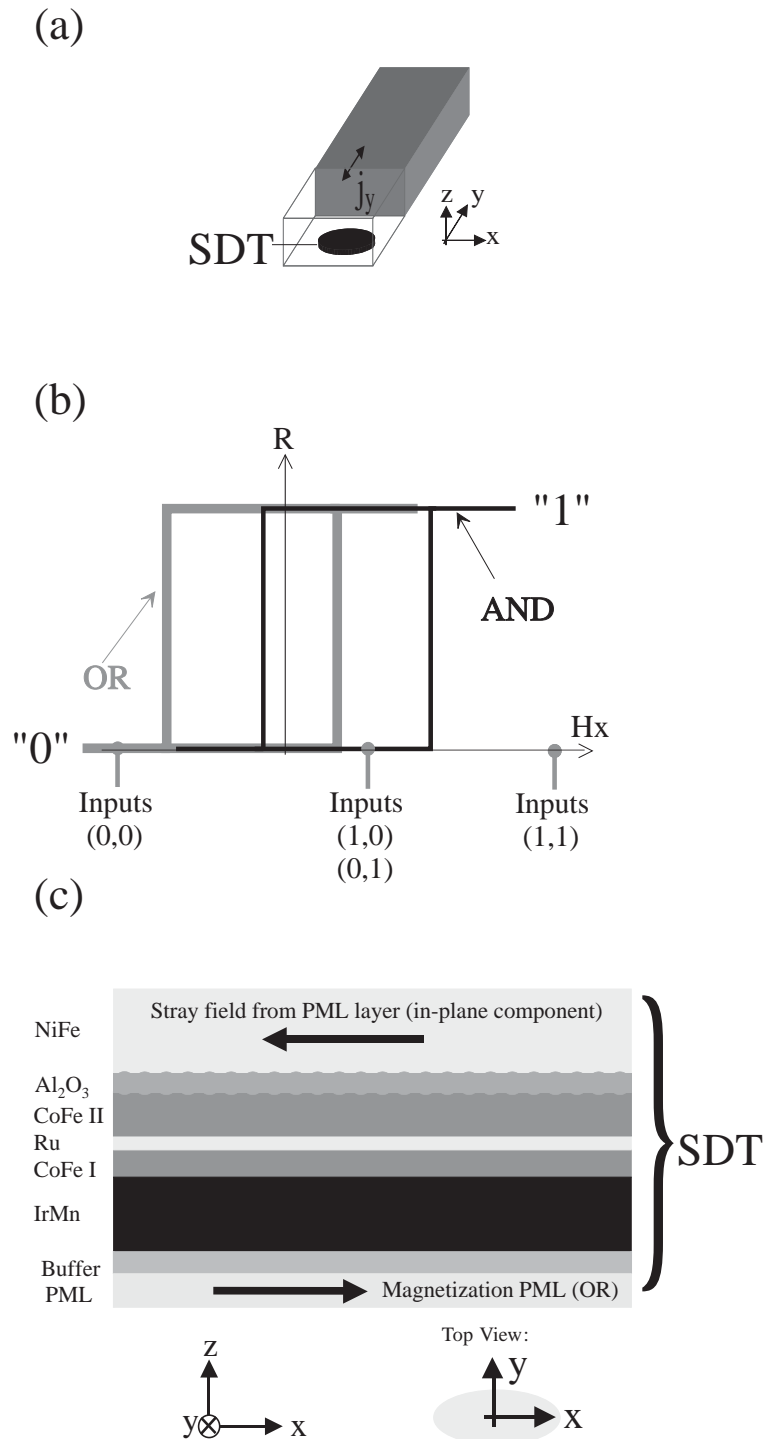


Figure 3.3: (a) Geometry word line (logic inputs) – SDT element of a PML–logic gate. The current line is electrically isolated by  $\text{SiO}_2$  from the SDT element. The current line for the bias magnetic field, the electrical contacts of the SDT element and the subsequent amplifier circuitry are not shown. (b) Schematic minor loops of a SDT element with a single domain like soft magnetic layer for the two programming options of the programming magnetic layer. (c) Principle tunneling stack of the PML–logic with exchange biased AFi reference layer system. The Programming Magnetic Layer is placed at the bottom of the tunneling stack. Its edge magnetic stray field causes a shift of the minor loop which is utilized for programming the logic gate. The PML's magnetization must be stable when switching the soft magnetic layer.

### 3.1.4 Spin–logic

#### The concept

The concept of spin–logic was introduced by Hassoun and coworkers in 1997 [14]. A spin–logic gate consists of magnetoresistive elements acting as reference and logic input bits. The architecture of a three input spin–logic gate consisting of six SDT elements is shown in Figure 3.4.

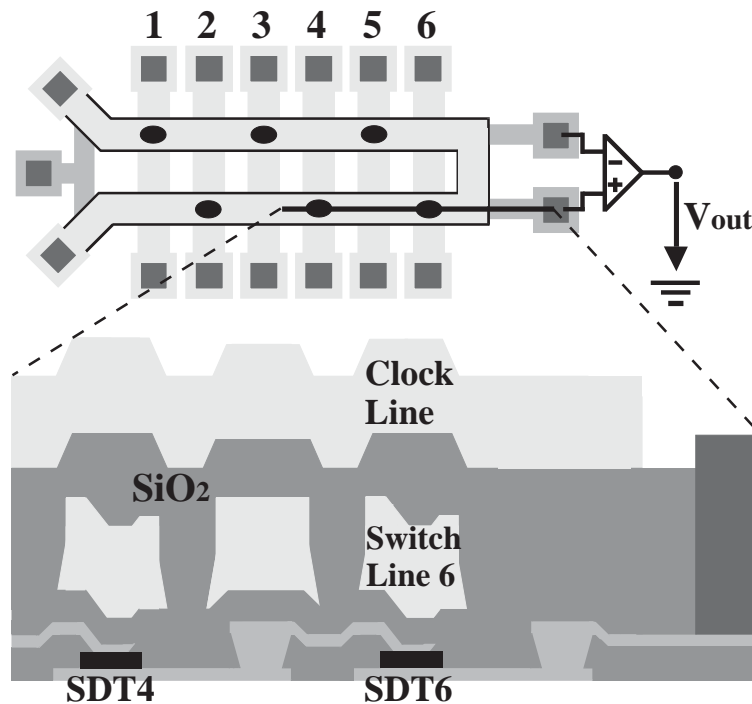


Figure 3.4: Top: design of a three input field programmable spin–logic gate. Bottom: schematic cross section through the device along the black line in the top. The SDT elements are separated by  $\text{SiO}_2$  from the switch lines (1–6) and the clock lines.

The SDT elements are arranged in two sense lines and are connected in series within a sense line. The SDT elements can be addressed independently by a current in a switch line (No. 1–6) which generates a magnetic field to switch the soft magnetic NiFe layer and hence the corresponding SDT element between its high and low resistance states. The switch lines are electrically insulated from the SDT element circuitry by  $\text{SiO}_2$ . A clock line runs on top and perpendicular to the switch lines. The astroid switching characteristic is utilized for this principle of a clock. A current in this line generates a bias magnetic field. The switch and the clock lines are electrically isolated from each other.

The logic output of a spin–logic gate is defined by the difference of the resistances of the two sense lines formed by the SDT elements. That difference is sensed via



applying constant voltages to each line and measuring the difference of the tunneling currents or applying constant tunneling currents to each sense line and measuring the differential voltage. Here only the voltage sense mode is discussed. As shown in Figure 3.4, a sense amplifier converts the differential voltage to a signal which serves as input signals for subsequent devices. The logic input signals  $I(0)$  and  $I(1)$  that corresponds to Boolean 0 and Boolean 1 are currents in a switch line (or voltages applied to the switch lines) that are capable to change the resistance of the addressed SDT element between the high and low resistance state. A changed resistance of a SDT element consequences in a change of the differential voltage to be amplified. The sense amplifier is designed to distinguish two regions of differential voltages  $U_{Diff}$ . For voltages  $U_{Diff} < U_{Diff,0}$  the output signal of the spin-logic gate is  $I(0)$  (Boolean 0), for voltages  $U_{Diff} > U_{Diff,1}$  the output signal of the spin-logic gate is  $I(1)$  (Boolean 1). Hence the change of the resistance of a SDT element is accompanied by a change of the differential voltage but not necessarily by a change of the logic output signal. Due to noise the sense amplifier is not free of errors. To distinguish the two regimes of differential voltages unambiguously,  $U_{Diff,0}$  and  $U_{Diff,1}$  must be separated by a gap  $G$ . For state-of-the-art sense amplifiers,  $G = 1$  mV is sufficient but for on-chip integrated sense amplifier circuitry at high integration density, a gap  $G$  of 20–40 mV is necessary [77].

In operation, these SDT elements that are arranged in one sense line are defined as input bits and these in the other sense line serves as programming (reference) bits. The choice of the input bits is principally not restricted to one sense line and to a fixed number for a spin-logic gate. Programming is not only the choice of the logic input bits (information stored in switches, e. g. MRAM plus transistor) and the adjustment of the reference bit's resistance. Programming information can also be stored in the reference layers of the input bits. Once the reference layer system is switchable by a current on-chip, it can also be used for programming. But first of all, spin-logic gates with a not programmable reference layer system are discussed. Figure 3.5 shows the programming example of a two input spin-logic gate which consists of four SDT elements.

The programming of a spin-logic gate can be categorized in two parts. Programming can be performed in the magnetic part of a spin-logic gate (the gate in figure 3.4 without the amplifier circuitry) or in the electronics around it. The magnetic part is regarded in Figure 3.5. Via the adjustment of the tunneling resistance of SDT element 3 and 4, the spin-logic gate can be programmed between the NOR/NAND basic functions. The possibility to use also electronics which can be affiliated to the spin-logic gate (current sources, offset voltage of the sense amplifier, switches) for programming opens more programmable logic functions per spin-logic gate at the expense of more semiconductor components. The possibility to program the

polarity of the currents allows to choose if a Boolean input 1 corresponds to the high or low resistance state of the addressed bit. Hence a spin–logic gate then can be programmed between the NOR/NAND/AND/OR basic functions. The possibility to adjust the offset of the sense amplifier (which corresponds to the positioning of the gap  $G$ ) and the use of switches which allows a variable connection of input and programming signals to the switch lines and hence to the corresponding SDT elements consequences in a further increase of the programmable functions per spin–logic gate e. g. Minority, Majority and more complex logic.

Within the group of more complex combinatorial logic functions, also those with distinguishable input bits are included (e. g.  $(A \text{ AND } B) \text{ OR } C$ ). The logic function which cannot be realized with spin–logic gates is the EXclusive OR (XOR). Generally, the number of logic inputs is variable, too.

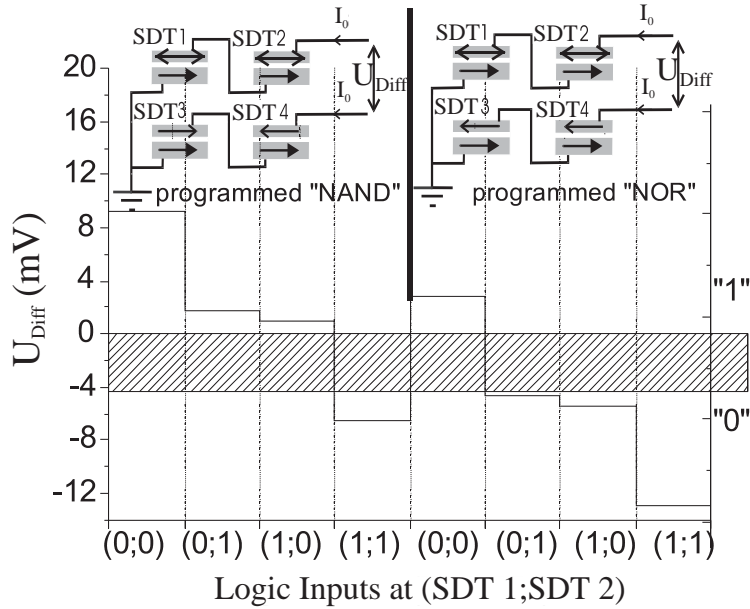


Figure 3.5: Programming example of a spin–logic gate that consists of  $2 \times 2$  SDT elements. SDT elements 1 and 2 are chosen as input bits. Differential signal  $U_{Diff}$  (logic output to be amplified) versus the permutations of Boolean inputs. Logic outputs 0 and 1 are separated by the grey area. A schematic of the field programmable logic gate is shown in the top of the figure. Arrows indicate the direction of magnetization of the layers adjacent to the tunneling barrier. The high and low resistance states of SDT element 3 are used for programming the gate to form a NOR or a NAND function.

As a conclusion spin–logic is a hybrid of semiconductor devices and magnetoresistive elements. The semiconductor circuitry is first essential for spin–logic to be an active digital logic, which means that the output can be used for inputs of subsequent devices. Secondly, semiconductor components expand the group of programmable logic functions per spin–logic gate drastically as exemplified for a two input gate.

Especially switches (e. g. MRAM plus transistor) that mix and match the input and programming signals to the switch lines are important for more complex logic functions.

As a rule of thumb, it is favorable to increase the degrees of freedom of the magnetic part of the spin–logic gate. More degrees of freedom consequences in a higher number of programmable logic functions per spin–logic gate mediated via its magnetic part. A programmable reference layer system is an example, as illustrated in table 3.1. With the introduction of a programmable reference layer system, one can spare the electronics that changes the polarity of the currents through the switch lines. If this is an advantage for a commercial product is not considered here and depends on the effort on electronics needed to establish this additional class of programming.

| Not programmable reference layer system | Programmable reference layer system |
|---|-------------------------------------|
| NAND, NOR                               | NAND, NOR, AND, OR                  |

Table 3.1: List of the basic programmable logic functions of a two input spin–logic gate realizable with its magnetic part.

The physical requirement to be fulfilled by the programmable reference layer is magnetic stability as investigated in the corresponding chapter for the system Ru/CoFe [55].

Magnetic device mismatch and its impact on the functionality of spin–logic gates is discussed later in the framework of the experiments performed.

According to reference [25], spin–logic gates open the possibility to an application which is currently investigated for Field Programmable Gate Arrays (FPGA’s), namely reconfigurable computing. In this application, the programming of a logic circuit is optimized for the given problem to calculate. In some cases significantly improved computational results are achieved compared to state–of–the–art processors, which are not programmable. Since many and different problems are to be calculated, the programming must be performed fast in order to have a benefit. Furthermore the concept of software is different, usual software is written to solve a problem, reconfigurable computing software has first to optimize the hardware, solves the problem, optimizes the hardware for the next problem, and so on..... (hardware gets software).

Properties being prerequisites for reconfigurable computing are fulfilled by spin–logic gates, namely that a programming operation can be performed fast and that there is no practical limitation of programming cycles, which is fulfilled when using an appropriate magnetic layer system fulfilling the demands of the switching stabil-

ity. How fast the programming of a complex spin–logic circuit can be performed is not known, but the nonvolatility of the programming information within spin–logic suggests this procedure to be faster than for state–of–the–art FPGA’s [25].

Beside the programming information, the logic inputs and outputs are nonvolatile in the spin–logic gates.

As magnetoresistive system for the field programmable spin–logic gates tunneling systems were chosen in this work, since a tunneling system exhibits good read–out voltage levels for sub– $\mu\text{m}$  elements and compatibility to nonvolatile memory (MRAM). Drawback of a tunneling system is, that one needs a homogeneous device fabrication process and a barrier with a homogeneous tunneling current distribution on the scale of the tunneling area to fulfill the matching requirements for the resistance and  $TMR$  of the SDT elements forming the field programmable spin–logic gate. For high integration density and high frequency applications, a low tunneling resistance is desirable as it increases the cut–off frequency of the spin–logic gate and the signal to noise ratio (larger tunneling currents). On the other hand the power consumption for driving the tunneling currents increases with decreasing  $R$ .

### **FPGA’s, an application for spin–logic gates**

Field Programmable Gate Arrays were introduced by Xilinx Inc. in 1985. The FPGA is the further development of the MPGA. In contrast to the MPGA, the logic function of the FPGA is defined by the user. There are different categories of FPGA’s currently commercially available. In all of these FPGA’s the interconnections between the core logic blocks (CLB’s) (in the simplest case these are OR/AND blocks) and how they are programmed vary (e. g. SRAM, EEPROM), in more complex FPGA’s also the CLB’s are programmable. The SRAM based FPGA, for instance, has three major configurable elements as shown in Figure 3.6: CLB’s, input/output blocks and interconnects. The input/output blocks provide the interface between the package pins and internal signal lines. The programmable interconnections provide the paths to connect the inputs and outputs of the CLB’s and input/output blocks. Customized configuration is established by programming internal SRAM cells that determine the logic functions and internal connections implemented in the FPGA.

The functionality of spin–logic gates correspond to that of the CLB’s. For a ”magnetic” FPGA, interconnections and parts of the input/output blocks can be realized by switches using MRAM cells, e. g. reconfigurable static latch cells [25] [78].

Conclusively, semiconductor circuitry is essential for a magnetic FPGA. A big part of the programming information is stored in MRAM cells, also within the spin–logic gate in order to program complex functions. For the programming information stored in the soft magnetic layer of the reference bits, there is no physical differ-

ence to the logic inputs stored in the soft magnetic layer of the input bits, hence the difference between the programming action and the logic operation disappears. Thus for this part of the programming information, prerequisites for reconfigurable computing are fulfilled. With the consideration of the rest of the programming information mainly stored in switches, it is expected to be faster than for state-of-the-art FPGA's [25].

The experimental part on spin-logic gates is concerned with their feasibility and the physical properties that have to meet the requirements of the application.

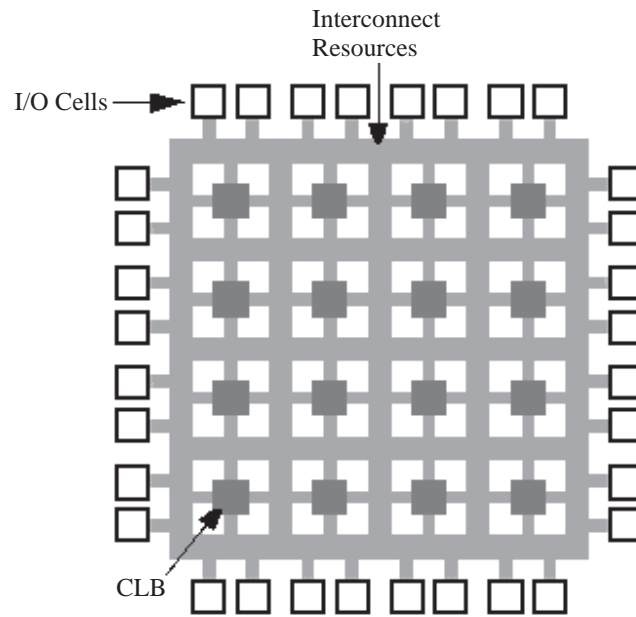


Figure 3.6: Architecture of an complex FPGA [23]. Programmable parts of the FPGA are CLB's, input/output blocks and interconnections.



# Chapter 4

## Sample patterning and Measurement

### 4.1 Fabrication process of spin–logic gates

The growth of the spin dependent tunneling systems was done in a commercial high vacuum sputtering system (For a detailed description of the sputtering process see Reference [79]). The base pressure was  $5 \cdot 10^{-8}$  mbar. Argon was used as the process gas.

In order to prevent currents between the top and bottom electrode through the substrate, the tunneling stack was grown on thermal oxidized Si wafers. All of the metallic layers were sputtered in the magnetron mode. The tunneling barrier was formed by plasma oxidization (Ar/O<sub>2</sub>) of a previously deposited aluminum layer (for tunneling systems sputtered in a Leybold or a Kenotec systems).

The patterning was done by a seven–mask lithography process. The mask set for the programmable logic (PROLOG) was designed (with Layed3<sup>©</sup> software) with the goal to proof the feasibility of different concepts of logic based on SDT elements. PROLOG offers the following features:

- Two–, three– and four input spin–logic gates with SDT elements of variable geometry and width between 0.6  $\mu\text{m}$  and 10  $\mu\text{m}$ .
- Groups of three, nominal identical SDT elements addressable by a 2–dimensional magnetic field via a current on–chip. The SDT elements are rectangular–, elliptically–, or eye–shaped with aspect ratios varied between 1 and 6 and width varied between 0.6  $\mu\text{m}$  and 10  $\mu\text{m}$ .
- Flip-Flops based on SDT elements.
- Arrays of nominal identical SDT elements for the characterization of tunneling systems with respect to the statistical fluctuations of  $TMR$  and  $R$ .

The techniques used in the sample patterning process are:

- Optical lithography
- Sputtering
- Ion beam etching (IBE)
- Reactive ion etching (RIE)
- Oxygen Plasma etching

Optical lithography is performed with a wavelength of 365 nm (Hg I-line) and a standard resist system (AZ5214). The pattern definition of structures down to the minimal length of 600 nm was done by using a trilayer structure that consists of bottom resist/SiO<sub>2</sub>/top resist.

The ion beam etching used for the fabrication of the logic gates makes use of Ar<sup>+</sup>-ions from a plasma. The Ar<sup>+</sup>-ions are accelerated towards the wafer by an electric field. After the acceleration, the beam of Ar<sup>+</sup> is neutralized by an electron beam and hit then the wafer which is therefore not charged up. Areas of the MML which are not protected by resist are removed with a material dependent etching rate due to the transfer of the kinetic energy from the Argon beam to the atoms at the surface. The wafer is rotated along an axis parallel to the Ar-beam in order to have an uniform the etch profile across the wafer.

Reactive ion etching (RIE) makes use of a chemical reaction between a plasma and the material to be etched. The resulting product is volatile. The wafer is placed on the negative electrode with its MML system pointing in the plasma. A plasma initiated with freon gas (CF<sub>4</sub>), for instance, creates fluorine radicals which react well with Si (and SiO<sub>2</sub>). RIE is element selective. Since there is a steady flow of freon in and out of the plasma, the reactants are removed steadily from the wafer.

Another etching tool used for sample patterning is the so called barrel reactor. The wafer is placed out of the oxygen plasma. Oxygen radicals reach the wafer by diffusion and react preferably with organic substances (e. g. resist).



Figure 4.1 explains the origin of the different etching profiles associated with the different etching mechanisms. The etching in the barrel reactor is isotropic (a), since the radicals emerge the wafer after many scattering events with other molecules. With IBE (b), an anisotropic etching profile is achieved, for RIE (b) this is also the case, unless the only reactive partner is protected by the resist. For this case sufficient radicals are present to etch the flanks which results in an anisotropic etching profile.

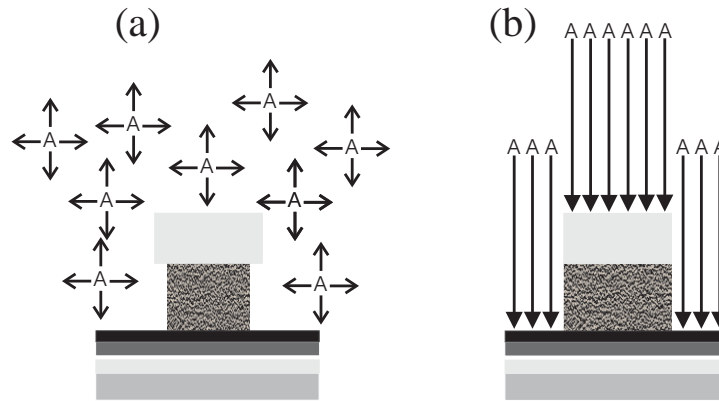


Figure 4.1: (a) isotropic etching by radicals A. (b) anisotropic etching by atoms or radicals (A).

The fabrication process for MRAM [80] forms the basis of the fabrication process for spin–logic gates. As already mentioned, optical (UV) lithography is used to transfer the structure of the mask onto the wafer. Within the standard process, the image reversal photoresist is spin-coated on the wafer with a typical thickness in the order of  $1.4 \mu\text{m}$ . Followed by a baking process, the wafer and the mask are brought close together in a commercial lithography system. The alignment is such, that the light reaches the photoresist on the wafer where the mask is transparent and changes its chemical properties. Next the wafer is wet chemically developed, where the light exposed areas of the resist are removed (positive process). In the negative process, the resist in the shadow of the mask is removed by the developer. This is achieved by a bake which polymerizes the image reversal photoresist exposed to light. Subsequently, the wafer is exposed to light without mask. The developer removes then the regions which are not polymerized.

The lithography is followed by an etching or by a deposition of material on top of the wafer. Depending on the profile at the resist boundaries required, a positive or a negative process (leads to an undercut) is performed. The contrast of the individual masks was chosen with respect to the needed profile.

The sequence of sample patterning of spin–logic gates is shown in the next pictures where the number  $n$  corresponds to the status of the tunneling stack before the use of mask–number  $n+1$ .

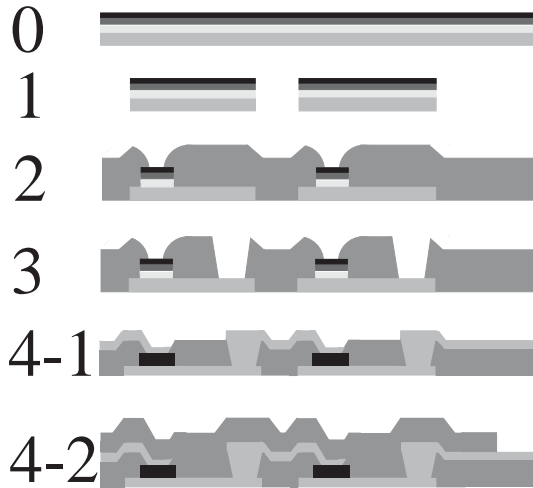


Figure 4.2: Patterning of the MML system till the fifth mask. 0 corresponds to the initial state of the MML.

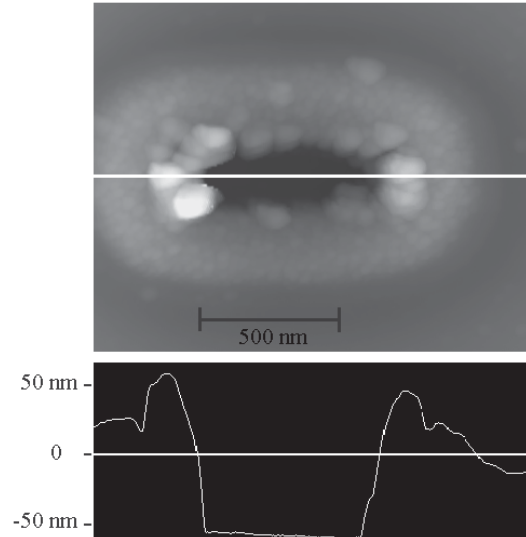


Figure 4.3: AFM scan across a nominal rectangular SDT element. The brightness corresponds to the relative height. The wafer is in the fabrication state No. 3 as shown in Fig. 4.2. The bottom part shows a cross section along the white line.

- (0) in Fig. 4.2 shows the virgin MML system.
- The first mask defines the bottom electrode. In a positive process, resist protects the areas that correspond to bottom electrode. Next not protected regimes of the wafer are etched by IBE down to the substrate ( $\text{SiO}_2/\text{Si}$ ). After the remove of the resist the MML is patterned as shown in (1).
- (2) Patterning of the SDT elements and subsequent steps. For the definition of the SDT elements, a trilayer structure that consists of 500 nm thick bottom resist (diluted AZ5214), 140 nm thick  $\text{SiO}_2$  and 500 nm thick top resist (AZ5205) as shown in Fig. 4.4 is used. In a first step the structure of the SDT elements is patterned in the top resist via a positive process. In order to transfer sub- $\mu\text{m}$  structures, there is a direct contact between the mask and the top resist during light exposure. Next the blank  $\text{SiO}_2$  is etched with freon gas in the RIE. Then both, the bottom resist and the top resist are etched by oxygen in the RIE. Fig. 4.4 (d) shows the SDT element pattern as defined by the  $\text{SiO}_2$  hard mask. Next the so-called undercut is formed by etching the bottom resist underneath of the  $\text{SiO}_2$  in the barrel reactor. This step is the reason for using the trilayer system. In a standard negative process, the strength of the undercut is adjusted by the time the wafer remains in the wet developer. The homogeneity across the wafer and the depth of the undercut

itself cannot be adjusted that accurately to define small (sub- $\mu\text{m}$ ) SDT elements in the resist. Next the SDT element pattern is transferred by IBE in the MML, the etching is stopped after the removal of the magnetic layers (controlled via the etching time). With the hard mask, a redeposition of a mix of resist and etched material is suppressed which can form shortcuts at the side of the SDT element [57]. After the IBE etch,  $\text{SiO}_2$  of 100 nm thickness is sputtered on the wafer which acts as an insulation between bottom and top electrode. In a self aligned process the  $\text{SiO}_2$  passivation is patterned in a lift off process for opening the top electrode. The undercut is the prerequisite of a working lift off process since after the deposition of  $\text{SiO}_2$  not all of the resist is covered by  $\text{SiO}_2$  (g) Hence acetone can crack the hardmask (lift-off) via its resist easily and opens the path to the top electrode (h).

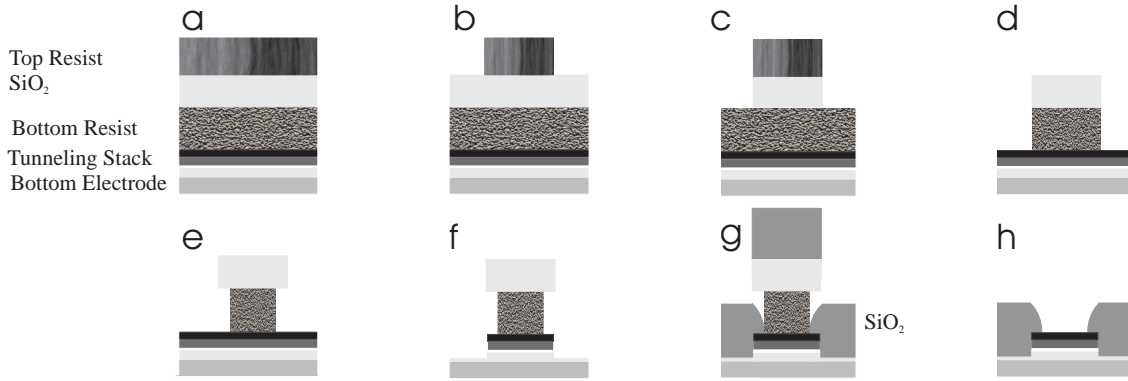


Figure 4.4: Sequence of the patterning of a SDT element via the trilayer process. (a–e) shows definition of the shape of the SDT element in the hard mask, (f) shows the patterned MML followed by the subsequently deposited  $\text{SiO}_2$ -layer (g) and the lift-off process (h).

- Mask No. 3 is used to open a path through the  $\text{SiO}_2$  to the bottom electrode for the serial connection of the SDT elements in a spin-logic gate. The position of the connection points are defined in a negative process and the blank  $\text{SiO}_2$  is etched by RIE.
- The open areas of the top electrodes are patterned via a standard negative process in the resist. Then the sequence Ta5/Cu30/Ta5 is sputtered on the wafer followed by a lift off process. Finally, the top electrode is patterned as shown on 4-1. A tunneling current flows symmetrically through the SDT elements, meaning either always from top to bottom or vice versa. Such an architecture increases the gap  $G$  of spin-logic gates. Next a 140 nm thick layer of  $\text{SiO}_2$  is sputtered on the whole wafer. This is done for insulating the SDT element circuitry from the subsequently deposited magnetic field generating

current lines. Since a contact is needed for the top electrode (and also for the bottom electrode in order to contact the single SDT elements on the wafer), one has to remove the  $\text{SiO}_2$  at the contact points at the end of the fabrication by RIE. In order to prevent a destruction of the top electrode by a long lasting overetching by the RIE, resist caps are patterned with mask No. 7 at the location of the contact points prior to the  $\text{SiO}_2$  deposition. The resist caps and the  $\text{SiO}_2$  on top are then removed by a lift off process for opening the contact points. Thus the total thickness of  $\text{SiO}_2$  to be etched and therefore the etching time at the end are reduced accompanied by a smaller overetching which is principally needed to compensate fluctuations in the etching rate. A contact point to the top electrode is shown at the right end of 4-2.

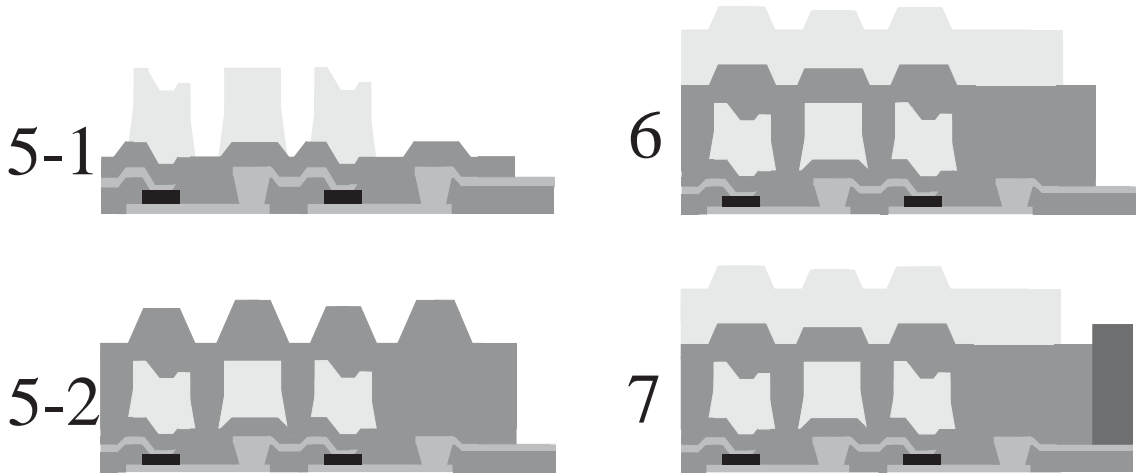


Figure 4.5: Sequence of patterning from masks No. 5 to No. 7

- The magnetic field generating current lines for programing and logic input are defined with mask No. 5 via a negative process. Then Ta5/Cu500/Ta5 is sputtered on the wafer followed by a lift off process. Ta serves for a good adhesion on top of the  $\text{SiO}_2$  and as a protection cap on top of Cu. Next 500 nm of  $\text{SiO}_2$  are sputtered on top of the current lines (5-2), followed by an lift off process that removes the newly sputtered  $\text{SiO}_2$  from the contact points.
- The current line for the bias magnetic field (Ta5/Cu500/Ta5) is patterned with mask No. 6
- Mask No. 7 serves for the definition of the contact points. First the  $\text{SiO}_2$  that covers the bottom electrode (necessary for the single SDT elements) is etched by RIE, then the contact pads (Nb30/Al230) are sputtered on the same resist pattern followed by a lift off process. The final spin-logic gate is shown in Fig. 4.5 (7) and Fig. 4.6.

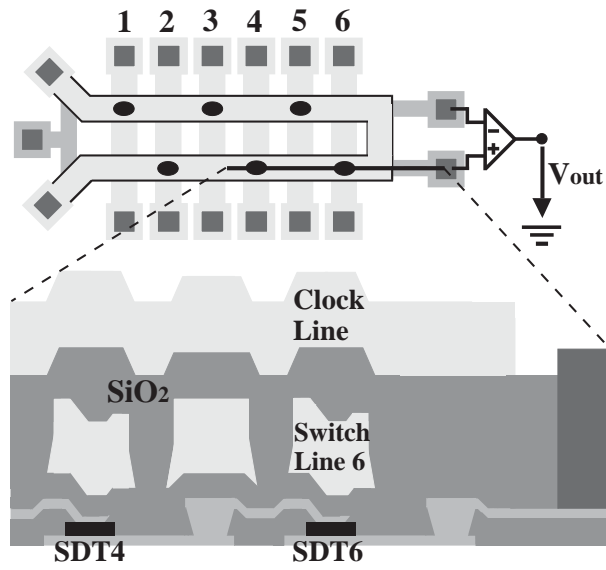


Figure 4.6: Final spin-logic gate

## 4.2 Electrical transport measurement

### 4.2.1 2–point and 4–point measurements

Within a so-called 2–point measurement, the voltage across the contacts plus SDT element is measured. The measured resistance is bigger than the resistance of the SDT element. A two point measurement gives reliable results of  $TMR$  and tunneling resistance, when the tunneling resistance is large compared to the resistance of the contacts. The architecture of a spin–logic gate is such that the output signal is proportional to the difference of the resistances of two lines in which SDT elements are connected in series. The resistances are compared via their voltage levels by the sense amplifier circuitry like in a two–point measurement. In order to increase the gap  $G$  of spin–logic gates, the resistances of the contacts/connections between the SDT elements have to be kept small (via thickness and material of bottom and top electrodes) compared to the tunneling resistance of the SDT elements.

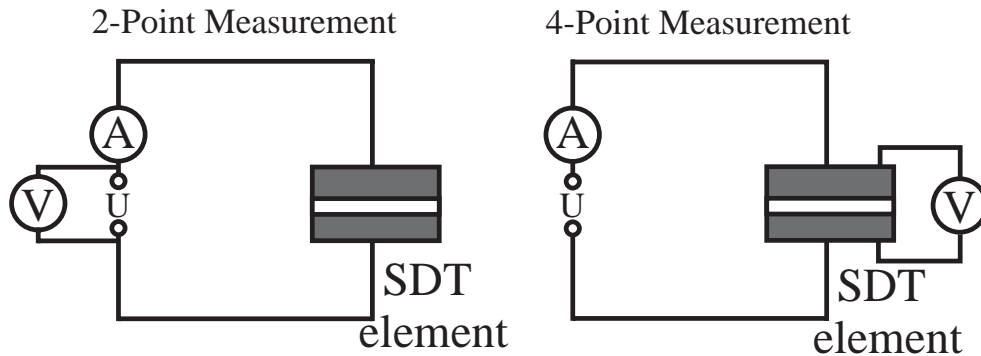


Figure 4.7: Schemes for 2–point (2 contacts at the SDT element) and 4–point (4 contacts at the SDT element) measurement. In a 4–point measurement, the contribution of the contacts to the measured total resistance (voltage) is significantly smaller than in a 2–point measurement.

The design of the mask set offers the possibility of four contact points for single SDT elements. Two contacts (bottom plus top electrode) are used to apply a tunneling current to a SDT element and to measure it, the other two contacts are connected to a voltmeter. Thus the voltmeter does not measure the contribution of the current contacts to the voltage across the SDT element as is the case for the 2–point measurement.

An inhomogeneous tunneling current distribution across the tunneling barrier can, beside other effects [81], cause an enhancement of the measured  $TMR$  with respect to the intrinsic  $TMR$  of the SDT element [82]. Such an inhomogeneous current distribution arises when the resistance of the contacts below the tunneling area is in the order of the tunneling resistance. For the measurements presented in this work, however, the resistance per unit area of both bottom and top electrode were

small compared to the tunneling resistances, hence the via 2-point measurement determined  $TMR$  and  $R$  values are close to the intrinsic values of the investigated SDT elements.

### 4.2.2 Experimental setup

The experimental setup shown in Fig. 4.8 was planned and constructed to perform measurements on logic gates based on SDT elements. The contact pads of bottom-, top-, and magnetic field generating-electrodes are bonded via aluminum wires of diameter  $40\ \mu\text{m}$  to a mobile sample holder. With the bonded sample and the sample holder stucked on its place in the measurement box, the electrical contacts of the device are addressed via the switching box by the electrical equipment. The bonded pads on-chip are contacted by plug panels with the electronic equipment via the switching box. This patch panel opens the possibility to perform variable measurements on bonded devices. The Pi-filter bank filters each signal addressing the SDT elements in the measurement box.

During the first measurements on SDT elements, electrical interference from other equipment (especially switches) and electro static discharge (ESD) turned out to be problem for the SDT elements, since voltages larger than  $1.5\ \text{V} - 2\ \text{V}$  across the tunneling barrier leads to its destruction. One tool to filter out the high voltages due to electrical interference is the Pi filter bank where the cut-off frequency is a compromise between the protection of the SDT elements and the speed of measurement of the setup.

Furthermore the metallic measurement box acts as a Faraday cage, all electrical connections are shielded and the whole setup is located in an additional Faraday cage. Measures performed to prevent ESD during handling the sample are discussed elsewhere [57].

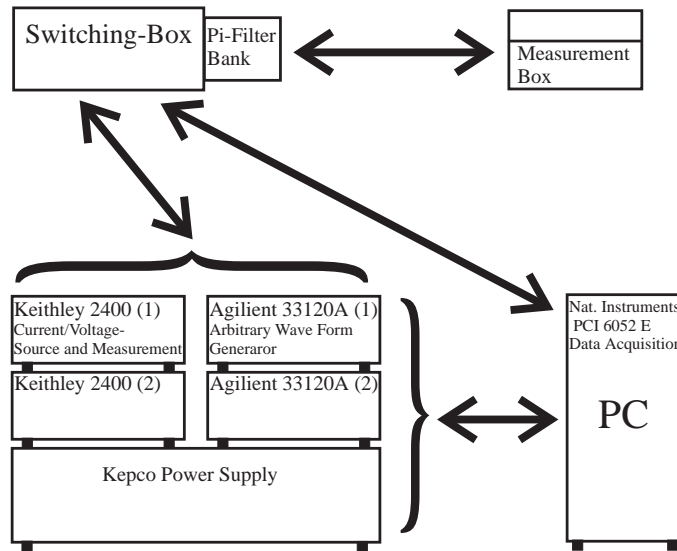


Figure 4.8: Conception of the experimental setup for SDT element based logic.

Two Keithley 2400 Sourcemeters are used to apply and to measure current/voltage of the SDT element circuitry, either in the 2–point or 4–point mode.

The two wave form generators provide the signals (maximal 0.25 A) for the two magnetic field generating current lines which addresses the SDT elements within a logic gate (Fig. 4.6 and Fig. 3.2). The phase between the two signals is adjustable which was utilized to generate a rotating magnetic field on–chip for the measurement in Fig. 8.3 (c). The Kepco power supply is used for higher magnetic fields by amplifying a synthesizer signal. A summary on the calculation of the magnetic field generated by a current is given in Fig. 7.2.

The data acquisition card (maximal sample rate:  $333000 \text{ s}^{-1}$ ) offers many possibilities, the options used are measuring the differential voltage of spin–logic gates and providing an amplified output signal. Furthermore, the voltages across the magnetic field generating current lines for determining the magnetic field acting on the SDT element were measured by the card.

As a summary a list of measurement options of the setup:

- $I - V$  curve of SDT elements
- $TMR$  versus voltage  $V$
- Minor loop and major loop measurements ( $H_{c,ReferenceLayer} < 18\text{kAm}^{-1}$ )
- Astroid measurements
- Measurement on the magnetic stability of tunneling systems (arbitrary 2–D magnetic field, only restricted in its magnitude)
- Characterization of spin–logic gates (dc and "ac")



# Chapter 5

## Spin–logic based on SDT elements

### 5.1 Requirements for the feasibility of spin–logic

Regarding the demands on the material system, there are two additional requirements for spin–logic compared to MRAM. A magnetically very stiff reference layer system is used in MRAM. As discussed on page 32, a programmable reference layer system is advantageous for spin–logic with respect to spare semiconductor electronics. The magnetic stability of the system Ru/CoFe is discussed on page 8. Secondly, the SDT elements that form spin–logic gates have to fulfill the matching requirements with respect to  $TMR$  and tunneling resistance ( $R$ ). The SDT elements that form a spin–logic gate exhibit in the ideal case identical  $R$  and  $TMR$ . If the fluctuations in  $R$  and  $TMR$  within a spin–logic gate are too big, it does not work. Additionally, the higher the  $TMR$  the better for spin–logic, whereas for MRAM the increase of the  $TMR$  beyond values possible in 2001 is not advantageous in terms of sparing semiconductor based electronics. Figure 5.1 shows the voltage levels of  $U_{Diff}$  of a two input spin–logic gate with perfectly matching values of  $TMR$  and  $R$ . The gap  $G$ , which separates Boolean output 1 and Boolean output 0 can be placed between the ideal voltage states, practically below or above 0 mV. The gap  $G$  is globally defined for all spin–logic gates on a chip at the same position. An individual adjustment of  $G$  appears to be too lavish.

Fluctuations in  $R$  and  $TMR$  lead to a splitting of the degenerated voltage levels as shown in Fig. 5.1. If a voltage level lies inside the globally defined gap  $G$ , the spin–logic gate does not work. Small statistical fluctuations in  $R$  and  $TMR$  of the SDT elements that form a spin–logic gate can be tolerated. But if these statistical fluctuations increase, the amount of spin–logic gates with voltage states inside the gap  $G$  increases and hence the rate of not working gates increases. The dependence of the probability  $P$  of working spin–logic gates on the statistical fluctuations is discussed at the end of this chapter. Furthermore,  $P$  increases with increasing voltage step  $\Delta U_{Max}$  when switching a SDT element between its extremal resistance states.



The fabrication was done by a five-mask lithography process. Bottom electrodes were defined in resist and the pattern was transferred by ion milling. Then the tunneling area patterns were defined on a negative resist system and were also transferred by ion milling into the magnetic multilayer system. The etching was stopped in the Cu electrode, hence the Fe6/Cu forms the electrical connection of the SDT elements in a sense line. For passivation, 60 nm of SiO<sub>2</sub> were deposited immediately after the etching. The SiO<sub>2</sub> passivation was then patterned in a self aligned lift off process for opening the top electrode. The Cr3/Cu30/Cr3 top electrodes and the Cr10/Cu200/Cr10 input lines were defined in subsequent process steps. A 60 nm thick SiO<sub>2</sub> layer separates the input lines from the top electrode, hence the inputs are electrically isolated from the SDT elements.

For the two input spin-logic gate, two input lines and the related SDT elements are chosen as logic inputs. The remanent resistance states of the remaining two SDT elements then defines the logic function, hence programming the magnetic part of the spin-logic gate is performed by switching the soft magnetic layer systems. In this demonstration, the shape of the SDT elements forming the spin-logic gate was rectangular, with an tunneling area  $A$  of  $50\mu\text{m} \times 10\mu\text{m}$ . Prior to the transport measurements, the AFi and all other magnetic parts of the SDT elements were saturated in a field of  $800\text{ kAm}^{-1}$ , parallel to the long axis of the elements. The resistance area product ( $RAP$ ) of the SDT elements is  $14\text{ M}\Omega \cdot \mu\text{m}^2$ , and the  $TMR$  is 13.5 % (at 10 mV and at room-temperature) from the minor loop. The switching field of the soft Co1/NiFe6-layer is  $700\text{ Am}^{-1}$  and due to the ferromagnetic orange-peel coupling field the related minor loop is shifted by  $200\text{ Am}^{-1}$ .

The functionality of the spin-logic gate was tested by applying a constant tunneling currents  $I_0$  of  $2.1\text{ }\mu\text{A}$  to each sense line and measuring the voltage  $U_{Diff}$ . For all SDT elements in the spin-logic gate, the net magnetic moment of the AFi points constantly in the same direction. In order to change the resistance state of selected SDT elements and hence to alter the voltage  $U_{Diff}$ , additional currents were applied to the input lines. The voltage  $U_{Diff}$  was measured as a function of the current applied to a single input line while the not selected SDT elements were in their minimal remanent resistance state.

Figure 5.2 shows the results for our field programmable spin-logic gate, reflecting the minor loop of each selected element as a function of the current density  $j$ . For  $j$  below  $-10^{10}\text{ Am}^{-2}$  ( $I = -130\text{ mA}$ ) in an input line, the soft magnetic layer of the corresponding SDT element is switched antiparallel to the net magnetic moment of the AFi. Hence the SDT element is in its high resistance state. Figure 5.2 shows, that both the resistance as well as the magnetoresistance of all four SDT elements are nearly identical. Small differences produce an uncertainty in  $U_{Diff}$  of  $\sim 1\text{ mV}$  which is much smaller than the signal produced by switching one SDT element.

As a consequence of the well matching properties of  $TMR$  and  $R$  of the SDT elements forming the spin-logic gate, a gap  $G$  of 4.5 mV separates the voltage states.

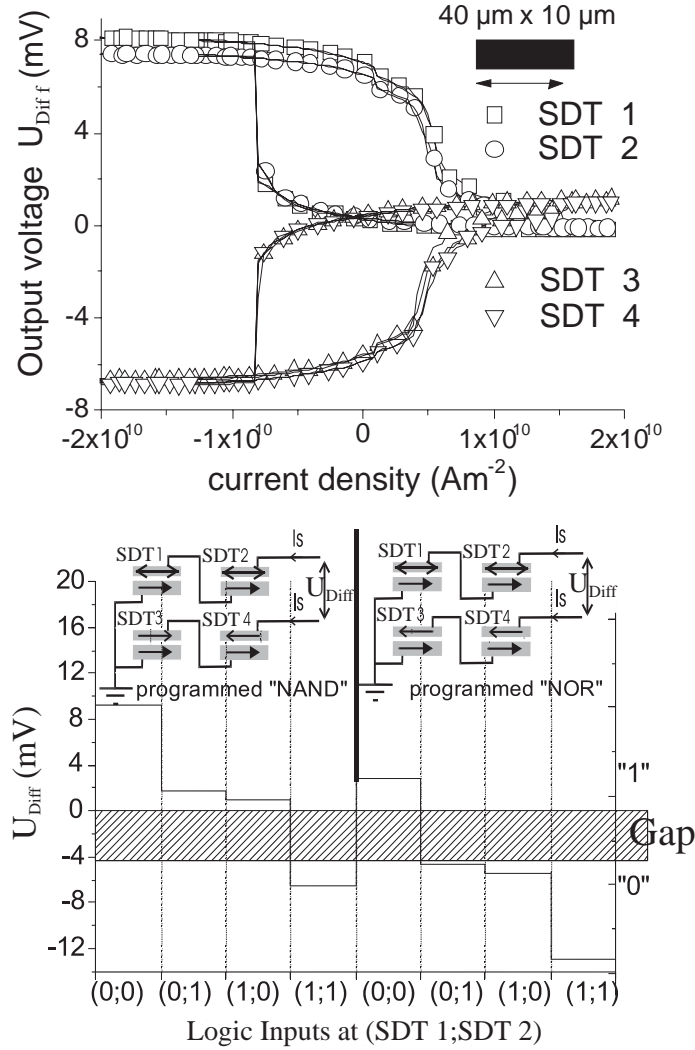


Figure 5.2: Characterization of the spin-logic gate operated at tunneling currents  $I_0$  of  $2.1 \mu A$ . The voltage  $U_{Diff}$  is measured as a function of the current density in the switch line of the selected element. Bottom: Programming example of the spin-logic gate. SDT element 1 (SDT1) and SDT2 are chosen as logic input bits. The voltage  $U_{Diff}$  versus the permutations of input signals is shown.  $U_{Diff} < -4,5$  mV is defined as logic output 0,  $U_{Diff} > 0$  mV as logic output 1. For the programming bits SDT3 and SDT4, the orientation of the net magnetization of the AFi relative to the magnetization of the soft magnetic layer is shown for two programming options of the spin-logic gate.

To demonstrate the principle of the spin-logic gate, logic inputs and outputs are now defined. A current density of  $-2 \cdot 10^{10} \text{ Am}^{-2}$  in a logic input line corresponds to a logic input 1,  $+2 \cdot 10^{10} \text{ Am}^{-2}$  to logic input 0. These current densities are able to switch the SDT elements between their maximal and minimal resistance states and are also used for programming. For the logic output we chose the gap

marked in Fig. 5.2 (lower part) below 0 mV to separate Boolean 0 and Boolean 1. A voltage of  $U_{Diff} > 0$  mV corresponds to logic output 1 and  $U_{Diff} < -4.5$  mV to logic output. Again, this gap  $G$  between logic output 0 and 1 is valid for any of the programming options which can be deduced from figure 5.2 by considering that programming a SDT element corresponds to the remanent resistance state following the programming action and that logic input corresponds to the extremal resistances of a SDT element. As a programming example concluded from the results in figure 5.2 (top), figure 5.2 (bottom) shows the performance of the spin–logic gate when SDT element 1 and SDT element 2 are chosen for logic input: the magnetic part of the spin–logic can be programmed as a NAND or a NOR gate. If one of the programming SDT’s is in its high remanent resistance state and the other in the low one, the spin–logic gate is programmed as the NAND function, if both, SDT 3 and SDT 4, are in the high remanent resistance state, the gate acts as the NOR function.

For perfectly matching SDT elements, the gap  $G$  between logic output 0 and logic output 1 roughly equals the product of the  $TMR$  value and the applied voltage across a single SDT element. In figure 5.2, the measured value of  $G$  is approximately 4.5 mV, where one would expect 7.8 mV. The margin is narrowed for several reasons: (1) the remanent states of the SDT elements have a resistance different to the corresponding saturation values (no single domain like switching behaviour of the soft magnetic layer), (2) mismatch of both  $TMR$  values and tunneling resistance values of the nominal identical SDT elements forming the spin–logic gate. Furthermore, asymmetry of  $TMR$  versus applied voltage may arise due to different densities of (tunneling) electron states (DOS) on both sides of the tunneling barrier [39]. This asymmetry has to be considered when discussing origins of mismatch in the resistances of the first spin–logic gate, since in the first design (figure 5.1) the tunneling current  $I_0$  flows from top to bottom electrode for one SDT element and from bottom to top for the other one.

The gap  $G$  of 4.5 mV at corresponding tunneling currents  $I_0 = 2.1 \mu\text{A}$  is not the upper limit of the gap  $G$  for the spin–logic gate (maximal voltage step  $\Delta U_{Max}$  at  $I_0 = \sim 10\mu\text{A}$ ).

Regarding the use in a FPGA, the size of the spin–logic gate has to be decreased (FPGA’s are currently fabricated down to  $0.18 \mu\text{m}$  minimal feature size). With smaller element size and the same thickness of the magnetic layers, the shape anisotropy starts to dominate the switching behaviour of magnetic layers, with the consequence of remanent resistance states closer to the extreme values. With smaller area of the spin–logic gate, the mismatch due to the global gradient in  $R$  across the wafer decreases. These effects consequence in a bigger gap  $G$  of a spin–logic gate. On the other hand, if local conducting centers (hot spots) dominate tunneling, the

variation of both  $R$  as well as  $TMR$  could become larger with smaller tunneling area. This, however, has to be avoided anyway for a working spin–logic gate. A further resource for increasing  $G$  not discussed so far is, beside the use of tunneling systems that exhibits higher  $\Delta U_{Max}$ , the use of a design as shown in Fig. 4.6, where the tunneling currents  $I_0$  are always flowing in one direction through the SDT elements forming a spin–logic gate and hence avoiding effects due to the asymmetry of the tunneling barrier as in the design chosen for the first spin–logic gate. This is shown in the next paragraph.

### 5.3 The feasibility of spin–logic gates realized with micron sized SDT elements

The tunneling system used is: Ta5/Cu30/TaN5/Ta9/NiFe3/IrMn7/CoFe2/Ru0.8/CoFe3/Al1.2 ox./NiFe6/Ta5. The CoFe2/Ru0.8/CoFe3 AFi is exchange biased to the antiferromagnet IrMn. The reference layer is not switchable on chip but guarantees magnetic switching stability at the expense of the number of programmable logic functions per spin–logic gate (in the magnetic part). At zero magnetic field the magnetizations of the AFi point in directions as defined during the anneal step [63]. The  $TMR$  is 30 % at 10 mV for SDT elements with sub- $\mu\text{m}$  width, the maximum voltage step  $\Delta U_{Max}$  is achieved at 600 mV ( $TMR$ : 15 %).

The fabrication was done by a seven–mask lithography process as already described. In contrast to the architecture of the first spin–logic device, effects due to the asymmetry of the tunneling barrier are excluded by the design.

Figure 5.3 (a) shows the architecture of the three input spin–logic gate consisting of six SDT elements. Figure 5.3 (b) shows the dc characteristic of a three input field programmable spin–logic gate realized by six nominally identical elliptically shaped SDT elements with dimensions  $2.4 \mu\text{m} \times 0.6 \mu\text{m}$ . The device is operated at tunneling currents  $I_0 = 5 \mu\text{A}$  with a corresponding voltage  $U$  of about 300 mV across each SDT element. Figure 5.3 (b) shows essentially the hysteretic switching behaviour of each SDT element while the others are in their remanent minimal resistance state. The well matching  $TMR$  and remanent resistance values of the SDT elements forming the logic gate of figure 5.3 (b) result in a gap  $G$  of 50 mV which is hence available for a sense amplifier circuit to separate two output voltage regimes corresponding to Boolean output 0 and Boolean output 1.

Nevertheless, statistical fluctuations in  $R$  and  $TMR$  values of the nominal identical SDT elements forming the spin–logic gate result in an offset  $U_0$ : 4 mV when all SDT elements are in their minimal resistance state and 10 mV when all SDT elements are in their maximal resistance state.

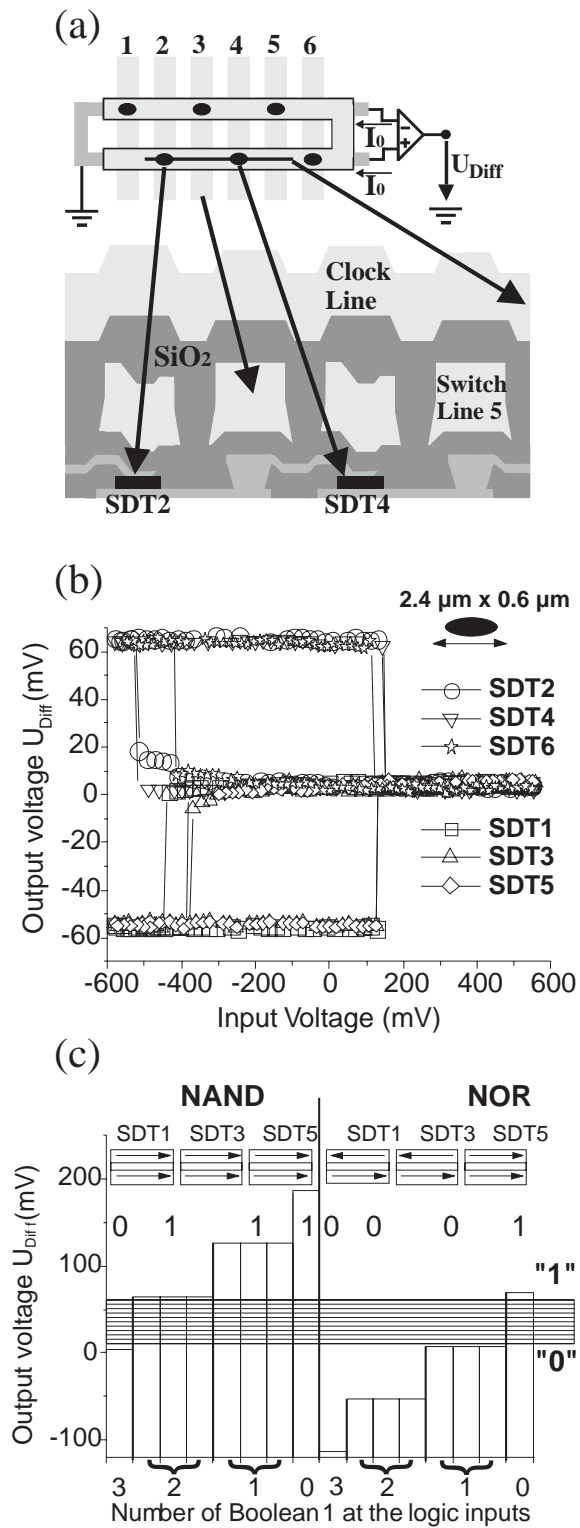


Figure 5.3: (a) design of a three input spin-logic gate and schematic cross section through the device along the black line in the top. (b) Dc characterization of a three input spin-logic gate. Numbers of the SDT elements and polarity of the voltage  $U_{Diff}$  (not amplified) are assigned in (a). (c) Programming example. SDT elements 1, 3 and 5 are chosen as programming bits, SDT elements 2, 4 and 6 serve as logic input bits. Defined Boolean values: (input 0; input 1) = (-600 mV; +600 mV), (output 0; output 1) = ( $U_{Diff} < 10$  mV;  $U_{Diff} > 60$  mV).

From the measurement in figure 5.3 (b) one can extract the voltages that corresponds to the permutations of resistance states of the SDT elements that form the spin–logic gate. Based on these voltage states, figure 5.3 (c) shows a programming example for the magnetic part of a spin–logic gate. SDT elements 1, 3 and 5 are chosen as reference bits, while the SDT elements 2, 4 and 6 serve as logic input bits. The voltages defining the input Boolean 0 and input Boolean 1 have been chosen such that the corresponding magnetic fields are sufficient to switch the soft magnetic layer of any selected SDT element. In this example, the spin–logic gate is programmed from the NAND to the NOR function by switching the soft magnetic layers of SDT elements 1 and 3.

Of course the definitions of logic and programming are arbitrary here, from the measurement of figure 5.3 (b) one can also conclude an AND/OR programming example or more complex functions by taking the fact into account that a spin–logic gate is a hybrid with more degrees of freedom due to the semiconductor circuitry.

Figure 5.4 demonstrates a three input field programmable spin–logic gate programmed as an AND gate with its output connected to a commercial sense amplifier circuitry (with opposite polarity as in Fig. 5.3) (a) in clocked operation. The SDT elements of this device are elliptically shaped ( $2.4 \mu\text{m} \times 0.6 \mu\text{m}$ ), whereas the gap  $G$  is here nominally centered around zero voltage.

As the clock signal a bias magnetic field expressed as a voltage leading to a current in the clock line and hence to a magnetic bias field is chosen identical for all SDT elements. For the  $2.4 \mu\text{m} \times 0.6 \mu\text{m}$  elliptic shaped soft magnetic layers the dependence of the coercivity on the bias magnetic field follows the so–called astroid. For the spin–logic hybrid device of figure 5.4 this characteristic is utilized for the clocked principle: the magnetic fields defining the logic input voltages corresponding to Boolean 1 and Boolean 0, and the magnetic bias field defining the amplitude of the clock signal has been chosen in a way, that the soft magnetic layer switches only when both magnetic fields are present at the location of the selected SDT element. There are other possibilities for the concept of the clock in spin–logic, the concept presented here represents not a flank principle, but a state principle.

In figure 5.4, the clock and hence the magnetic bias field is operated at 200 Hz, while the logic input, applied to SDT element 6, is alternating between Boolean 0 and Boolean 1 at a frequency of 100 Hz. The other bits of the spin–logic gate are in their remanent minimum resistance state, which corresponds here to Boolean 1 for the input bits. Output I shows the logic output of the hybrid device. The amplitude is less meaningful. More important is, that the sense amplifier acts as a current source available for inputs of subsequent spin–logic gates. Note, that the output signal I does not change upon switching of the clock, only.

Output II shows the output signal without amplifier. There is a further reduction



of the gap  $G$  when operating a spin–logic gate in clocked operation. This is due to a slight rotation of the soft magnetic layers accompanied by a shift of the tunneling resistances when the bias magnetic field is present.

The measurements presented here have not been optimized for speed. Even though the time needed to switch a magnetic layer sets the upper physical barrier for the speed, the overall circuit speed will be dictated by interface circuitry [25].

In conclusion, the feasibility of a hybrid field programmable spin–logic gate based on SDT elements in steady state and clocked operation has been shown. The programming information and the logic inputs and output are nonvolatile.

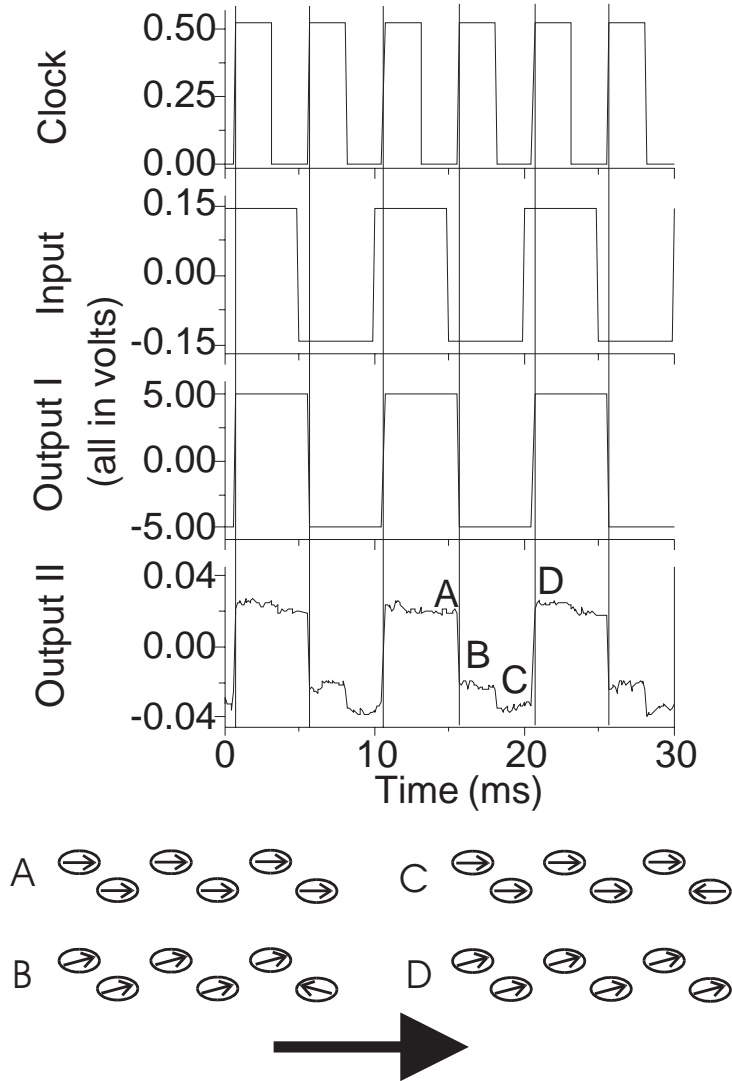


Figure 5.4: Clocked operation of a hybrid spin–logic gate, programmed as an AND gate. The input signal is applied to one bit, while the other input bits remain in their minimum resistance state corresponding to the Boolean 1. Input Boolean (0;1) = (−0.15 V; +0.15 V), output Boolean (0;1): (−5 V; +5 V). Output II shows the output signal  $U_{Diff}$ . The bottom part shows the orientation of the soft layer’s magnetization in the spin–logic gate for the corresponding cases of Output II. The big arrow points in the direction of the hard subsystem’s net magnetization.

## 5.4 Judgement on tunneling systems with respect to working spin–logic gates

So far, the criteria for working spin–logic gates have been named and two working spin–logic gates have been presented. The matching requirements of  $TMR$  and  $R$  are fulfilled for these spin–logic gates. Regarding the yield of working spin–logic gates across a wafer, the fluctuations of  $TMR$  and  $R$  within the SDT elements that form spin–logic gates have to be taken into account. Sources for mismatch of these properties are obviously due to the fabrication process or due to the tunneling system.

The geometry of the SDT elements that form a spin–logic gate are defined identically on the mask, but their electrical properties might fluctuate due to inhomogeneities in the fabrication process, which are namely (without seeking of completeness):

Granularity of the resist which leads to a roughness of the SDT element pattern within the MML accompanied by fluctuations in the SDT's area and hence in the measured tunneling resistance. An inhomogeneous development of the resist does have the same consequence.

Shortcuts between the bottom and top electrode along the SDT elements, produced by the deposition of a mixture of MML material and resist during the IBE transfer of the SDT element in the MML lead either to a decrease of both the mean of  $TMR$  and the mean of  $R$  or even to a shortcut between top and bottom electrode. The weak presence of this effect leads also to fluctuations of  $TMR$  and  $R$ .

The tunneling system is the other source of fluctuation. For measuring identical  $TMR$  and  $R$ , the magnetization states that correspond to maximal and minimal tunneling resistances of both the reference layer system and the soft magnetic layers needs to be identical and reproducible for the SDT elements. For sub- $\mu\text{m}$  SDT elements with statistically distributed edge roughness (ratio of circumference to area increases for smaller area) such identical and reproducible magnetization states cannot be taken granted because roughness induces magnetic stray fields with impact on the magnetization state. The not reproducible switching behaviour of the soft magnetic layer for nominal identical SDT elements as shown in Fig. 6.4, for instance, indicates these not reproducible magnetization states. Furthermore, the choice of the reference layer system does have an impact on the degree of irreproducibility of magnetization states and hence on the fluctuations of  $TMR$  and  $R$  across a wafer. The choice of the programmable reference layer system Ru/CoFe leads to not reproducible magnetization states of the soft magnetic layer (Fig. 6.4) and of the CoFe layer. The higher intrinsic magnetic stability of an exchange biased system leads directly to a better reproducibility of the magnetization states, as can be concluded from Fig. 6.4.

The tunneling barrier is the next possible source for mismatching properties of the SDT elements that form spin-logic gates. The tunneling barrier must be structurally as well as electrically homogeneous for matching  $TMR$  and  $R$  values of nominal identical SDT elements. For thicknesses of tunneling barriers below 2 nm, a variation of 0.1 nm in the barrier thickness, correlated to the grain size of the underlying metallic layers, for instance, leads to an increase in tunneling current in the order of at least one decade. Thus the tunneling resistance is extremely sensitive to the homogeneity of the tunneling barrier thickness. A source for thickness variation of  $\text{Al}_2\text{O}_3$ , for instance, is the thickness variation of sputtered aluminum, which is oxidized in a subsequent step. The resulting over- and underoxidization leads to further inhomogeneities in the electrical properties of the tunneling barrier. Moreover, interface and bulk traps, contaminants, crystal defects and surface roughness can reduce the effective thickness of the tunneling barrier and lead to further conducting centers (hot spots) through the oxide [83]. A further source of barrier inhomogeneity are trapped states within the tunneling barrier. These electronic states within the barrier, formed by a rest of metallic aluminum, for instance, lead to an enhanced local tunneling probability and act as spin flip centers which leads to a decreased  $TMR$  signal.

The impact of the inhomogeneities within the tunneling barrier on the matching properties of  $TMR$  and  $R$  of nominal identical SDT elements depends on the ratio of SDT element dimensions and the mean separation of the inhomogeneities within the barrier. For dimensions of the SDT elements in the regime of the mean distance of the inhomogeneities (the different classes of inhomogeneities do have different mean distances), the mismatch in  $R$  and  $TMR$  does have its maximum. A tool to map local conduction centers in the tunneling barrier is the conducting atomic force microscope (C-AFM) [84]. C-AFM measurements on typical tunneling barriers (magnetic reference electrode plus  $\text{Al}_2\text{O}_3$ ) showed these hot spots with a mean separation below 100 nm [85] [86]. Furthermore, most of the tunneling current is mediated by the hot spots. From the typical separation below 100 nm one can expect an increasing mismatch of  $R$  and  $TMR$  (fluctuations in  $TMR$  are connected to these in  $R$  by the spin flip centers) with decreasing dimensions of the SDT elements down to the sub-100 nm regime.

In order to make a judgement on a tunneling system with respect to the yield of working spin-logic gates, the following experiment was performed.

$R$  (corresponds to the minimal resistance) and  $TMR$  of 20, nominal identical SDT elements of circular shape were measured. The SDT elements are arranged as shown in the top of Fig. 5.5 and are separated from each other by 40  $\mu\text{m}$ . From these measurements, the mean  $\mu$  and the standard deviation  $\sigma$  are determined.

Within closed neighborhood, there are arrays with different tunneling area of 20,

nominal identical circular shaped SDT elements. Hence  $\mu_R$ ,  $\mu_{TMR}$ ,  $\sigma_R$  and  $\sigma_{TMR}$  can be measured as a function of tunneling area.

The mask set was defined such that the measurement could be performed on many locations of the 3 inch structured wafer. The resulting  $\mu$  and  $\sigma$  are a consequence of all inhomogeneities discussed earlier and no trial is performed here to name the sources of the fluctuations in the measured data. Nevertheless two rules of thumb are concluded from all measurements performed. Firstly the fluctuations reach a minimum in the regime where the tunneling barrier is optimized with respect to the highest  $TMR$  signal. Secondly, the real area of the tunneling elements differs by their nominal area, the exact difference depends on the individual fabrication charge.

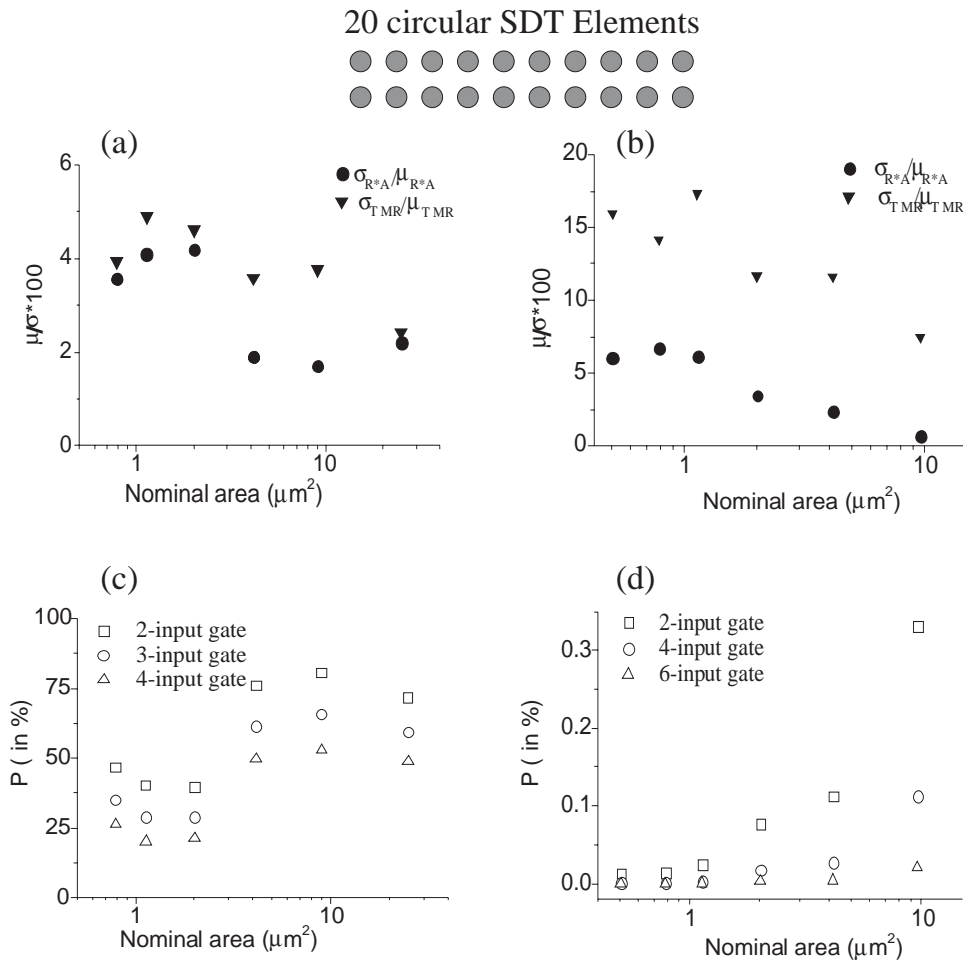


Figure 5.5: Top: Arrangement of the nominal identical circular SDT elements within an array. (a) Relative standard deviations as a function of the nominal area of the circular shaped SDT elements (Ta5/Cu30/TaN5/Ta9/NiFe3/IrMn7/CoFe2/Ru0.8/CoFe3/Al1.2 ox./NiFe6/Ta5). The results are based on 20 measurements per area. (b) Result as in (a) for Ru30/CoFe1.5/Al1.2/CoFe1/NiFe5/Ta5. The results are based on 80 measurements per area. (c) Result of a Monte-Carlo simulation on the probability  $P$  of working spin-logic gates based on (a). A gaussian distribution of  $R$  and  $TMR$  is assumed. (d) Result as in (c) based on the measurement in (b).

Figure 5.5 (a) and (b) shows the results for two tunneling systems, namely Ta5/Cu30/TaN5/Ta9/NiFe3/IrMn7/CoFe2/Ru0.8/CoFe3/Al1.2 ox./NiFe6/Ta5 (a) and Ru30/CoFe1.5/Al1.2/CoFe1/NiFe5/Ta5 (b). The fluctuations in (a) are smaller than in (b) (especially  $TMR$ ) which can be explained by two reasons. The tunneling barrier in (a) is better optimized than in (b) which manifests itself in a higher breakdown voltage for system (a) (2.2 V) than in (b) (1.5 V). Secondly, the intrinsic magnetic stability of the reference layer system in (a) is higher than in (b). The magnetic configuration of the programmable reference layer CoFe ( $H_c \approx 25 \text{ kAm}^{-1}$ ) is easier to disturb by magnetic fields (e. g. demagnetizing fields in small elements) than the magnetic configuration of the exchange biased AFi. Hence the deviation from the homogeneous magnetization of the reference layer system in small SDT elements is in (b) bigger than in (a). This mechanism leads mainly to an increase of the fluctuations of the  $TMR$  with smaller area (bigger demagnetizing fields) as measured in (b). Furthermore the increase of the relative standard deviation  $\frac{\sigma}{\mu}$  of  $R$  and  $TMR$  is in (b) bigger than the corresponding errors of the relative standard deviations, hence from the measurement one can conclude a systematic increase of the fluctuations with smaller tunneling area. Contrary, this cannot be concluded from (a), since the errors of  $\frac{\sigma}{\mu}$  are in the order of the changes of  $\frac{\sigma}{\mu}$  itself (the error of  $\frac{\sigma}{\mu}$  is bigger due to a smaller basis of measurement from which  $\frac{\sigma}{\mu}$  is concluded).

Figure 5.5 (c) and (d) shows the probability  $P$  of working spin–logic gates on a wafer that exhibits a gaussian distribution of  $R$  and  $TMR$  with standard deviations and means from (a) ( $\mu_{TMR} = 15 \%$  at 650 mV) and (b) ( $\mu_{TMR} = 10 \%$  at 450 mV). Details on the Monte–Carlo simulation are given in the next section.

The measured data was tested on a gaussian distribution by a probability paper test [87]. In spite of the small number of data points, it turned out that the assumption of a gaussian distribution is reliable.

### 5.4.1 Monte–Carlo simulation

Monte–Carlo (MC) simulation is a technique for numerically solving mathematical problems via statistics. The goal of the MC simulation is the determination of the probability  $P$  that a spin–logic gate works, when  $TMR$  and  $R$  of nominal identical SDT elements that form spin–logic gates do fluctuate according to a gaussian distribution described by  $\sigma$  and  $\mu$ . The architecture of the MC program is as follows: The program generates randomly SDT elements characterized by  $R$  and  $TMR$ .  $R$  and  $TMR$  are calculated from a gaussian distribution characterized by  $\mu_R$ ,  $\mu_{TMR}$ ,  $\sigma_R$ ,  $\sigma_{TMR}$  and voltage of operation. Next, different SDT elements are used to form spin–logic gates (n input gate consists of 2n SDT elements). For these randomly generated gates all voltage states as shown exemplarily for a two input spin–logic

gate in Fig. 5.1 are calculated. Obviously, these voltage states are not degenerated. Within this scheme, a big number ( $\sim 10000$ ) of spin-logic gates is calculated.

The criterion for a working spin-logic gate is chosen from an economic point of view. The gap  $G$  (30 mV) is defined globally for all spin-logic gates on the wafer, meaning that the amplifier circuitry uses that gap to separate the logic outputs 0 and 1 regimes for all spin-logic gates. A working spin-logic gate does not have a voltage state inside the gap. With this criterion the number of working spin-logic gates is calculated. From the total amount of spin-logic gates calculated, the probability  $P$  is determined.

The results of Fig. 5.5 were calculated by the MC simulation for measured values. Figure 5.6 shows a systematic study of the influence of the important parameters which determine  $P$ .

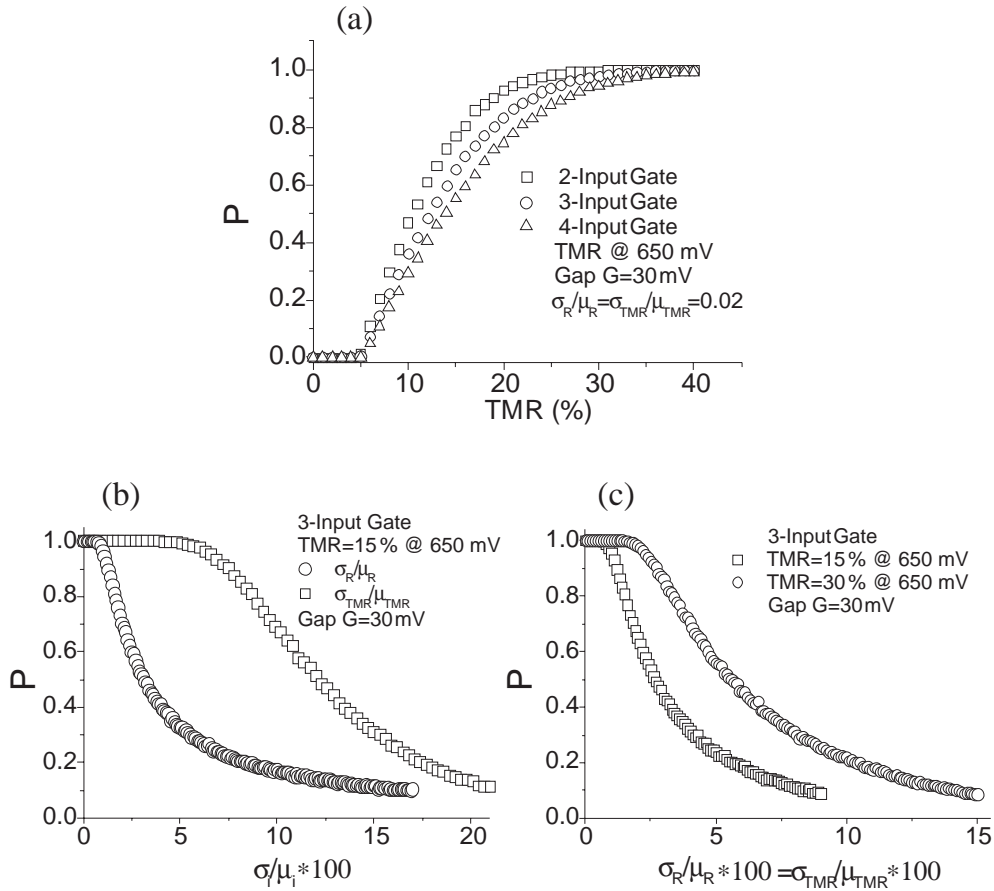


Figure 5.6: Results of the MC simulation on the global behaviour of the probability  $P$  of working spin-logic gates. (a) dependence of  $P$  with respect to the number of logic inputs and the mean  $TMR$  signal at constant fluctuations in  $R$  and  $TMR$ . (b) Statistical fluctuations in  $R$  are more critical than statistical fluctuations in  $TMR$  for  $P$  (The not fluctuated parameter is kept at zero). This conclusion is right for state-of-the-art tunneling systems with  $TMR$  values below 100% (c) High statistical fluctuations in  $R$  and  $TMR$  can be compensated by an increase of the  $TMR$  signal.  $\square$  represents the tunneling system of Fig. 5.5 (a).  $\circ$  represents the best (for spin-logic) state-of-the-art tunneling system.

As already mentioned,  $P = f(\mu_R, \mu_{TMR}, \sigma_R, \sigma_{TMR}, \text{operation voltage, size of gap } G, \text{ number of inputs})$ .

Tendencies which higher  $P$  are an increase of  $\Delta U_{Max}$  ( $TMR \cdot$  operation voltage) and a decrease of the statistical fluctuations in  $TMR$  and  $R$ . The statistical fluctuations are not reducible to any amount, even for smaller tunneling areas. Hence a maximization of  $\Delta U_{Max}$  is important, e. g. by using SDT elements with double [88] barriers. A decrease of the Gap  $G$  is also desirable and should not be accompanied by too much efforts to the amplifier circuitry.

Since it is favorable to maximize the number of inputs of spin–logic gates and  $P$  decreases with higher number of inputs, it is favorable to decrease the fluctuations and increase  $\Delta U_{Max}$  anyway.

The next sections deal with investigations of physical aspects of single SDT elements with impact on the performance of spin–logic gates, namely the switching behaviour of the soft magnetic layer, the programmable reference layer system Ru/CoFe and the magnetic stability of magnetic reference layer systems.





# Chapter 6

## Aspects of the switching behaviour

### 6.1 Shape anisotropy

#### 6.1.1 Theoretical aspects

For the application of SDT elements in logic gates, the magnetic layers must exhibit a single domain like switching behaviour. One approach to achieve this is the use a soft magnetic material where a strong intrinsic uniaxial anisotropy, expressed as a dominating  $E_{Anisotropy}$  in equation 2.12, defines an easy axis for the magnetization. For the in-plane magnetization aligned along the easy axis, the anisotropy energy  $E_{Anisotropy}$  is then minimal.

The approach investigated here is to define an easy axis for the magnetization by the shape anisotropy. This anisotropy originates from the fact, that the stray field energy  $E_{StrayField}$  depends on the direction of the magnetization for a single domain magnetic particle with an asymmetric shape. The stray field  $H_D$  ( $E_{StrayField} = \frac{1}{2} \cdot \mu_0 \cdot \int_{allspace} H_D^2 dV$ ) that results from the magnetization of a magnetic body can be calculated from the scalar magnetic potential  $\varphi_m(\vec{r})$ , which is derived directly from a Maxwell equation for the conditions  $\vec{j}(\vec{r}) = 0$  and  $\vec{M}(\vec{r}) \neq 0$  [89]:

$$\vec{\nabla} \cdot \vec{B}(\vec{r}) = \mu_0 \vec{\nabla} \cdot (\vec{H}(\vec{r}) + \vec{M}(\vec{r})) = 0$$

$$\vec{H}_D(\vec{r}) = -\vec{\nabla} \cdot \varphi_m(\vec{r}) \quad \text{with} \quad \Delta \varphi_m(\vec{r}) = \vec{\nabla} \cdot \vec{M}(\vec{r}) \quad (6.1)$$

The classical example of the uniformly magnetized general ellipsoid with axes a, b, c results in a constant interior stray field  $H_{D,i}$  that is given by [12] [90]:

$$\vec{H}_{D,i} = -\mathbf{N} \cdot \vec{M} \quad (6.2)$$

The magnetic stray field in the magnetic body is orientated antiparallel to the magnetization which causes the stray field.  $\mathbf{N}$  is the symmetrical demagnetizing tensor with the demagnetizing factors  $N_a$ ,  $N_b$ ,  $N_c$  along the corresponding axes

fulfilling  $N_a + N_b + N_c = 1$ . As experimentally verified later in this section, the shape anisotropy of a soft magnetic layer of an elliptically shaped SDT element can be well approximated by the shape anisotropy of an ellipsoid with length  $a$ , width  $b$  and thickness  $c$  ( $a > b \gg c$ ). For an in-plane magnetized single domain particle, the dependence of the stray field energy  $E_{StrayField}$  on the magnetization's angle of rotation  $\varphi$  from the long axis (Minimum of  $E_{StrayField}$ ) corresponds to that of a second order uniaxial anisotropy:

$$E_{StrayField} = \frac{1}{2} \cdot \mu_0 \cdot M_s^2 \cdot V_{Sample} \cdot N_a + \frac{1}{2} \cdot \mu_0 \cdot M_s^2 \cdot V_{Sample} \cdot (N_b - N_a) \cdot \sin^2 \varphi \quad (6.3)$$

Thus the corresponding anisotropy field  $H_k$  is given by:

$$H_k = M_s \cdot (N_b - N_a) \quad (6.4)$$

Figure 6.1 shows numeric calculations of the anisotropy field  $H_k$  of the general ellipsoid for the saturation magnetization  $M_s=800 \text{ kAm}^{-1}$  (NiFe).

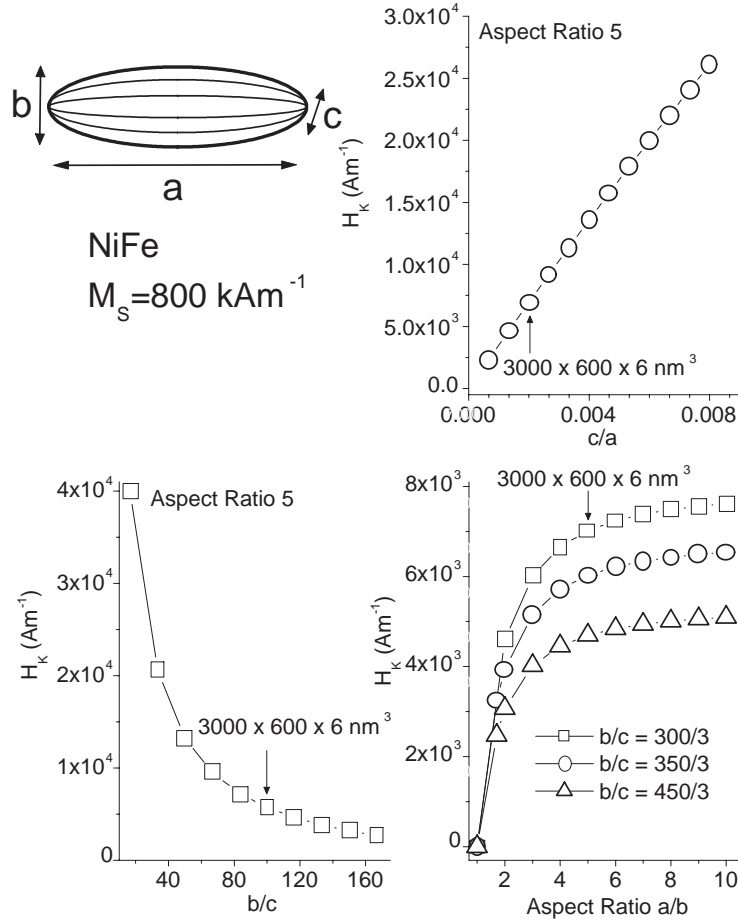


Figure 6.1: Dependencies of the shape anisotropy field  $H_k$  on the ratios of the axes  $a$  (length),  $b$  (width) and  $c$  (thickness) of the general ellipsoid for NiFe ( $M_s=800 \text{ kAm}^{-1}$ ). The ratios shown are typical for the soft magnetic layer of SDT elements at sub- $\mu\text{m}$  widths.

The calculations are based on the demagnetizing factors of the general ellipsoid as given in Ref. [91].

According to Fig. 6.1, the shape anisotropy is adjustable by the ratios of the axes of the ellipsoid,  $a$ ,  $b$  and  $c$ . At constant thickness  $c$ , which is typically below 10 nm for the soft magnetic layer in SDT elements, the shape anisotropy increases with smaller width  $b$  and larger aspect ratio  $a/b$ . At constant ratio  $b/c$ , the shape anisotropy reaches a saturation value with increasing aspect ratio.

The intrinsic uniaxial anisotropy of a 6 nm thick, rf-magnetron sputtered NiFe film (Ru5/Cu30/Al1.5 ox./NiFe6/Ta5) was measured by MOKE and varied between 0.4 kAm<sup>-1</sup> and 0.6 kAm<sup>-1</sup> across a 3 inch wafer. Hence for SDT elements with a high aspect ratio and a width  $b$  in the regime of about 1 μm and below (Fig. 6.1), the shape anisotropy is expected to determine the switching behaviour of a NiFe layer with  $c=6$  nm.

In contrast to the general ellipsoid discussed so far, the magnetic layers of a typical SDT element are oblate. Two geometries of a magnetic layer were investigated, the disc-shaped (oblate) ellipsoid and the rectangle. For a homogeneous magnetization, the magnetostatic potentials  $\varphi_m(\vec{r})$  were calculated. The resulting magnetic stray field of the oblate ellipsoid magnetized parallel to its length  $a$  is given by:

$$\vec{H}_D(\vec{r}) = \frac{M_s}{4\pi} \int_0^{2\pi} \int_{-\frac{c}{2}}^{\frac{c}{2}} \cos \varphi' \cdot \sqrt{a^2 \cdot \cos^2 \varphi' + b^2 \cdot \sin^2 \varphi'} \cdot \left( \frac{\vec{r} - \vec{r}_{ab}}{|\vec{r} - \vec{r}_{ab}|^3} \right) d\varphi' dz',$$

$$\text{with } \vec{r}_{ab} = (a \cdot \cos \varphi', b \cdot \sin \varphi', z') \quad (6.5)$$

$H_D$  of the oblate rectangular magnetized along its length  $a$ :

$$\vec{H}_D(\vec{r}) = \frac{M_s}{4\pi} \int_{-\frac{b}{2}}^{+\frac{b}{2}} \int_{-\frac{c}{2}}^{+\frac{c}{2}} \left( \frac{\vec{r} - \vec{r}_{+a}}{|\vec{r} - \vec{r}_{+a}|^3} - \frac{\vec{r} - \vec{r}_{-a}}{|\vec{r} - \vec{r}_{-a}|^3} \right) dy' dz', \quad \text{with } \vec{r}_{\pm a} = \left( \pm \frac{a}{2}, y', z' \right) \quad (6.6)$$

The origin of the coordinate system coincides with the center of the magnetic bodies. The  $x$ -,  $y$ -,  $z$ -axes point in the direction of the length  $a$ , width  $b$  and thickness  $c$ , respectively.

The magnetic stray fields from equations 6.5 and 6.6 were calculated numerically with Mathematica<sup>®</sup>. The amplitude of the magnetic stray field  $|\vec{H}_{D,x} + \vec{H}_{D,y}|$  in the  $x - y$ -plane through the center ( $z=0$ ) of a 1800 nm × 900 nm × 6 nm ellipse and a 1800 nm × 900 nm × 6 nm rectangular, respectively, are shown in Fig. 6.2.

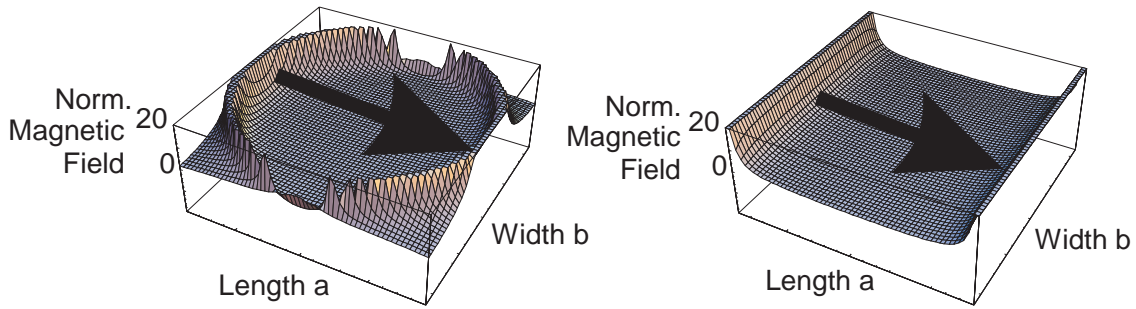


Figure 6.2: 3-D plots of the amplitude of the stray field  $H_D = |\vec{H}_{D,x} + \vec{H}_{D,y}|$  of 6 nm thick, flat magnetic layers homogeneously magnetized in the direction of the respective arrow. The left magnetic film is elliptic (1800 nm  $\times$  900 nm), the right one is rectangular (1800 nm  $\times$  900 nm). The amplitude of  $H_D$  is normalized to its value in the center of the respective element. Relative amplitudes larger than 20 near the boundaries of the elements are suppressed.

In contrast to the general ellipsoid, the magnetic stray field inside the magnetic bodies is not constant and a magnetization along the length  $a$  causes also a magnetic stray field component along the  $y$ -axis. The strong magnetic stray fields near the boundaries of the elements favor magnetic domains there energetically in real systems ( $\vec{M}$  is antiparallel orientated to the stray field component along the long axis). If magnetic domains are present, a general prediction of the impact of the shape anisotropy on the switching behaviour cannot be concluded. If, however, the magnetization does not split up into domains, the shape anisotropy is given by the mean of  $H_k$  over the volume of the element. This mean value of  $H_k$  is often well approximated by that of the inscribed ellipsoid [91].

### 6.1.2 Impact of the shape on the minor loops

Figure 6.3 shows the impact of the shape and the aspect ratio at width  $b = 900$  nm on the switching behaviour of a 6 nm thick NiFe layer. The shapes investigated here are the rectangle, ellipse and eye. The real patterns exhibit, in contrast to the shapes used for simulation, rounded curves due to the pattern transfer in lithography. The switching behaviour of the NiFe layers is measured via the  $TMR$ , the stack of the SDT elements was: Ta5/Cu30/TaN5/Ta9/NiFe3/IrMn7/CoFe2/Ru0.8/CoFe3/Al1.2ox./NiFe6/Ta5. The fluctuations in the  $TMR$  signals are due to a second tunneling barrier between the top electrode and the NiFe layer, probably formed by a Ta<sub>2</sub>O<sub>5</sub> layer or a remaining resist film on top of the Ta. This tunneling barrier was selectively destroyed by applying a high voltage across both tunneling barriers. The variation of the  $TMR$  signals in Fig. 6.3 reflects an only partial destruction of the additional tunneling barrier for some SDT elements.

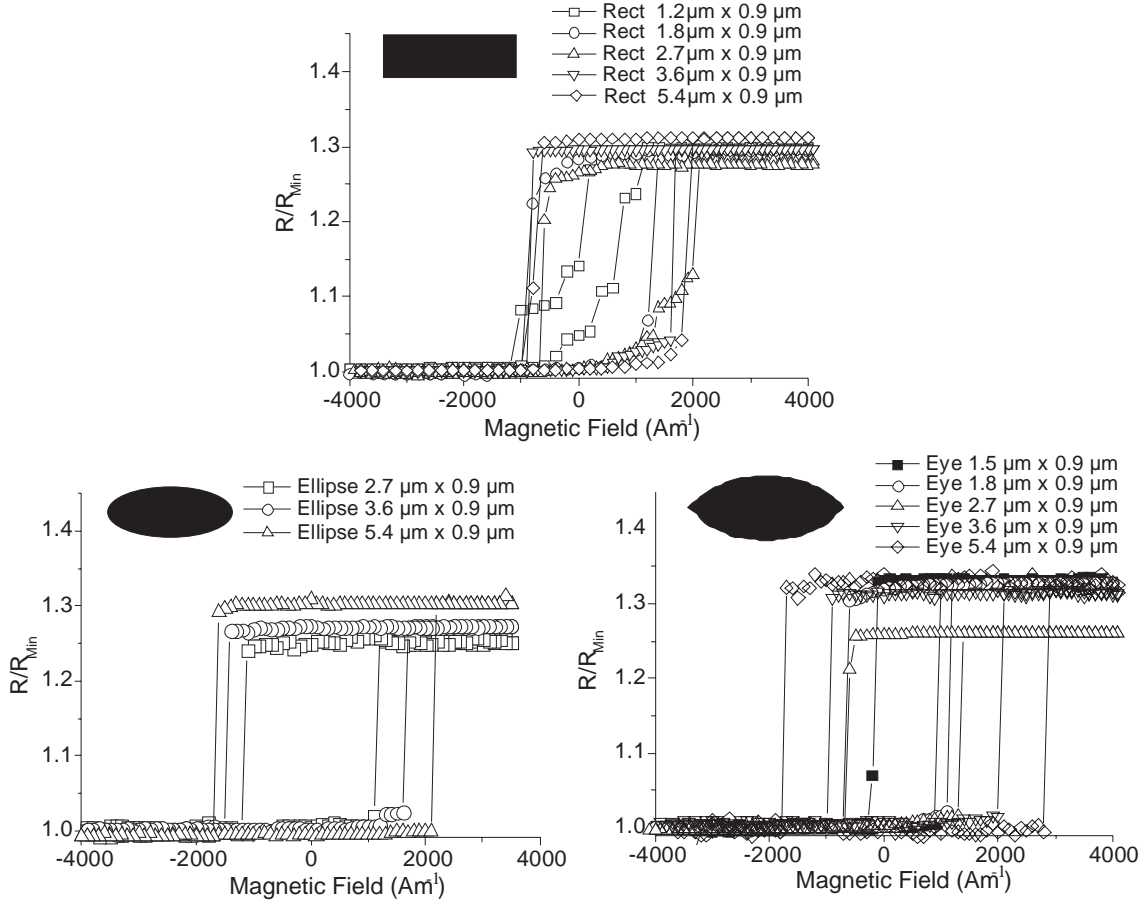


Figure 6.3: Minor loops of SDT elements of width  $0.9 \mu\text{m}$  with an exchange biased AFi and a soft magnetic NiFe layer (...IrMn7/CoFe2/Ru0.8/CoFe3/Al1.2 ox./NiFe6/Ta5). The higher the aspect ratio is the more single domain like is the switching behaviour along the long axis of the soft magnetic layer. Rectangles exhibit the abrupt switching only at the big aspect ratios, whereas elliptically and eye shaped SDT elements start with this behaviour at lower aspect ratios.

Rectangular shaped SDT elements exhibit intermediate resistance states between the extremal ones, hence multiple domain configurations are energetically stable. The switching behaviour of the two highest aspect ratios is single domain like, with remanent resistance states matching the extremal resistance states.

Elliptically and eye shaped SDT elements exhibit single domain like minor loops for lower aspect ratios, nevertheless tiny deviations indicate the existence of magnetic domains.

All measured coercivities are smaller than the theoretically predicted  $H_k$ . The switching behaviour of the rectangular elements can be explained by domains at the ends, which are energetically favorable because their existence decreases the stray field at the edges as shown in Fig. 6.2 and hence the stray field energy  $E_{StrayField}$ . The existence of these domains in rectangular shaped elements has been also reported elsewhere [92] [93] [94].

For low aspect ratios, at a critical magnetic field lower than  $H_k$ , the switching of the magnetic layer starts at these edge-domains. For 20 nm and 5 nm thick NiFe, rectangular elements (down to a width of 400 nm) with a higher aspect ratio are reported to exhibit a more pronounced single domain like switching behaviour [94]. This is in accordance with the measurements in Fig. 6.3. With increasing aspect ratio, the end domains occupy a relatively smaller part of the magnetic layer, with the consequence of smaller influence on the magnetization reversal and more pronounced single domain like switching.

Another explanation reported for the reversal mechanism in a rectangular shaped, 10 nm thick magnetic layer (NiFe10/Cu5/NiFe5/NiO10) is domain wall nucleation at the ends which is the starting point of the reversal [95]. The external magnetic field required for nucleating the domain wall depends on the stray field at the end of the wire. Its general trend, calculated from equation 6.6, is a decrease of the stray field at the edges with increasing length. The higher the aspect ratio the lower the stray field  $H_D$  at the edges, hence a higher external magnetic field  $H_{Ext}$  is needed to start the domain wall nucleation. Hence this model explains also the measurements in Fig. 6.3.

A measurement of  $TMR$  versus aspect ratio, which could clear the question on the existence of the edge domains, was not possible to perform, because the  $TMR$  itself turned out not to be reproducible for nominal identical SDT elements of the sample. For the elliptically and eye shaped SDT elements, in principal the same scenarios of the switching behaviour as for the rectangles are possible. End domains in elliptically shaped, 21 nm thick NiFe layers were observed, down to a width of 100 nm and even for high aspect ratios [92]. The initialization of the switching is reported to start at higher fields compared to rectangles, which is in accordance with the measurements of Fig. 6.3. Furthermore, the initialization of the magnetization reversal by an end domain movement is observed at higher external magnetic fields with higher aspect ratio of the ellipses. In fact, that tendency is reflected by the measurements of Fig. 6.3, too.

Evaluating equation 6.5 for the ellipse leads to lower stray fields at the ends of an ellipse as for a rectangle at same dimensions  $a$ ,  $b$ ,  $c$ . The stray fields at the ends of the ellipse decrease with higher aspect ratio, too. These results explain the lower coercivities of rectangles compared to elliptic and eye shapes and the increasing coercivity of elliptic and eye shapes with increasing aspect ratio.

In contrast, micromagnetic simulations of 3 nm thick elliptically shaped magnetic layers with sub- $\mu\text{m}$  width showed the reversal initiated by domain nucleation in the center of the element and no end domains [96]. These simulations showed also a significant influence of the edge roughness on the switching fields.

### 6.1.3 Impact of the reference layer system

Figure 6.4 (a) shows exemplarily the reproducibility of the switching behaviour for elliptically and eye shaped SDT elements at widths below  $1 \mu\text{m}$ . The overall shape of the minor loop is single domain like, whereas the switching fields of different, nominal identical elements do not match exactly. Furthermore, the switching fields fluctuate with repeating the reversal cycles of one element. The switching fields of the soft magnetic layer of a SDT element are reproducible within an interval with size of  $150 \text{ Am}^{-1}$ .

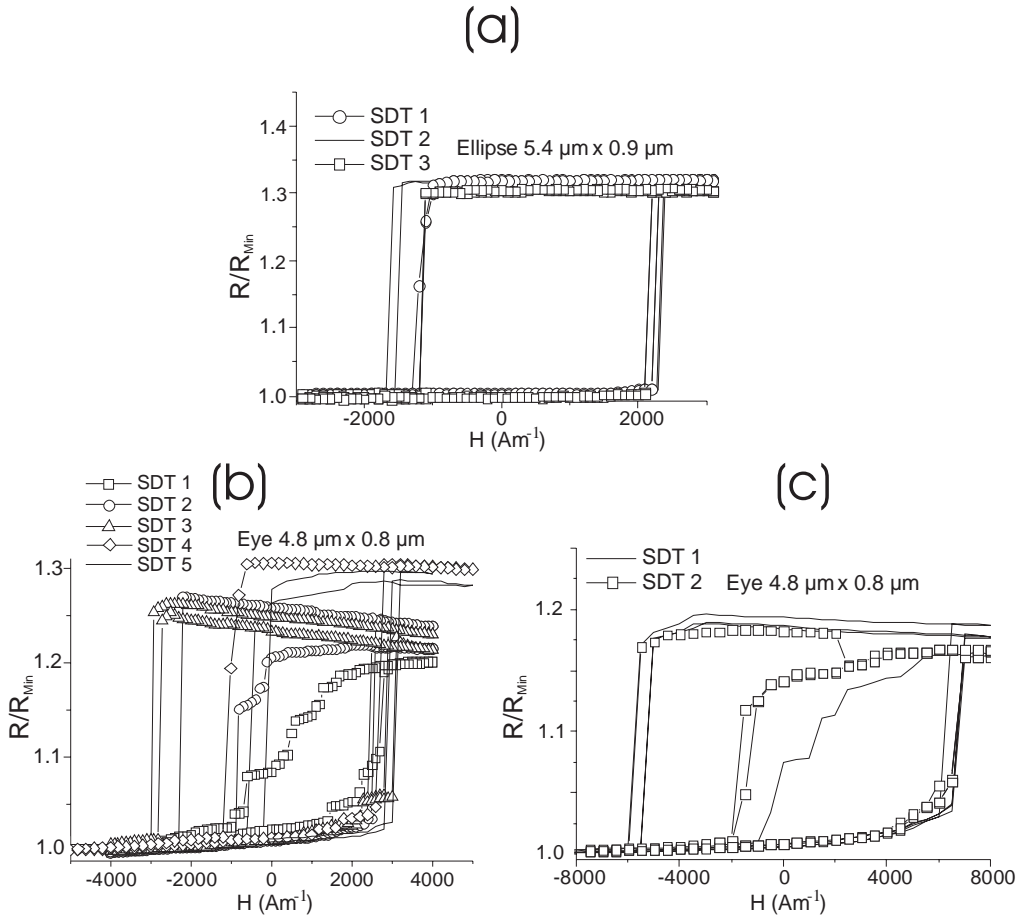


Figure 6.4: (a) Minor loops of three  $5.4 \mu\text{m} \times 0.9 \mu\text{m}$  elliptically shaped SDT elements with an exchange biased AFi as the hard magnetic system ( $\text{Ta5/Cu30/TaN5/Ta9/NiFe3/IrMn7/CoFe2/Ru0.8/CoFe3/Al1.2 ox./NiFe6/Ta5}$ ). The switching behaviour of the soft magnetic layer is significantly less reproducible for  $\text{Ru/Co}_{50}\text{Fe}_{50}$  as the reference system. (b)  $\text{Ru20/Ta5/Ru10/Co}_{50}\text{Fe}_{50}1/\text{Al1.2ox./NiFe5}$ . (c)  $\text{Ru30/Co}_{50}\text{Fe}_{50}1.5/\text{Al1.2/Co}_{50}\text{Fe}_{50}1/\text{NiFe5}$ .

A feature not yet addressed is the impact of the reference layer on the switching behaviour of the soft magnetic layer. Features discussed later in more detail (figure 6.6) are the Néel and magnetostatic coupling and the magnetic stray fields from

the edges of the reference layer acting on the edge domains in the soft magnetic layer [95]. Fig. 6.4 (b) and (c) show the switching behaviour for SDT elements with a simple Ru/CoFe hard magnetic system. The switching behaviour is significantly less reproducible as for the tunneling system in (a) with an exchange biased AFI as the reference layer. One can identify two different reversal mechanisms, a single domain like corresponding to a high  $TMR$  and another one corresponding to a lower  $TMR$ . Hence two different corresponding magnetization configurations of one or both of the CoFe and NiFe correspond to the two switching mechanisms. The reversal mechanisms will be discussed later in more detail.

Conclusively, the closest single domain like switching behaviour is achieved for the tunneling system with an exchange biased magnetic reference electrode and for elliptically or eye shaped SDT elements with aspect ratio between 2 and 6 at widths below  $1 \mu\text{m}$ .

## 6.2 Measurement of astroids

### 6.2.1 Determination procedure of an astroid

From the investigation of the two-dimensional switching behaviour of the soft magnetic layer of a SDT element one gains more information about the interlayer coupling and the domain structure of the soft magnetic layer. Recapitulating the results from Fig. 6.3, eye shaped SDT elements at sub- $\mu\text{m}$  widths, which promise to be closest to the single domain like switching behaviour, are investigated. Both the magnetic field along the long axis of the element ( $H_x$ ) and the magnetic field perpendicular to the long axis ( $H_y$ ) were generated by currents through the respective current lines running on top of the SDT element (a cross section of the arrangement on-chip is shown in Fig. 8.1). For the minor loop measurements,  $H_x$  was changed in discrete steps separated by a time of 500 ms while a constant magnetic field  $H_y$  was applied to the SDT element. According to the Stoner and Wohlfarth theory as described on page 14, the coercivity of a single domain particle is characterized by a so-called astroid in the  $H_x - H_y$  space. From a minor loop measurement  $R(H_x, H_y = \text{const.})$ , two values  $H_{c1}$  and  $H_{c2}$  are determined by the two fields corresponding to the extremal changes of the tunneling resistance:

$$H_{c1} = \text{Min} \left( \frac{\partial R}{\partial H_x} \right)_{H_y = \text{const.}, H_x: - \rightarrow +} \quad H_{c2} = \text{Min} \left( \frac{\partial R}{\partial H_x} \right)_{H_y = \text{const.}, H_x: + \rightarrow -} \quad (6.7)$$

Equations 6.7 are valid for a set of minor loops with its minimal tunneling resistance at positive  $H_x$  as is in Fig. 6.5.



## 6.2.2 Deviations of the measured astroids from the Stoner and Wohlfarth theory

The astroid shown in Fig. 6.5 is extracted from the measurement of three minor loops per  $H_y$ . Its overall shape is reproducible within the typical interval size of minor loop measurement ( $150 \text{ Am}^{-1}$ ). The  $H_x$  axis coincides with the easy axis of the uniaxial shape anisotropy. The end points of the minor loops were chosen to be in a regime  $H_x = [-10 \text{ kAm}^{-1}; 15 \text{ kAm}^{-1}]$ . The subsequently measured switching fields turned out to be independent of the exact end point values in this regime. There are deviations to the theoretical astroid as predicted by Stoner and Wohlfarth. Most of these deviations origin simply from the fact that the soft magnetic layer characterized in Fig. 6.5 is not a single domain particle. Obviously, the steps in the minor loops in Fig. 6.5 (a) and (b) reflect domain configurations of the soft magnetic layer at  $H_y \neq 0$  which are not present at  $H_y = 0$ . Moreover,  $\frac{H_c}{H_k} \approx 0.5$ , as determined from the fit to the astroid in Fig. 6.5. Hence the magnetization reversal of the soft magnetic layer is not due to a coherent rotation which would result in a  $\frac{H_c}{H_k}$  close to 1.

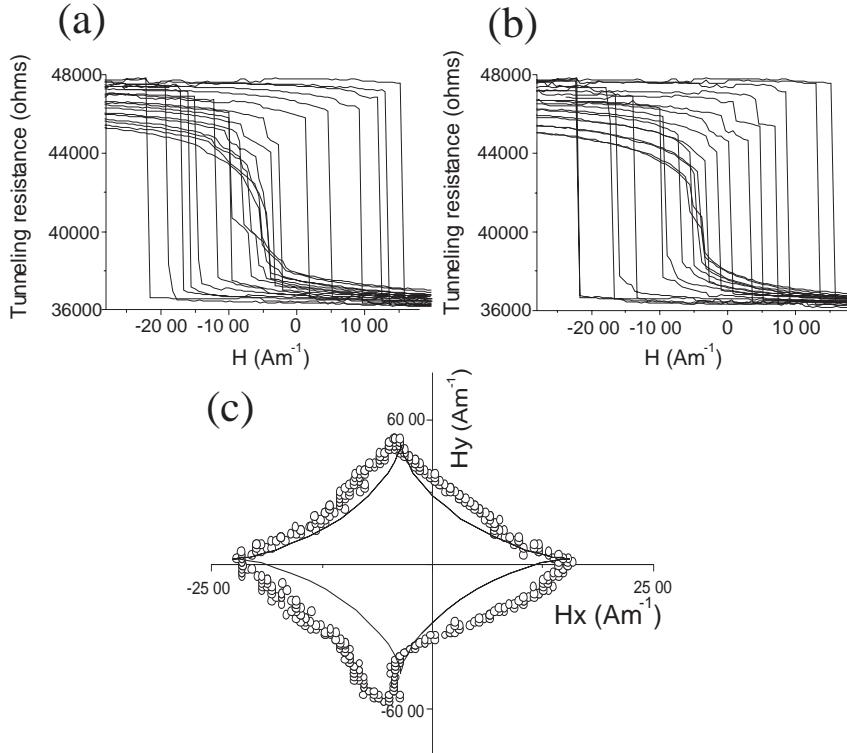


Figure 6.5: Typical astroid measurement on an eye shaped SDT element fabricated from the stack: Ta5/Cu30/TaN5/Ta9/NiFe3/IrMn7/CoFe2/Ru0.8/CoFe3/Al1.2 ox./NiFe6/Ta5 ( $4.2 \mu\text{m} \times 0.7 \mu\text{m}$ ). (a) Minor Loops at constant  $H_y$  values, ranging from  $H_y = -5850 \text{ Am}^{-1}$  to  $H_y = 0$  in steps of  $585 \text{ Am}^{-1}$ . (b)  $H_y = 0 \text{ Am}^{-1}$  to  $H_y = +5850 \text{ Am}^{-1}$ , also in steps of  $585 \text{ Am}^{-1}$ . (c)  $\circ$ : Astroid extracted from measurements as shown in (a) and (b) by use of equation 6.7. The line is a fit to theory.

The mismatch of the center of the astroid to the origin of the  $H_x - H_y$  coordinate system can be explained by magnetostatic interactions of the soft magnetic NiFe layer with the CoFe/Ru/CoFe AFi [97].

The net interaction is the sum of the Néel coupling and the edge magnetic stray fields caused by the CoFe layers at the location of the soft magnetic layer as shown in Figure 6.6.

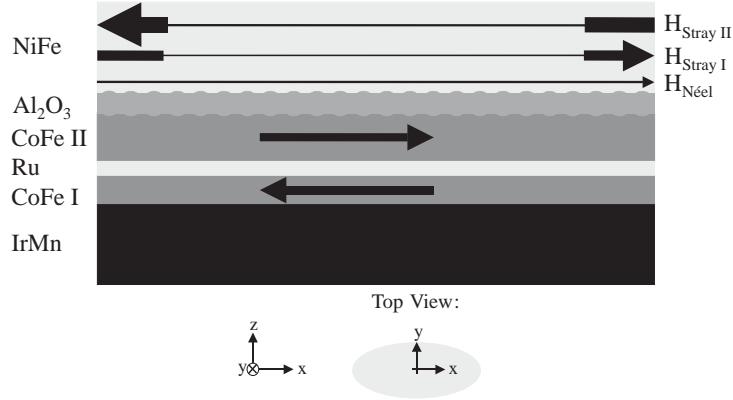


Figure 6.6: The homogeneously magnetized CoFe layers (I+II) that form the AFi cause magnetic stray fields  $H_{Stray I}$  and  $H_{Stray II}$  at the location of the soft magnetic NiFe layer of a tunneling element. The arrows show the orientation of the magnetizations along the x-axis within the AFi and the resulting x-components of the magnetic stray fields at the location of the NiFe layer. Their increased amplitudes at the edges are visualized by thicker parts of the arrows. In contrast, there is no enhancement of the Néel coupling field near the edges.

For a homogeneously magnetized elliptic CoFe layer, the resulting magnetic stray field is given by equation 6.5. At distances  $d$  typical for the separation of the soft magnetic layer from the reference layer(s), the in-plane component of the edge magnetic stray field acting on the soft magnetic layer differs from the in-plane component of the stray field in the CoFe layer (demagnetizing field) only in the order of one percent – this is valid for  $(d, c) \ll b \leq a$ , with  $a$  length,  $b$  width and  $c$  thickness of the CoFe layer. Hence the resulting magnetic stray field of an AFi, consisting of homogeneously magnetized layers, is well approximated by the stray field resulting from a single CoFe layer with the net magnetic moment of the AFi. Figure 6.2 shows the qualitative spatial dependence of the in-plane magnetic stray field acting on the soft magnetic layer. Obviously, the edge magnetic stray field favors an antiparallel coupling of the soft magnetic layer magnetic moment and the net magnetic mo-

ment of the AFi. Thus for SDT elements with ...IrMn7/CoFe2/Ru0.8/CoFe3/Al1.2 ox./NiFe6/Ta5 stack, the stray field coupling and the Néel coupling act in opposite directions.

The center of the astroid shown in Fig. 6.5 is shifted by  $350 \text{ Am}^{-1}$  along its easy axis ( $H_x$ ). Hence, in the  $4.2 \mu\text{m} \times 0.7 \mu\text{m}$  eye shaped SDT element the ferromagnetic Néel coupling is larger than the effective stray field coupling along the long axis. The astroid in Fig. 6.5 does not show an asymmetry with respect to the switching fields of parallel–antiparallel and antiparallel–parallel alignment of the (net) magnetic moments as reported in reference [57] for an elliptic element. Such an asymmetry is explained by the response of the soft magnetic layer near the edges to the sum of its demagnetizing field and the stray fields from the magnetic reference system. The consequences are usually edge domains. In the parallel alignment the resulting stray field near the edges is bigger than for the antiparallel alignment of the reference net magnetic moment and soft magnetic moment. Hence edge domains and the resulting switching behaviour are considered to be different, i. e. an asymmetry would result. For the minor loops of rectangular elements in Fig. 6.3, such an asymmetry is present. Its existence for rectangular elements is understandable by the higher demagnetizing fields near the edges for rectangular magnetic layers than for elliptical ones.

The center of the astroid in Fig. 6.5 exhibits also a shift along the hard axis respectively the  $H_y$ -axis which is caused by a  $y$ -component of the reference layers net magnetization [97]. From that shift of the astroid one can conclude a mismatch of  $6^\circ$  between the pinning direction of the AFi and the long axis of the STD elements [97].

### 6.2.3 Impact of the shape anisotropy on the astroid

Figure 6.7 shows the impact of the aspect ratio on the astroid curve for eye shaped SDT elements at width  $0.9 \mu\text{m}$ . The fits to the astroids were done by neglecting regimes where multiple domain switching was dominant. The origins for the deviations from the Stoner and Wohlfarth theory have been discussed in the previous section and do apply also to these measurements. The poor astroid for the eye shaped  $1.5 \mu\text{m} \times 0.9 \mu\text{m}$  SDT element is explained by multiple domain steps in nearly all minor loops due to a too small shape anisotropy and is neglected in the following analysis. A feature not discussed so far is a rotation up to  $5^\circ$  of some astroids in the  $H_x - H_y$ -plane. This is due to a slight mismatch of the long axis of the element with the easy axis of the uniaxial anisotropy which is in general a sum of contributions of the shape anisotropy and an intrinsic uniaxial anisotropy of the NiFe.

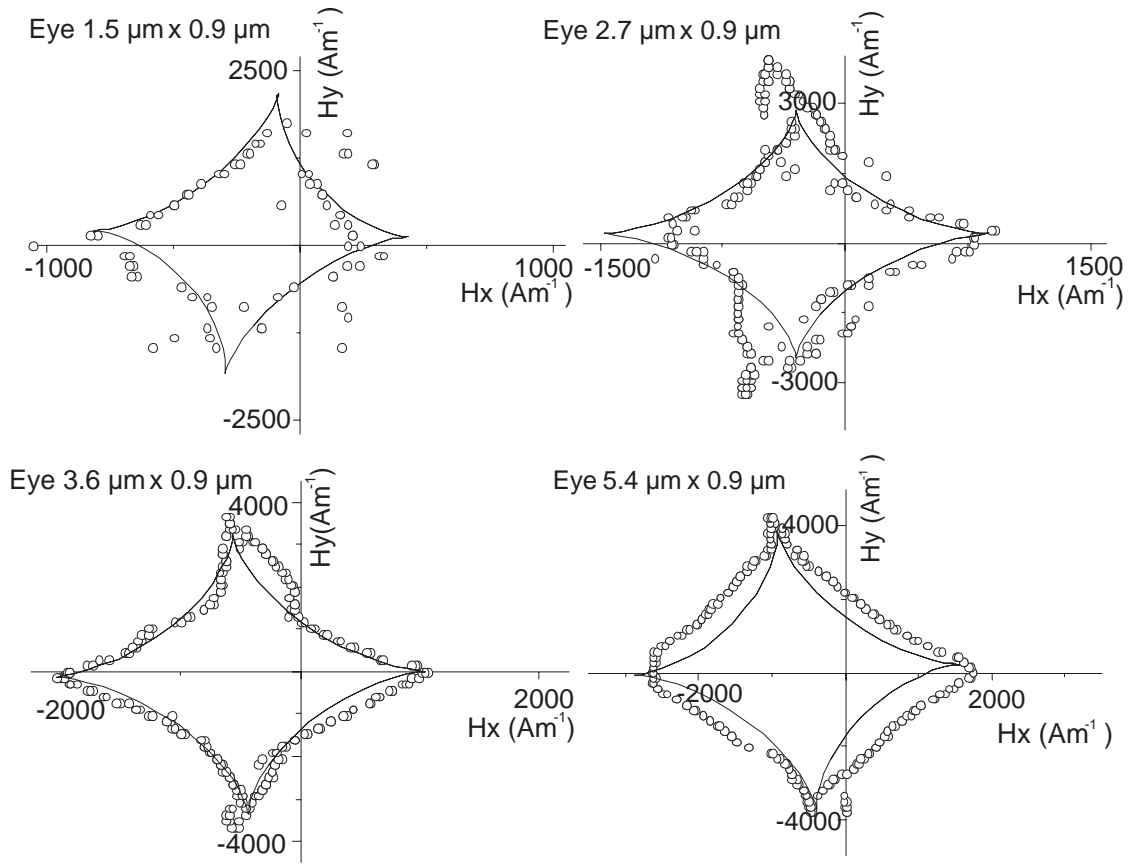


Figure 6.7: Astroids for eye shaped SDT elements of different aspect ratio.

Figure 6.8 shows the summary of the measurements in Fig. 6.7.  $H_k$ , extracted from the closing points of the fitted astroids, matches well with the theoretical  $H_k$  of a single NiFe layer according to equation 6.4. The theoretical  $H_k$  was calculated by considering the magnetization of the NiFe layer ( $M_S = 630 \text{ kAm}^{-1}$ ). The magne-

tization was gained from the magnetic moment as measured by vibrating sample magnetometer (VSM) divided by the nominal storage layer–volume of the sample. The oblate elliptically shaped soft magnetic layer was approximated by the general ellipsoid. The best fit of theory to the data extracted from the measurements was achieved for general ellipsoids with reduced aspect ratios (by 0.7).

$$H_k[\text{measured}] = H_k\left[\left(\frac{a}{b} - 0.7\right)\right]$$

$\frac{a}{b}$  is the aspect ratio. The reduced aspect ratio can be explained by regions of the NiFe layer which are occupied by domains. Thus NiFe layers with an aspect ratio below 1.7 cannot theoretically be described by a single domain particle.

The right part of Fig. 6.8 shows the systematics of the  $H_x$ –axis offset  $H_{xo} = H_{StrayField,AFi} - H_{Néel}$  due to the interaction with the AFi ( $H_{Néel} = 690 \text{ Am}^{-1}$ ). The higher the aspect ratio, the smaller the resulting edge magnetic stray field from the AFi is. The fit to theory is the edge magnetic stray field of a homogeneously magnetized general ellipsoid, where the AFi is approximated by its net magnetic thickness, a CoFe layer of 1 nm thickness with  $M_s = 1550 \text{ kAm}^{-1}$  as determined by VSM.

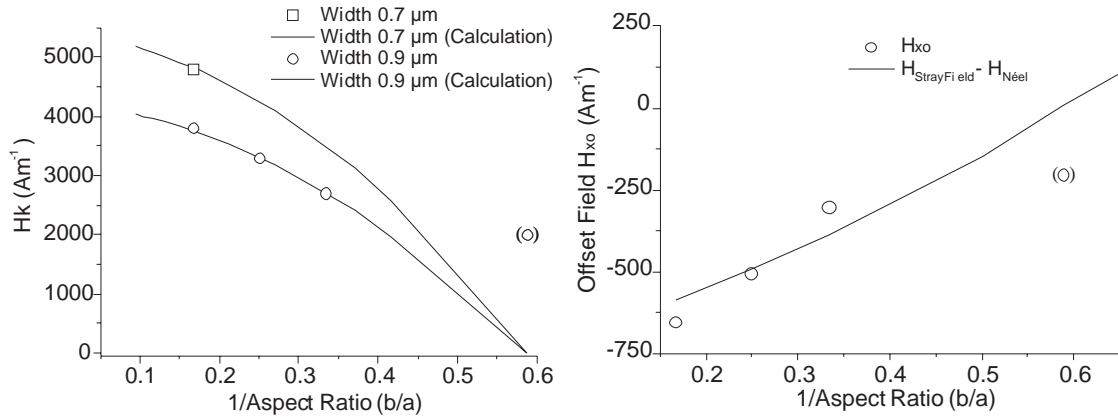


Figure 6.8: Left: Comparison of the anisotropy field  $H_k$  extracted from the astroids with theory. Shown is the best fit. Right: Comparison of the effective coupling field of the soft magnetic layers from Fig. 6.7 to theory. The AFi of the SDT elements is approximated by a 1 nm thick CoFe single layer.

Figure 6.9 shows an astroid of an eye shaped  $4.8 \mu\text{m} \times 0.8 \mu\text{m}$  SDT element with only a Ru 10/Co<sub>50</sub>Fe<sub>50</sub>1 reference layer system (Ru20/Ta5/Ru10/Co<sub>50</sub>Fe<sub>50</sub>1/Al1.2ox./NiFe5/Ta5), i. e. without exchange biasing by IrMn.

There are principal differences to the previously measured astroids, even the minor loops at high  $H_y$  exhibit stronger deviation from the Stoner and Wohlfarth theory. In the minor loop measurement, the  $H_x$  was only driven up to  $+4000 \text{ Am}^{-1}$ . A change of this value resulted in a change of the switching field of the subsequent AP–P reversal of the soft magnetic layer. As a consequence, the astroid in Fig. 6.9 is asymmetric with respect to its magnetic hard axis field. The higher the end field of the positive  $H_x$ , the higher is the astroids asymmetry. The fit to the astroid in Fig. 6.9 does not bear in mind this asymmetry.

The maximum  $H_k$  is larger than the theoretically expected one for the single NiFe element ( $3500 \text{ Am}^{-1}$ ).

Furthermore, there are two different reversal modes of the soft magnetic layer in the regime of low  $H_y$  and the  $TMR$  decreases with increasing  $H_y$ . The two different switching mechanisms between the high and low resistance states (AP–P) were already noted in Fig. 6.4. The reversal mechanism leading to a lower coercivity is reflected in Fig. 6.9 by the points in the interior of the astroid.

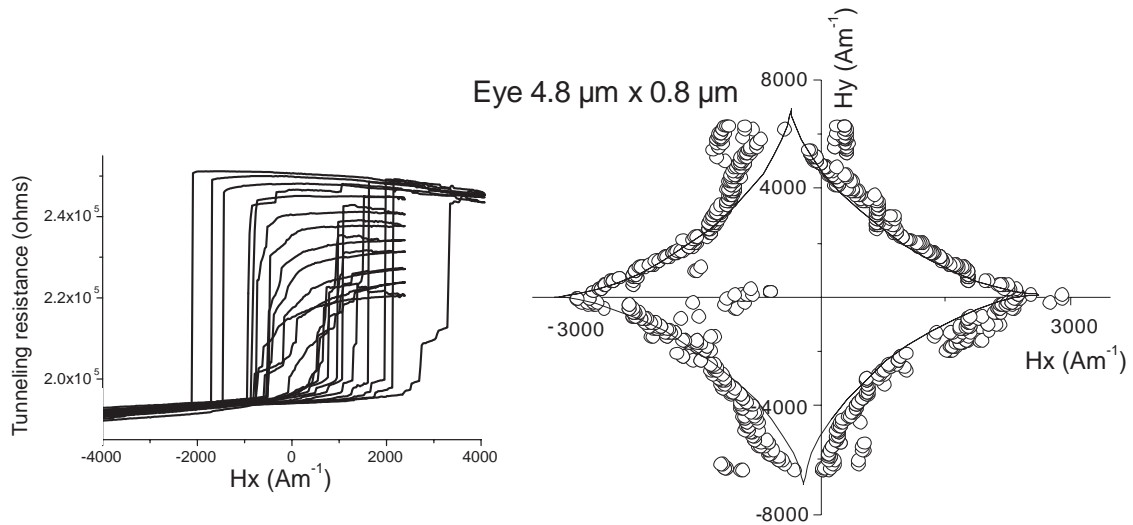


Figure 6.9: Astroid of a  $4.8 \mu\text{m} \times 0.8 \mu\text{m}$  SDT element with stack: Ru20/Ta5/Ru10/Co<sub>50</sub>Fe<sub>50</sub>1/Al1.2ox./NiFe5/Ta5. The amplitude of  $H_y$  was restricted in the measurement by the geometry of the corresponding current line.

These differences to the previous discussed astroids can be explained by the different reference layer systems.

Even though MOKE measurements showed that the direction of the intrinsic NiFe anisotropy (5–6 nm thick) depends on the reference layer system and on the thickness

of NiFe, its magnitude does only change slightly for the tunneling stacks compared here. This effect is hence not considered any more.

The  $\text{Co}_{50}\text{Fe}_{50}$  layer of the  $\text{Ru}/\text{Co}_{50}\text{Fe}_{50}$  system, however, is not saturated at remanence. Hysteresis curves of  $1\text{ cm} \times 1\text{ cm}$   $\text{Ru}$  (5–50 nm)/ $\text{Co}_{50}\text{Fe}_{50}$  (1–2 nm) samples measured by VSM show a remanent magnetization  $M_r$  in the order of 80 % of  $M_s$ . This is also true for the SDT elements which can be deduced from Fig. 6.4 (b) and (c). Due to the inhomogeneous configuration of the  $\text{Co}_{50}\text{Fe}_{50}$  magnetization ("ripple structure"),  $\vec{\nabla} \cdot \vec{M}$  is not zero, hence magnetic stray fields from the CoFe act on the NiFe layer. Obviously, when the configuration of the  $\text{Co}_{50}\text{Fe}_{50}$  magnetization changes, the stray fields acting on the NiFe change. These stray fields do have an impact on the domain structure of the NiFe layer and on its switching behaviour [98]. The larger  $H_k$  of the NiFe film compared to theory can be thus explained by a change of the CoFe magnetization. The coercivity of the hard magnetic CoFe 1 nm layer is measured by VSM to be  $10\text{ kAm}^{-1}$ . At high  $H_y$ , the shape of the minor loop deviates strongly from the switching curve of a Stoner and Wohlfarth particle. This is because not only the NiFe layer but both magnetic layer change their magnetization state. The lower  $TMR$  is mainly due to an increase of the  $y$  component of the CoFe magnetization with higher  $H_y$ . A  $y$  component of the CoFe magnetization causes (equation 6.5) an edge magnetic stray field (maximal  $1.7\text{ kAm}^{-1}$ ) oppositely orientated to the externally applied  $H_y$  on which the determined  $H_k$  is based. Also stray fields originating from the reference layer which act on the soft magnetic NiFe layer change. This can cause a change of the NiFe switching behaviour and can hence have an impact on the measured  $H_k$ .

Beside the increase of  $H_k$ , there are two different switching mechanisms in the AP–P reversal. The two characteristic switching modes in Figures 6.4 ((b)+(c)) and 6.9 exhibit two different  $TMR$  values, hence two different corresponding configurations of the magnetizations of CoFe or NiFe or both. The overall shape of the minor loops of the coexisting reversal mechanisms in Fig. 6.4 corresponds well with reversal mechanisms investigated by micromagnetic simulations in Reference [57]. The magnetic reversal mechanism exhibiting the lower switching field and the lower  $TMR$  has been explained by the creation of a  $360^\circ$  domain wall in the P–AP reversal prior to the AP–P reversal, where the reduced coercivity is explained by a start of the AP–P reversal from the middle of the  $360^\circ$  wall [57]. The second reversal mechanism does not have that resource of a domain and is hence characterized by a larger coercivity. A fact that supports the previous interpretation, is that in the regime of high  $H_k$  the reversal mechanism with lower  $TMR$  does not appear. According to Reference [99], the creation of the  $360^\circ$  domain walls is suppressed at high bias fields.

The choice of a  $\text{Ru}/\text{CoFe}$  reference layer system leads to more deviations from the

Stoner–Wohlfarth astroid as the choice of an exchange biased AFi (IrMn/CoFe/Ru/CoFe) reference system which magnetization is more stable when external magnetic fields in the order of the NiFe switching fields are present.

As a conclusion, for elliptically shaped SDT elements at widths of 1  $\mu\text{m}$  and below and for aspects ratio larger than 2 the shape anisotropy dominates over the intrinsic anisotropy and determines the switching behaviour for 6 nm respectively 5 nm thick NiFe.

The measured astroids exhibit deviations from the Stoner and Wohlfarth theory and are hence not simply explainable by a coherent rotation of the soft magnetic layer. The most obvious deviation is the presence of domain states in the minor loops.

For SDT elements based on a IrMn/CoFe/Ru/CoFe reference layer system, the anisotropy fields  $H_k$  of the soft magnetic NiFe layer fits well to the theoretical expected ones if one considers a reduced length (by 600 nm) of the SDT elements for the calculation compared to the real ones. This result suggests an interplay of edge domains with the domain in the main body. The astroid is determined by that interplay.

In contrast to measurements reported in Reference [97],  $\frac{H_c}{H_k}$  increases with increasing aspect ratio.

The choice of a Ru/CoFe reference layer system leads for the soft magnetic NiFe layer to more deviations from the Stoner–Wohlfarth astroid as the exchange biased AFi (IrMn/CoFe/Ru/CoFe) reference system where the magnetization is more stable.



# Chapter 7

## Programmable reference layer

### 7.1 Calculation of magnetic fields versus currents on-chip

By introducing a reference layer system, which can be switched (programmed) by a current on-chip, one increases the degrees of freedom per SDT element. This gives in a larger number of programmable logic functions in the magnetic part of a spin-logic gate.

When choosing a programmable reference layer system, one must consider the upper limit of the magnetic field which can be generated at the location of the magnetic layers (critical magnetic field) by a current on-chip. The critical magnetic field depends, beside the material parameters, on the geometrical shape of the current line and its distance to the magnetic reference layer system. A cross section of the geometry current line-SDT element of a field programmable spin-logic gate is shown in Fig. 7.1.

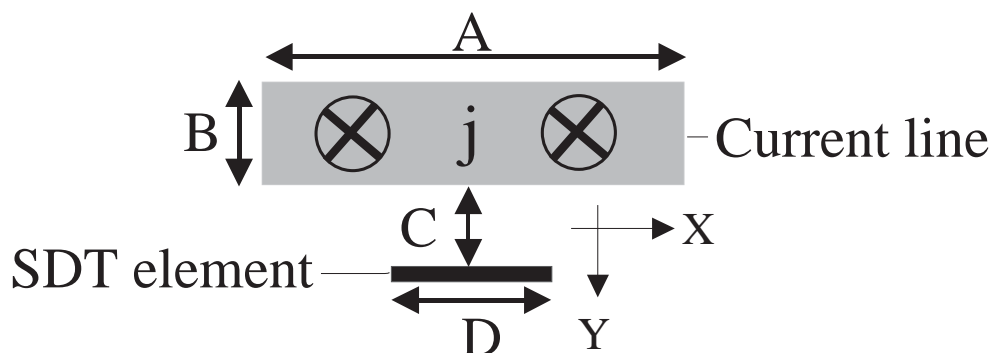


Figure 7.1: A current density  $j$  in the current line of width  $A$  and thickness  $B$  generates a magnetic field at the location of the SDT element at a distance  $C$  from the current line.  $D$  is the length of the long axis of the SDT element.

The skin penetration depth at an appropriate operating frequency in the order of 1 GHz is about 2  $\mu\text{m}$  for copper [100], for the calculation of the critical magnetic field it is therefore reasonable to assume a homogeneous current distribution in the line.

Moreover, an infinitely long current line with rectangular cross section is assumed, so the resulting magnetic field vector lies in the  $X - Y$  plane of figure 7.1.

Due to the shape anisotropy, the magnetic field perpendicular ( $H_Y$ ) to the thin magnetic films of the SDT element needs not to be considered.

The component  $H_X$  in the plane of the thin magnetic films was calculated numerically, starting with Biot–Savarts law by:

$$\vec{H}(\vec{r}) = \frac{jz}{4\pi} \int_{-\frac{A}{2}}^{+\frac{A}{2}} \int_{-\frac{B}{2}}^{+\frac{B}{2}} \int_{-\infty}^{+\infty} \begin{pmatrix} -(y - y') \\ (x - x') \\ 0 \end{pmatrix} \cdot \frac{1}{((x - x')^2 + (y - y')^2 + z'^2)^{\frac{3}{2}}} dx' dy' dz' \quad (7.1)$$

A critical current density  $j_{CR}$  of  $10^{11} \text{ Am}^{-2}$  can be applied to a copper line without causing its failure. For the calculation of the critical magnetic field by equation 7.1, a critical current density  $j_{CR}$  of  $10^{11} \text{ Am}^{-2}$  is used. For ac currents, higher (peak) values of  $j_{CR}$  are possible.

The results for  $j_{CR} = 10^{11} \text{ Am}^{-2}$  are summarized in figure 7.2 a – e.

$H = k \cdot I$  ( $I$ : current) was measured and the constant  $k$  was determined for a current line with a  $30 \mu\text{m} \times 0.5 \mu\text{m}$  cross section. The generated magnetic field turned out to be in accordance with equation 7.1 within 5 %. The error is due to the deviations of the current line on–chip from the rectangular cross section and its uneven track in the vicinity of the tunneling element (as shown in Fig. 4.6). The calibration was performed by generating a magnetic offset field at the location of the SDT element by applying a constant current to the current line and measuring the minor loop. The shift of the minor loop,  $\Delta H$ , versus the current or the current density, respectively, is shown in Fig. 7.2 (e).

In the field programmable spin–logic device as shown in Fig. 3.4, a current line does have a cross section of  $10 \mu\text{m} \times 0.5 \mu\text{m}$  and is separated by 200 nm from the magnetic layers of the SDT element (distance  $C$  in figure 7.1). As seen in figure 7.2 (a), the critical magnetic field  $H_{XCR}$  at  $C = 200 \text{ nm}$  below the center of the current line is about  $23 \text{ kAm}^{-1}$ . Note, that ( $H_{XCR}$ ) varies slightly along the location of the SDT element ( $x$ –axis) at constant  $C$ . Regarding a higher integration density of spin–logic, this variation increases for a smaller width  $A$  of the current line. Secondly the critical magnetic field  $H_{XCR}$  is decreasing width decreasing width  $A$  at constant  $C$ , as can be seen in Fig. 7.2 (b).

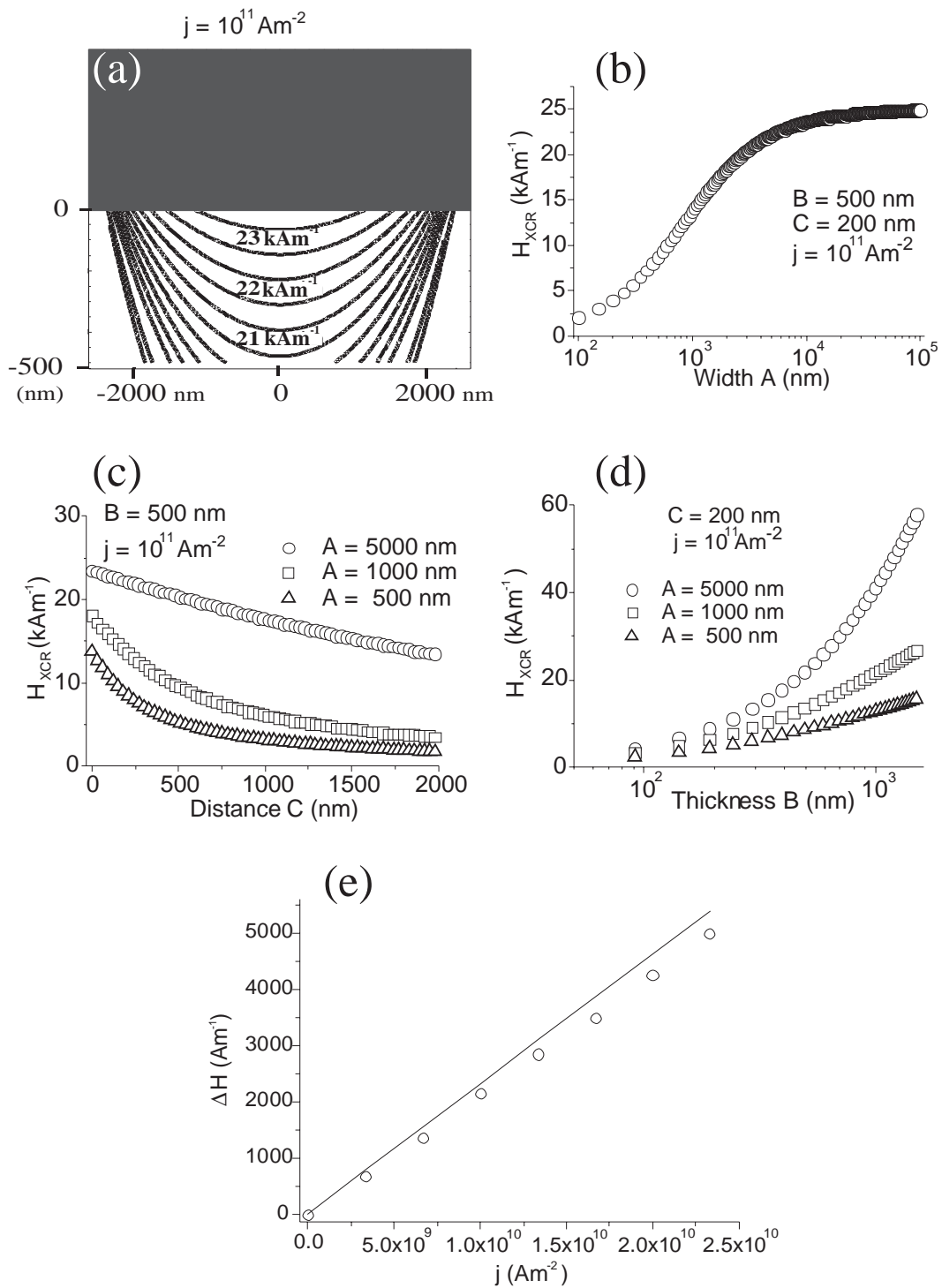


Figure 7.2: Calculated magnetic field component  $H_{XCR}$  generated by a current density of  $j_{CR} = 10^{11} \text{ Am}^{-2}$  in the current line of Fig. 7.1. Part (a) shows a contour plot of constant magnetic field below a current line with  $5000 \times 500 \text{ nm}^2$  cross section. Parts (b) and (d) shows the dependencies of  $H_{XCR}$  below the center of the current line on the width  $A$  and thickness  $B$ , (c) shows the variation of the magnetic field  $H_{XCR}$  with distance  $C$  below the center of the current line. (e): The result of a calibration measurement on a current line with  $30 \mu\text{m} \times 0.5 \mu\text{m}$  cross section ( $\circ$ ) is compared to calculation ( $-$ ).

In Fig. 7.2 (c), the dependence of  $H_{XCR}$  with distance  $C$  is plotted for different widths  $A$ . The smaller  $A$ , the higher the variation of  $H_{XCR}$  is in the region of interest, below  $C = 200$  nm. A possibility to increase the critical magnetic field  $H_{XCR}$  is obviously the increase of the thickness  $B$  of the current line, as can be concluded from Fig. 7.2 (d).

With a current line of width  $A = 500$  nm and thickness  $B = 2000$  nm one can generate a field of  $18 \text{ kAm}^{-1}$  at  $C = 200$  nm.

A further increase of  $H_{XCR}$  by a factor of two can be achieved by a partial surrounding of the current line with a magnetic film [101].

Regarding the coercivity of a programmable reference layer, this value can be bigger than  $H_{XCR}$ , since in a logic gate there can be a second current line running perpendicular to the first one below the SDT element at the same distance  $C$ . The bias magnetic field generated by a current in the additional current line reduces the switching field of the magnetic layers for SDT elements exhibiting 2-D switching behaviours characterized by an astroid [48]. Hence current lines at widths of 500 nm are capable to switch a reference layer on-chip with a coercivity of up to the order of  $50 \text{ kAm}^{-1}$ .

Of course this value can be increased by applying current densities higher than  $10^{11} \text{ Am}^{-2}$  to the current lines, which is possible without damaging the current line (ac, pulsed-currents, which would be the case in a device anyway).

### 7.1.1 Cross-talk in spin-logic gates

$H_{XCR}$  is not the only criterion that determines the coercivity of a programmable reference layer. The effect of the programming magnetic field on the not addressed SDT elements within a spin-logic gate (cross-talk) has also be taken into consideration. When programming a magnetic reference layer, the soft magnetic layers of the other SDT elements within a spin-logic gate must be unaffected since some of them store programming information, too. Obviously, the higher the integration density of a spin-logic gate is, the more critical becomes the cross-talk. A quantitative analysis on the cross-talk in a spin-logic gate is shown in Fig. 7.3.

The cross-talk magnetic field cannot be neglected for spin-logic gates at integration densities with a sub- $\mu\text{m}$  minimal feature size (which is roughly the width  $A$  of the current line). The distance between the centers of neighboring SDT elements is exemplarily chosen to be  $2 \cdot A$  in the analysis. The higher the integration density, the higher is the normalized magnetic in-plane field at the location of the SDT elements in the neighborhood of the addressed SDT element (cross talk field). For a spin-logic gate with current lines of cross section  $180 \text{ nm} \times 180 \text{ nm}$  and SDT elements separated by  $C = 200$  nm from the current lines, the cross-talk field at the center

of the neighboring SDT elements is nearly 50 % of the magnetic field at the center of the addressed SDT element.

If one considers the worst scenario for the cross-talk, which is the case when beside one SDT element in the middle of a spin-logic gate all reference layers are programmed simultaneously, the normalized (with respect to the magnetic field at the center of an addressed SDT element) cross-talk field is about 1 at the location of the not addressed SDT element.

The cross-talk fields corresponding to the worst case are at least a factor of 2 larger than the fields shown in Fig. 7.3. As shown in Fig. 7.3 (b) and (c), the cross-talk field can be reduced by decreasing the distance  $C$  and lowering the aspect ratio  $B/A$  of the current line.

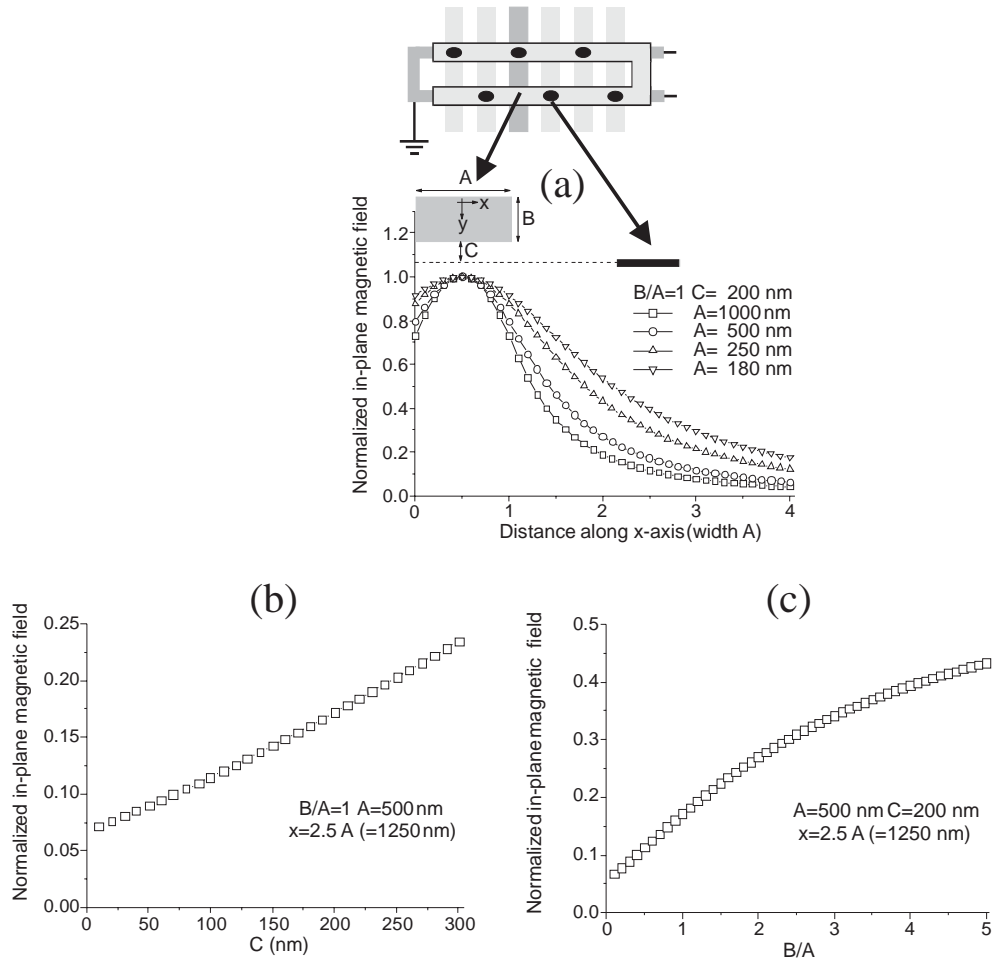


Figure 7.3: (a) In-plane magnetic field component  $H_X$ , normalized to its maximum value below the center of the magnetic field inducing current line at  $C = 200$  nm, versus  $x$  in terms of the width  $A$  of the current lines. The cross section of the current line is chosen to be quadratic ( $B/A = 1$ ). One of the neighboring SDT elements is drawn at  $x = 2.5 A$ , the exact value depends on the fabrication process. (b) Dependence of the magnetic field at  $x = 2.5 A$  on the distance  $C$  between the current lines and the SDT elements of a spin-logic gate. (c) Dependence of the magnetic field at  $x = 2.5 A$  on the aspect ratio  $B/A$  of the current lines.

The cross-talk field or  $H_{XCR}$  determine the upper limit of the coercivity of a programmable reference layer system in a working spin-logic gate. Hence this limit is a consequence of the integration density, the critical current density of the current lines, the geometry of the current lines cross section and on the fabrication process with respect to the minimal achievable  $C$  and with respect to the separation of the SDT elements within a spin-logic gate.

## 7.2 Programmable reference layer system Ru/CoFe

The coercivity of  $\text{Co}_{50}\text{Fe}_{50}$  grown on Ru is in the regime of interest of a programmable reference layer system. As shown for  $\text{Co}_{50}\text{Fe}_{50}$ ,  $H_c$  increases with increasing thickness of the Ru-buffer and is maximal for a thickness of the  $\text{Co}_{50}\text{Fe}_{50}$  between 1.5 nm and 2 nm. Beyond a Ru thickness of 50 nm,  $H_c$  reaches a saturation value.

The  $\text{Co}_{90}\text{Fe}_{10}$  alloy exhibit qualitatively the characteristic as shown in Fig. 7.4, but with lower coercivities [102].

Ru is *dc* magnetron sputtered and its crystal structure is hexagonal close-packed (hcp), [103] [104] which is confirmed by X-ray diffraction measurements (table 7.1). Under normal conditions,  $\text{Co}_{50}\text{Fe}_{50}$  does have body centered cubic (bcc) and  $\text{Co}_{90}\text{Fe}_{10}$  face centered cubic (fcc) crystal structure. The bcc crystal structure for  $\text{Co}_{50}\text{Fe}_{50}$  sputtered on ruthenium could not be confirmed for thicknesses below 3 nm due to the small X-ray diffraction signal from the  $\text{Co}_{50}\text{Fe}_{50}$  layer.

The  $\text{Co}_{50}\text{Fe}_{50}$  does not exhibit a macroscopic easy axis on the scale measured by VSM, i. e. the  $\text{Co}_{50}\text{Fe}_{50}$  layer is isotropic. The  $\text{Co}_{50}\text{Fe}_{50}$  is rf magnetron sputtered.

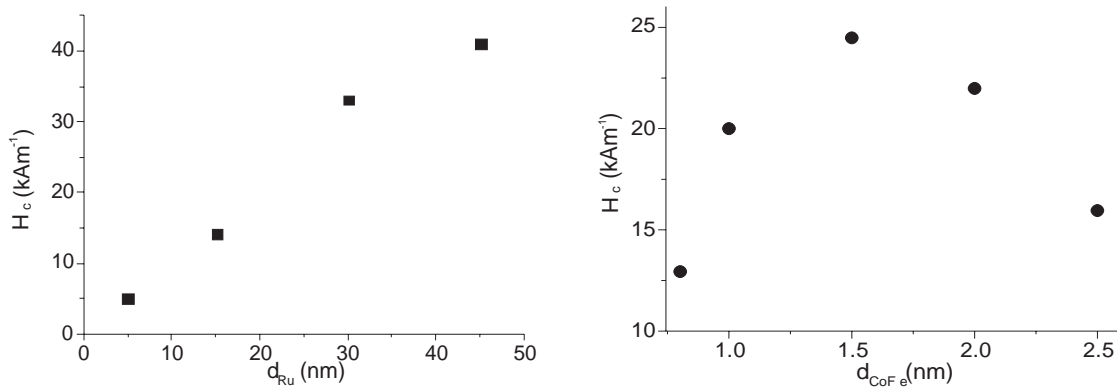


Figure 7.4: Left: Coercivity of a 2 nm thick  $\text{Co}_{50}\text{Fe}_{50}$  layer versus the thickness of the Ru-buffer [105]. Complete stack:  $\text{Ru}_{d_{\text{Ru}}}/\text{Co}_{50}\text{Fe}_{50}2/\text{Ru}5$ . Right: Dependence of the coercivity of  $\text{Co}_{50}\text{Fe}_{50}$  on its thickness (Ru 25/ $\text{Co}_{50}\text{Fe}_{50}d_{\text{Co}_{50}\text{Fe}_{50}}/\text{Al}1.2 \text{ ox.}/\text{NiFe}6/\text{Ta}2/\text{Ru}3/\text{Ta}5$ ).

Figure 7.5 shows the results of X-ray diffraction measurements ( $\theta-2\theta$ -scan [106]) using Cu  $K\alpha 1$  ( $\lambda = 1.5405\text{\AA}$ ) radiation on a series of samples (Ru/ $\text{Co}_{50}\text{Fe}_{50}$ /protection cap) and table 7.1 summarizes the results [107]. The samples are rotated around an axis parallel to the surface of the wafer, hence the Ru crystal planes corresponding to the measured Bragg-peaks lies parallel to the surface of the wafer [108]. The relative amounts of crystal directions (hkl) are extracted from the intensity scattered in the corresponding Bragg-peak. The  $\text{Co}_{50}\text{Fe}_{50}$  thickness is too low for a Bragg-peak signal higher than the background scattering signal. Thus crystallographic information is only gained for the Ru-buffer layer.

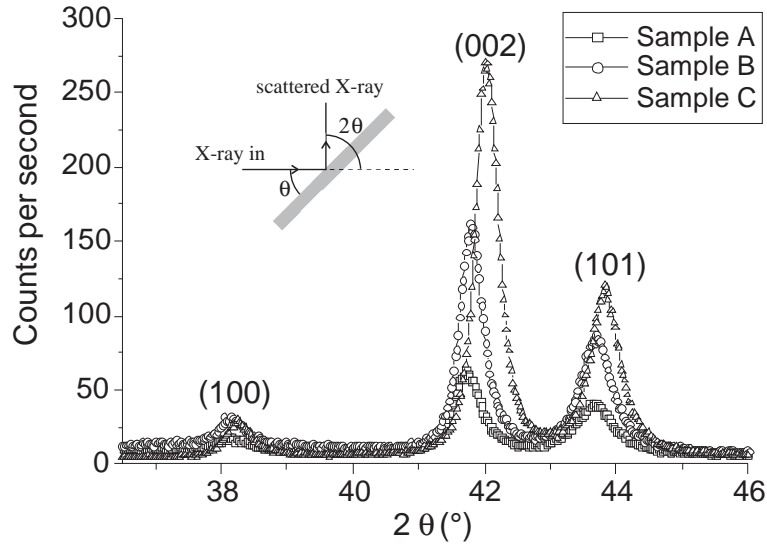


Figure 7.5: XRD pattern for three different samples. A: Ru25/Co<sub>50</sub>Fe<sub>50</sub>2/Ta10. B: Ru40/Co<sub>50</sub>Fe<sub>50</sub>1.5/Ta10. C: Ru50/Co<sub>50</sub>Fe<sub>50</sub>1.5/Al1.5 ox.. The Bragg-peaks are due to the ruthenium.

Sample A: Ru25/Co<sub>50</sub>Fe<sub>50</sub>2/Ta10  
Sample B: Ru40/Co<sub>50</sub>Fe<sub>50</sub>1.5/Ta10  
Sample C: Ru50/Co<sub>50</sub>Fe<sub>50</sub>1.5/Al1.5 ox.

|                                     | Sample A             | Sample B             | Sample C             | polycrystalline |
|-------------------------------------|----------------------|----------------------|----------------------|-----------------|
| $2\theta(100)$                      | 38.15°               | 38.03°               | 38.25°               | 38.385°         |
| $2\theta(002)$                      | 41.71°               | 41.77°               | 42.00°               | 42.151°         |
| $2\theta(101)$                      | 43.63°               | 43.69°               | 43.83°               | 44.00°          |
| share (100)                         | 9 %                  | 9 %                  | 6 %                  | 23 %            |
| share (002)                         | 51 %                 | 56 %                 | 60 %                 | 20 %            |
| share (101)                         | 40 %                 | 35 %                 | 34 %                 | 57 %            |
| Grain size (X-ray)                  | 19–25 nm             | 23–30 nm             | 23–27 nm             | –               |
| Grain size (AFM)                    | 15–20 nm             | –                    | 20–25 nm [109]       | –               |
| $H_c(\text{Co}_{50}\text{Fe}_{50})$ | 16 kAm <sup>-1</sup> | 24 kAm <sup>-1</sup> | 40 kAm <sup>-1</sup> | –               |

Table 7.1: Results of the X-ray diffraction measurement. The relative shares of the crystal directions of Ru are concluded from the intensity  $I_{hkl}$  scattered in the corresponding Bragg-peaks with respect to the total scattered intensity ( $\frac{I_{hkl}}{I_{100}+I_{002}+I_{101}}$ ) [107]. As a reference, the intensities of a polycrystalline Ru reference sample are given with the same normalization ( $\frac{I_{hkl}}{I_{100}+I_{002}+I_{101}}$ ) [108]. The grain size is derived from the angular broadening of the Bragg peaks [79].

The diffraction measurements confirm the hcp crystal structure of ruthenium and shows three different Bragg-peaks which correspond to the planes parallel to the substrate. The grains grow either hcp(100), hcp(002) or hcp(101). The Bragg-angles are smaller than the theoretical ones and these values increase slightly towards the theoretical Bragg-angle with increasing thickness of the ruthenium. That tendency



can be explained by a shift of the mean lattice constant of hcp ruthenium towards its equilibrium values with increasing thickness. On the other hand, the change of the Bragg-angles might be due to misalignment of the samples.

In comparison to the relative intensities of a ruthenium powder sample [108], the grains of the ruthenium buffer grow preferentially hcp(002). Furthermore, the bigger the thickness of the ruthenium buffer, the higher the hcp(002) share is, hence the fraction of grains with hcp(002) orientation at the Ru/Co<sub>50</sub>Fe<sub>50</sub> boundary increases with increasing thickness of the ruthenium. The approximate range of the grain size is calculated from the width of the Bragg-peaks by the Scherrer formula [79]. There is no significant change of the grain size(s) with increasing thickness (25–50 nm) of the ruthenium buffer.

Figure 7.6 shows a High Resolution Transmission Electron Microscope (HRTEM) picture of the cross section of a Ru5/Co<sub>50</sub>Fe<sub>50</sub>1.5/Ta10 sample [110]. The brightness corresponds to the intensity of electrons transmitted through the sample, which is proportional to the atomic number  $Z$  of the material. From bottom to top the sequence of the layer system is given by its degrees of brightness. The sequence is: Si/SiO<sub>2</sub>/Ru/Co<sub>50</sub>Fe<sub>50</sub>/Ta. Ru ( $Z = 44$ ) and Ta ( $Z = 73$ ) are separated by a bright, extremely fine layer. Beside its nominal location, the atomic numbers of Co<sub>50</sub>Fe<sub>50</sub> ( $Z = 27, 26$ ) makes it reliable to identify the region of the bright, extremely fine layer by Co<sub>50</sub>Fe<sub>50</sub>.

The granular composition of ruthenium and the atomic structure (texture) of some grains is well shown in Fig. 7.6 (a). The average width of the ruthenium grains (grain size) is 4.5 nm. In some areas of Fig. 7.6 (a)–(c), the texture of the Ru continues into the brighter regions that separates the Ru and Ta.

Fourier transformations are performed on two different grains. The areas transformed are marked in Fig. (b) and (c), the corresponding transformation is shown on the right. From the reciprocal lattice vectors  $\vec{g}_{ghl}$ , which points perpendicular to the corresponding lattice planes, the distance  $d_{ghl}$  between the corresponding family of planes can be calculated [111]. From the value of  $d_{ghl}$  and the known lattice parameters of hcp Ru ( $a : 2.7058\text{\AA}$ ,  $c : 4.2819\text{\AA}$ ) [108], the Miller indices (hkl) are concluded and given in Fig. 7.6. The Bragg-peaks (hkl) detected in the measurement of Fig. 7.5 correspond to Ru grains with the  $\vec{g}_{hkl}$  pointing normal to the substrate. The two grains analyzed in Fig. 7.6 correspond to the (100) and (101) Bragg-peaks.

Furthermore, the angle between the (100) and (101) planes match with theory.

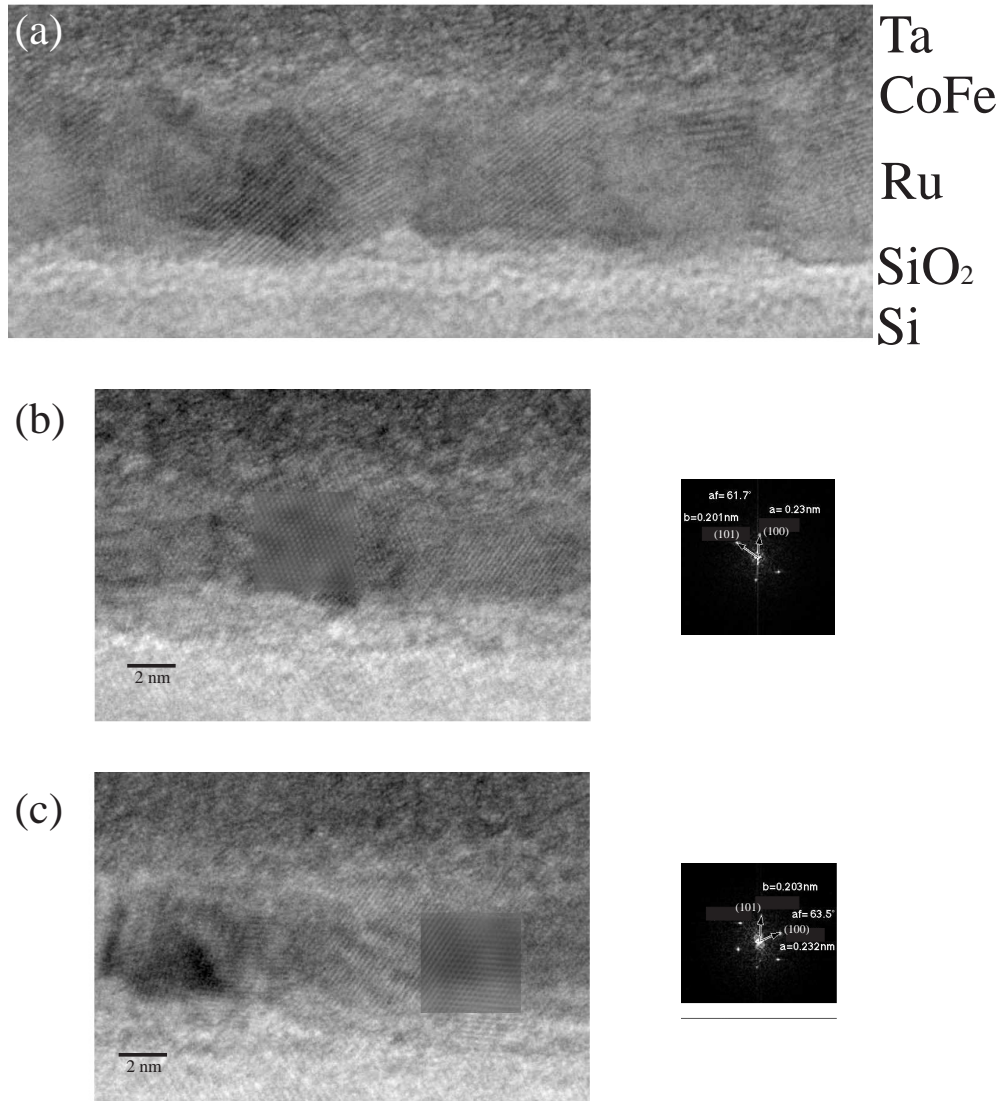


Figure 7.6: HRTEM picture of a Ru<sub>5</sub>/Co<sub>50</sub>Fe<sub>50</sub><sup>1.5</sup>/Ta<sub>10</sub> cross section [110]. In (b) and (c), the texture of two Ru grains is determined.

The following list discusses possible origins for the increasing coercivity of Co<sub>50</sub>Fe<sub>50</sub> with increasing Ru thickness.

- The surface roughness of an ultrathin magnetic layer leads to an increase of the in-plane demagnetizing factor which consequences in an enhanced coercivity [112]. The surface roughness might contribute to the high coercivity of Co<sub>50</sub>Fe<sub>50</sub> sputtered on Ru, but does not explain the strong dependence of the Co<sub>50</sub>Fe<sub>50</sub> coercivity on the thickness of the ruthenium buffer. Theoretically, the change of coercivity due to surface roughness scales with the root-mean-square (rms) roughness [112]. The coercivity of 0.8 nm thick Co<sub>50</sub>Fe<sub>50</sub> on Ru (Ru<sub>25</sub>/Co<sub>50</sub>Fe<sub>50</sub><sup>0.8</sup>/Al<sub>1.2</sub> ox) increases by 13 %, if it is grown

on Ru5/Cu30/Ru30 (Ru5/Cu30/Ru30/Co<sub>50</sub>Fe<sub>50</sub>0.8/Al1.2 ox.).

The increase of the Néel coupling field due to the higher degree of roughness introduced by the copper is shown in Fig. 7.7. From AFM measurements the increase of the rms-value is determined from 2.2 Å (Ru25/Co<sub>50</sub>Fe<sub>50</sub>0.8/Al1.2 ox) to 6.0 Å (Ru5/Cu30/Ru30/Co<sub>50</sub>Fe<sub>50</sub>0.8/Al1.2 ox.).

The rms-value of Ru 5 nm was measured to be 1.15Å, for Ru 40 nm 2.5Å. This rms-value measurement sets the upper limit for an increase of the Co<sub>50</sub>Fe<sub>50</sub> coercivity to 11% when increasing the ruthenium buffer from Ru 5 nm to Ru 40 nm. Hence surface roughness is not the origin of the dependence of the coercivity of Co<sub>50</sub>Fe<sub>50</sub> on the thickness of the Ru-buffer.

- The growth of the magnetic reference electrode on top of the bottom electrode was determined to be columnar [109]. Hence the grain size of Co<sub>50</sub>Fe<sub>50</sub> correlates with that of the underlying Ru-buffer. AFM measurements on Ru25 and Ru25/Co<sub>50</sub>Fe<sub>50</sub>1.5 showed the same wavelength of roughness. According to the results from the XRD experiment, the average grain size of Ru (thicknesses  $\geq 25$ nm) and hence Co<sub>50</sub>Fe<sub>50</sub> does change slightly, only.

On the other hand, the grain size increases significantly between Ru thicknesses 5 nm and 25 nm, namely from 5 nm (Fig. 7.6) to 15–20 nm (Table 7.1). For both, in the regime with nearly no change and in the regime with a significant change of the grain size, the coercivity of Co<sub>50</sub>Fe<sub>50</sub> increases with thickness of the Ru-buffer. Hence the data indicate that the grain size of Co<sub>50</sub>Fe<sub>50</sub> is not the origin of the increase of Co<sub>50</sub>Fe<sub>50</sub> coercivity.

- Annealing at a temperature of 300 °C leads for the Co<sub>50</sub>Fe<sub>50</sub> (Ru/Co<sub>50</sub>Fe<sub>50</sub>) to a slightly enhanced coercivity. This indicates that stress and stress release at higher temperatures do have no impact on the high coercivity of Co<sub>50</sub>Fe<sub>50</sub> on ruthenium.
- According to the results of the XRD analysis in table 7.1, the fraction of grains with hcp (002) direction at the Co<sub>50</sub>Fe<sub>50</sub>/Ru interface which points out of the Ru surface increases with increasing thickness of the ruthenium buffer at the expense of hcp (101) and hcp (100).

Co<sub>50</sub>Fe<sub>50</sub> sputtered rf diode exhibits a low coercivity ( $< 5$ kAm<sup>-1</sup>) and does not show the investigated characteristic of Fig. 7.4. Contrary, Co<sub>50</sub>Fe<sub>50</sub> sputtered rf magnetron shows the high coercivities. Generally, different sputtering modes can cause different textures [79] which indicates that a special texture of CoFe might be the reason of the high coercivities.

From the HRTEM-pictures like in (Fig. 7.6), the crystallographic structure of the Co<sub>50</sub>Fe<sub>50</sub> could not be concluded.

The measurements performed make it conclusively, although not proven here,

that the high coercivity of  $\text{Co}_{50}\text{Fe}_{50}$  is due to its texture, which is itself determined by the texture of the underlying ruthenium buffer. Bcc (110)  $\text{Co}_{50}\text{Fe}_{50}$ , for instance, fits to hcp (002) Ru atom by atom, if two side lengths of the bcc cubus are expanded by 16 % and the remaining width is shrunken by 6 %. Such a distorted bcc  $\text{Co}_{50}\text{Fe}_{50}$  grain would exhibit a changed spin-orbit coupling of the electrons, leading to a stress induced uniaxial anisotropy.

This stress induced, uniaxial magnetoelastic anisotropy is given by  $K_\sigma = \frac{3}{2} \cdot \lambda_s \cdot \sigma$ , [113] where  $\lambda_s$  is the saturation magnetostriction and  $\sigma$  is the stress applied to the material. The stress required to expand the  $\text{Co}_{50}\text{Fe}_{50}$  bcc cubus by 16% is given by  $\sigma = E \cdot 0.16$ , hence  $K = \frac{3}{2} \cdot \lambda_s \cdot E \cdot 0.16$ . The E modulus of Co and Fe is in the order of  $2 \cdot 10^5 \frac{\text{N}}{\text{mm}^2}$ ,  $\lambda_s$  for  $\text{Co}_{50}\text{Fe}_{50}$  is reported to be in the order of  $60 \cdot 10^{-6}$  [113]. Thus the value of  $K_\sigma$  for expanding the  $\text{Co}_{50}\text{Fe}_{50}$  cubus by 16% is approximated by  $K_\sigma = 2.9 \cdot 10^6 \frac{\text{J}}{\text{m}^3}$ . The intrinsic (magneto-crystalline) anisotropy constant  $K_c$  for  $\text{Co}_{50}\text{Fe}_{50}$  (cubic anisotropy) depends on the thickness of the crystal, magnitudes between  $4 \cdot 10^4 \frac{\text{J}}{\text{m}^3}$  and  $1 \cdot 10^6 \frac{\text{J}}{\text{m}^3}$  are reported [114] [115]. Hence the stress induced anisotropy is bigger than the magneto-crystalline anisotropy for the distorted bcc cubus. That leads to an increase of  $H_k$  for a  $\text{Co}_{50}\text{Fe}_{50}$  grain with the distorted cubic cells. The coercivity of a  $\text{Co}_{50}\text{Fe}_{50}$  film formed by such grains increases with increasing  $H_k$  of the grains, [113] hence for the case that distorted  $\text{Co}_{50}\text{Fe}_{50}$  grains grow on hcp (002) Ru, the increase of the  $\text{Co}_{50}\text{Fe}_{50}$  coercivity with increasing Ru thickness would be explained by the increasing fraction of hcp (002) texture as determined experimentally (table 7.1).

Another scenario is that a ferromagnetic hcp  $\text{Co}_{50}\text{Fe}_{50}$  grows on the hcp (002) Ru for the first atomic layers. A similar behaviour is reported for the system  $\text{Re}(001)/\text{Fe}(8 \text{ \AA})$ , where ferromagnetic Fe grows hcp for the first atomic layers. The stable ferromagnetic structure of Fe under normal conditions is bcc [116] References [117] [118] are also concerned with hcp Fe. Such an imposition of the crystallographic structure for the first atomic layers by the underlying buffer is a well known phenomena from the growth of semiconducting material.

### 7.2.1 Finite thickness effect of the $\text{Co}_{50}\text{Fe}_{50}$ reference layer on the Néel coupling

In order to have a nonvolatile programming information in spin–logic gates, the Néel coupling field has to be smaller than the coercivity of the soft magnetic layer. The rms value of the roughness of the ruthenium surface lies in the regime of  $1\text{Å} - 3\text{Å}$  for thicknesses up to 100 nm which turned out to be less than the rms value of copper ( $5\text{Å} - 9\text{Å}$ ), hence the Néel coupling is smaller when Ru is used instead of Cu to form the bottom electrode. Beside the parameters discussed by Néel (equation 2.15), the Néel coupling field depends also on the thicknesses of the magnetic reference layer:

$$H_{N\acute{e}el} = H_{0N\acute{e}el} \cdot \left[ 1 - \frac{a_1}{a_2} \cdot e^{-\frac{2\pi \cdot \sqrt{2} \cdot d_{\text{Co}_{50}\text{Fe}_{50}}}{\lambda}} \right] \cdot \left[ 1 - e^{-\frac{2\pi \cdot \sqrt{2} \cdot d_{\text{NiFe}}}{\lambda}} \right] \quad (7.2)$$

Equation 7.2 describes the Néel coupling under the consideration of the finite thicknesses of the magnetic layers [119] [120]. The formula is derived with a model for the roughness described by a two dimensional sinusoidal wave with wavelength  $\lambda$  and amplitudes  $a_i$ .  $\lambda$  is assumed to be identical for all interfaces which is reliable if the grain structure of the magnetic layers is columnar at all interfaces meaning that the first sputtered layers gives the initial grain structure. This is the case for the tunneling systems investigated here [109]. In terms of the  $\text{Ru}/\text{Co}_{50}\text{Fe}_{50}/\text{Al}_2\text{O}_3/\text{NiFe}$  system,  $a_1$  is the amplitude of the waviness at the  $\text{Ru}/\text{Co}_{50}\text{Fe}_{50}$  interface and  $a_2$  is that of the  $\text{Co}_{50}\text{Fe}_{50}/\text{Al}_2\text{O}_3$  interface,  $d_{\text{Co}_{50}\text{Fe}_{50}}$  is the thickness of the  $\text{Co}_{50}\text{Fe}_{50}$ ,  $d_{\text{NiFe}}$  the thickness of the NiFe.  $H_{0N\acute{e}el}$  is the coupling field as suggested by Néel (equation 2.15).

According to Néel, the net ferromagnetic coupling results from the magnetostatic interactions between the two interfaces which exhibit a correlated interface roughness separated by the tunneling barrier [49]. For thicknesses of the magnetic layers less than the wavelength  $\lambda$  (equation 2.15) of the correlated roughness waviness, the outer surfaces of the magnetic layers cannot be neglected any more. The two surfaces of the reference layer interact magnetostatically with the two surfaces of the soft magnetic layer, hence there are in sum four interactions, where two are ferromagnetic and two are antiferromagnetic in nature [120]. The first correction term in equation 7.2 describes the effect of finite thickness of the reference layer, the second term approximates the effect of the finite thickness of the soft magnetic layer.

The dependence of the Néel coupling on the finite thickness of the magnetic reference layer was experimentally verified and is shown in Fig. 7.7. Clearly, an increase of the rms–value (roughness) at the  $\text{Ru}-\text{Co}_{50}\text{Fe}_{50}$  interface by introducing Cu in the bottom electrode leads to an increased Néel coupling field at a fixed thickness of the  $\text{Co}_{50}\text{Fe}_{50}$ . The analysis of the fit to theory (Equation 7.2) is summarized in table 7.2.

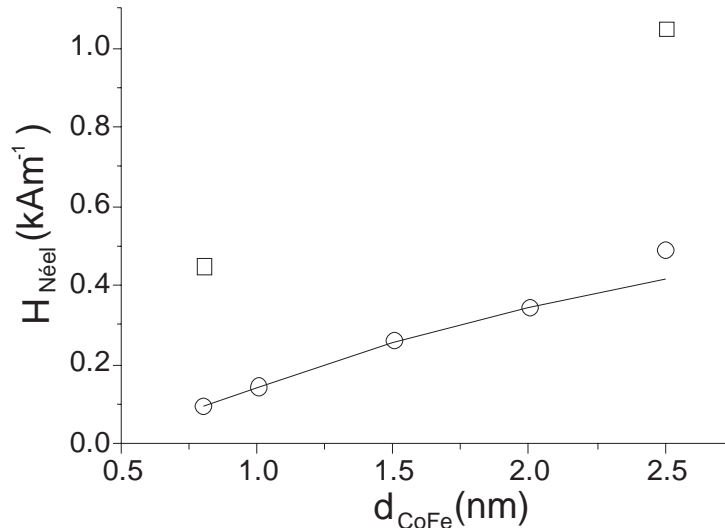


Figure 7.7: Measurement on a series of Ru25/Co<sub>50</sub>Fe<sub>50</sub> d<sub>Co<sub>50</sub>Fe<sub>50</sub></sub>/Al1.2 ox./NiFe6/Ta2/Ru3/Ta5 samples (○) with variable thickness of Co<sub>50</sub>Fe<sub>50</sub>. The Néel coupling field is plotted as a function of the thickness d<sub>Co<sub>50</sub>Fe<sub>50</sub></sub> of the Co<sub>50</sub>Fe<sub>50</sub> magnetic reference layer. (For comparison: Ru5/Cu30/Ru30/Co<sub>50</sub>Fe<sub>50</sub> d<sub>Co<sub>50</sub>Fe<sub>50</sub></sub>/Al1.2 ox./NiFe6/Ta5. (□)) The line is a fit to theory (equation 7.2).

#### Parameters used in the fit

|   |
|---|
| $M_S = 1320 \text{ kAm}^{-1}$ (VSM)                                 |
| Magnetization of the NiFe layer: $M_S = 800 \text{ kAm}^{-1}$ (VSM) |
| Dead layer of NiFe: 13 Å (VSM)                                      |
| $a_2$ (rms) = 1.3 Å – 1.5 Å (AFM)                                   |

#### Fitted parameters

| Fit  | Measured  |
|--|---|
| $\frac{a_1}{a_2} = 1.03$                                   | $\frac{a_1}{a_2} = 1.3$ (rms values measured by AFM)          |
| $\lambda = 21 \text{ nm}$                                  | $\lambda = 20 \text{ nm} - 25 \text{ nm}$ (measured by AFM)   |
| dead layer Co <sub>50</sub> Fe <sub>50</sub> : 3.8 Å       | dead layer Co <sub>50</sub> Fe <sub>50</sub> : 4 Å (from VSM) |
| thickness Al <sub>2</sub> O <sub>3</sub> : 1.5 nm – 2.2 nm | thickness Al, $d_{\text{Al}} = 1.2 \text{ nm}$                |

Table 7.2: Parameters used and gained by the fit of the Néel coupling to theory (Fig. 7.7). The AFM measurements were performed on a Ru25/Al1.2 ox. sample ( $\implies a_1$ ) and a Ru25/Co<sub>50</sub>Fe<sub>50</sub>1.5/Al1.2 ox. sample ( $\implies a_2$ ).

A number of parameters are used to fit the data of the Néel coupling versus the thickness of the Co<sub>50</sub>Fe<sub>50</sub> layer to equation 7.2. A dead layer is the difference between the nominal thickness and the thickness of the ferromagnetic part of a magnetic layer. Hence an error of the sputtering rate that leads to a thinner layer than the

nominally assumed contributes to the dead layer as well as an intermixing of magnetic and nonmagnetic material at the interfaces (e. g. Ta and NiFe) which leads to a not ferromagnetic material. Four parameters were optimized in order to achieve the best fit (nonlinear least square fit, NLSF). The thickness of the magnetic layers might be slightly different to the nominal thicknesses. This fact causes a small error of the parameters gained from the fit. The datapoint at  $d_{\text{Co}_{50}\text{Fe}_{50}} = 2.5$  nm was not considered in the fit and is interpreted as a "bad" charge which were sputtered occasionally. The result of the fit is summarized in table 7.2. The measured systematic can be described by theory, and also the values of the parameters gained from the fit are reasonable.

The thickness of the not ferromagnetic part (magnetic dead layer) of the  $\text{Co}_{50}\text{Fe}_{50}$  reference layer is one  $\text{Co}_{50}\text{Fe}_{50}$  layer and matches well with the measured value by VSM. The magnetic dead layer might be due to interdiffusion of Ru and  $\text{Co}_{50}\text{Fe}_{50}$  at the boundary, for instance. Furthermore, the wavelength of the interface roughness, which is essentially the grain size of the ruthenium, is confirmed by AFM and XRD (table 7.1) measurements.

The difference of the amplitudes  $a_1$  and  $a_2$  as measured by AFM is not reproduced by the best fit ( $\frac{a_1}{a_2}=1.03$ ). Since the Néel coupling field originates from the ferromagnetic part of the  $\text{Co}_{50}\text{Fe}_{50}$  layer but the AFM measurement is sensible to all material, the discrepancy can be explained by a smoothing of the ferromagnetic  $\text{Co}_{50}\text{Fe}_{50}$  layer roughness  $a_1$  due to interdiffusion of  $\text{Co}_{50}\text{Fe}_{50}$  and Ru and the interface.

The thickness of the  $\text{Al}_2\text{O}_3$  that separates the NiFe from the  $\text{Co}_{50}\text{Fe}_{50}$  is expected to be about 1.5 nm, the fit delivers a thickness in the range of 1.5 nm – 2.2 nm. The gained thickness of the  $\text{Al}_2\text{O}_3$  is very sensitive to the provided number of rms roughness. Since the peak to peak amplitude of the sinusoidal waviness in the model (equation 7.2) is an oversimplified picture of the real roughness approximated by the rms value, the fit-gained  $\text{Al}_2\text{O}_3$ -thickness can only be an approximation to the real thickness of the insulating layer. In contrast, the other parameters gained are relatively insensitive to the parameters used in the fit.

Conclusively, the thickness of the  $\text{Co}_{50}\text{Fe}_{50}$  layer can be used as a tool for tuning the Néel coupling.





# Chapter 8

## Magnetic stability

Magnetic stability of SDT elements means the preservation of the reference layers magnetization after repeated reversals of the magnetization of the soft magnetic layer. In a logic gate, magnetic stability has to be achieved for the lifetime of the device, which is conveniently expressed in switching cycles of the soft magnetic layer. For the application of SDT elements in magnetic random access memory (MRAM), different tunneling systems were investigated with respect to magnetic stability. Tunneling systems with an exchange biased reference layer system showed magnetic stability [55] [56] up to  $10^{13}$  switching cycles of the soft magnetic layer (uniaxial switching). Reference layer systems which are not pinned by an antiferromagnet were measured to be not magnetically stable, like a  $\text{Co}_{75}\text{Pt}_{12}\text{Cr}_{13}$  single layer and a Co/Cu/Co artificial antiferromagnet (AFi) [55] [121].

The decay of the reference electrodes magnetization were reported to be sensitive to the distance soft magnetic layer–reference layer ( $\text{Co}_{75}\text{Pt}_{12}\text{Cr}_{13}$ ) and to the material of the soft magnetic layer. Magnetic stray fields from domain walls incorporated in the soft magnetic layer were identified to demagnetize the reference layer [122] [123]. Indeed, no decay was measured, when the reversal of the soft magnetic layer was performed by coherent rotation. The decay with coherent rotation cycles reported in reference [121] was attributed to the instability of the Co/Cu/Co AFi itself.

As described earlier, the use of a programmable reference layer in spin–logic gates is favorable. Beside the programmable reference layer system Ru/CoFe, SDT elements with several reference layer systems were tested on magnetic stability with respect to their use in a spin–logic gate. The magnetic fields were generated by currents on–chip, the geometrical arrangement of the two magnetic field generating current lines and the SDT element investigated is shown in Fig. 8.1. The long axis of the SDT element is aligned along the  $x$ –axis. Hence a current density  $j_y$  generates a magnetic field along the easy axis of the SDT element ( $H_x$ ), as defined by the shape anisotropy of the soft magnetic layer. The second current line which allows to flow a current density along the  $x$ –axis is fabricated for the generation of the bias mag-

netic field ( $H_y$ ). A rotational magnetic field was generated by applying sinusoidal currents (current densities  $j_y$  and  $j_x$ , respectively) with a phase shift of 90 degrees and current amplitudes that lead to  $H_x$  and  $H_y$  of same amplitude.

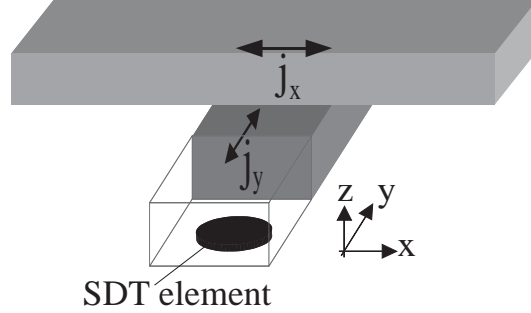


Figure 8.1: Geometrical arrangement of the magnetic field generating current lines and the SDT element. The current lines (cross section:  $10\mu m \times 0.5\mu m$ ) are electrically isolated from each other and from the SDT element. The SDT element and the first current line are separated by 60 nm of  $\text{SiO}_2$  and the two current lines themselves are separated by 500 nm of  $\text{SiO}_2$ .

Prior to each measurement of the magnetic stability, the reference layer system was saturated in a magnetic field of  $800 \text{ kAm}^{-1}$  along the long axis of the SDT element. The magnetic stability was determined by the measurement of the *TMR* in the minor loop as a function of the preceding number of switching cycles of the soft magnetic layer. The SDT elements were switched at frequencies up to 10 kHz. The peak to peak amplitude of the sinusoidal current signal was chosen to ensure switching of the soft magnetic layer twice per cycle but not switching of the hard magnetic layer system (especially Ru/CoFe). The measured switching stability did not depend on the frequency.

Figure 8.2 shows the magnetic stability for uniaxial switching along the long axis of five SDT elements (cycling of  $H_x$ ,  $H_y = 0$ ).

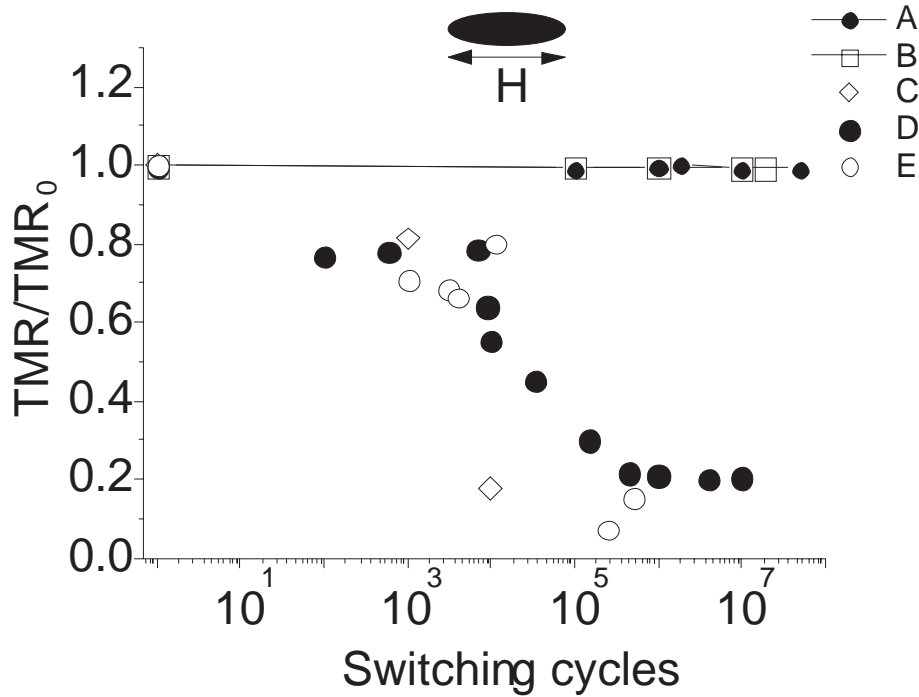


Figure 8.2: Measurement of the  $TMR$  of systems A–E versus the number of uniaxial switching cycles of the soft magnetic layer. The  $TMR$  is normalized to its value measured during the first switching cycle ( $TMR_0$ ). The decay of  $TMR$  is concluded to be due to the demagnetization of the reference layer.

The following SDT elements were investigated:

System A (eye  $3.6\mu\text{m} \times 0.9\mu\text{m}$ ):

Ta5/Cu30/TaN5/Ta9/NiFe3/IrMn7/Co<sub>50</sub>Fe<sub>50</sub>2/Ru0.8/Co<sub>50</sub>Fe<sub>50</sub>3/Al 1.2 ox./  
NiFe6/Ta5

System B (eye  $2.4\mu\text{m} \times 0.8\mu\text{m}$ ):

Ta5/Cu20/Ru5/Co<sub>50</sub>Fe<sub>50</sub>1.5/Ru0.9/Co<sub>50</sub>Fe<sub>50</sub>2.2/Al1.5 ox. /NiFe6/Ta2/Ru3/Ta5

System C (eye  $3.6\mu\text{m} \times 0.9\mu\text{m}$ ):

Ru20/Ta5/Ru10/Co<sub>50</sub>Fe<sub>50</sub>1/Al1.2 ox./NiFe5/Ta2/Ru3/Ta5

System D (eye  $2.8\mu\text{m} \times 0.7\mu\text{m}$ ):

Ru30/Co<sub>50</sub>Fe<sub>50</sub>1/Al1.2 ox./Co<sub>50</sub>Fe<sub>50</sub>1/NiFe5/Ta5

System E (elli  $3.2\mu\text{m} \times 0.8\mu\text{m}$ ):

Ru20/Ta5/Ru10/Co<sub>50</sub>Fe<sub>50</sub>1/Al1.2 ox./NiFe5/Ta2/Ru3/Ta5

System A represents an exchange biased AFi system, where the hard magnetic layer system cannot be programmed with a current on-chip. System B represents a pure AFi system which is reversed at  $80 \text{ kAm}^{-1}$ . C–E are tunneling systems with a Ru/Co<sub>50</sub>Fe<sub>50</sub> reference layer systems, which are switchable (programmable) by a current on-chip. For the SDT elements with sub- $\mu\text{m}$  width, the coercivity of Co<sub>50</sub>Fe<sub>50</sub> of systems C, E is in the regime of  $10 \text{ kAm}^{-1}$  and for system D it is in the regime of  $25 \text{ kAm}^{-1}$ , compared with about  $2 \text{ kAm}^{-1}$  for the soft magnetic layer. The results are shown in figure 8.2. The typical shape (respectively quality) of the minor loops from the SDT elements investigated is shown exemplarily for system E in Fig. 8.3 (a).

Up to  $10^7$  switching cycles, there is no measurable decay for the SDT element of the exchange biased AFi system A as well as for the SDT element of the pure AFi system B. While the result on the magnetic stability for the exchange biased AFi reference layer is expected from the result reported for an exchange biased single layer in reference [55], the magnetic stability of the Co<sub>50</sub>Fe<sub>50</sub>/Ru/Co<sub>50</sub>Fe<sub>50</sub> AFi is different to the results reported for an Co/Cu/Co AFi in reference [121].

The Co/Cu/Co AFi decayed in uniaxial cycling. That difference is explained by comparing the tunneling systems in more detail. Firstly, the distance between the Co<sub>50</sub>Fe<sub>50</sub>/Ru/Co<sub>50</sub>Fe<sub>50</sub> AFi and the soft magnetic NiFe layer is 50 % bigger than between the Co/Cu/Co AFi and the Co/NiFe soft magnetic layer. Secondly the magnitude of stray fields from Néel domain walls in Co<sub>1</sub>/NiFe<sub>6</sub> bilayers are stronger than in NiFe<sub>6</sub> due to the Co (additional magnetic material) Hence a higher magnetic stray field acts on the Co/Cu/Co AFi in reference [121] than on the Co<sub>50</sub>Fe<sub>50</sub>/Ru/Co<sub>50</sub>Fe<sub>50</sub> AFi investigated here [123]. Thirdly, the materials of the AFis compared are different (different coercivities, different strength of the coupling of the two magnetic layers, different grain sizes of the granular films). These differences lead to different magnetic stabilities of the pure AFis. Next, the size of the SDT elements investigated is different. In reference [121], the minimal width of the SDT elements is  $3 \mu\text{m}$  whereas for system B the (nominal) width is  $0.9 \mu\text{m}$ . Hence single domain like switching behaviour which excludes moving domain walls (and hence excludes one mechanism of demagnetization of a reference layer) is, at the first sight, energetically more favorable and hence more probable for system B than for the SDT elements investigated with the Co/Cu/Co AFi. Furthermore, the Co/Cu/Co AFi exhibited an intrinsic instability which was not measured for system B. Conclusively, it is not reliable to compare the experiments on magnetic stability reported in reference [121] and of system B in Fig. 8.2. In fact the experiments on the two AFi systems are different. Finally system B turned out to be magnetically stable, which is an important result.

Systems C–E with the programmable reference layer system Ru/Co<sub>50</sub>Fe<sub>50</sub> turned

out to be not magnetically stable during uniaxial switching. A difference between systems C, E and D cannot be concluded from the measurements in Fig. 8.2. The question on the origin of the demagnetization is answered, in accordance to references [55] [122] [123], by a rotational switching experiment.

The result on the magnetic stability of system E for rotational cycling of the soft magnetic layer is shown in Fig. 8.3 (c). The amplitudes of  $H_x$  and  $H_y$  were adjusted to be of equal magnitude and to be about a factor 0.1 bigger than the coercivity of system E ( $H_x=1.1 \cdot H_c \cdot \sin \omega \cdot t$ ,  $H_y=1.1 \cdot H_c \cdot \cos \omega \cdot t$ ).

The magnetic stability is drastically improved by rotational switching. After  $3 \cdot 10^7$  rotational switching cycles of the soft magnetic layer, the *TMR* is decreased by 3% (relative) from the initial *TMR*. Hence the origin of the demagnetization of the  $\text{Co}_{50}\text{Fe}_{50}$  reference layer during uniaxial switching as shown in figures 8.2 and 8.3 (b) is, according to the conclusions drawn in Ref. [122], due to moving domain walls occurring during the uniaxial reversal process of the NiFe soft magnetic electrode. Regarding spin–logic gates, magnetic stability with respect to rotational switching has to be considered. Magnetic stability up to at least  $10^7$  switching cycles was shown for systems A and B. For the programmable reference layer systems Ru/CoFe, the magnetic stability was exemplarily measured for system E up to  $10^7$  rotational switching cycles. However, the reference layer system Ru20/Ta5/Ru10/Co<sub>50</sub>Fe<sub>50</sub>1 (E) exhibited a slight intrinsic instability (Fig. 8.3 (c)).

Magnetic stability for the programmable reference layer system Ru/CoFe has been shown for up to  $10^7$  rotational switching cycles.

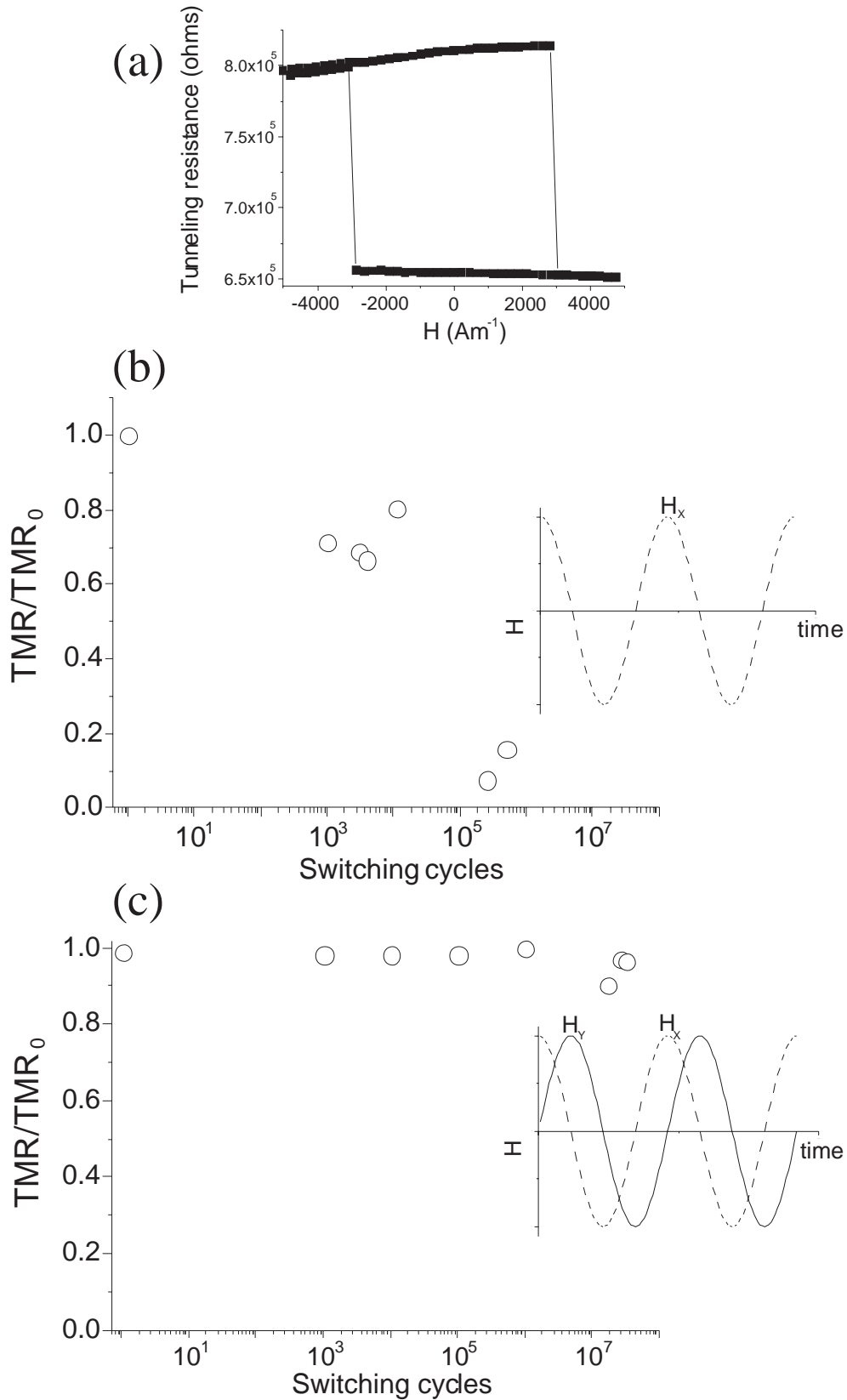


Figure 8.3: Magnetic stability of system E (Ru20/Ta5/Ru10/Co<sub>50</sub>Fe<sub>50</sub>1/Al1.2 ox./NiFe5/Ta2/Ru3/Ta5) (a) Minor loop (elli  $3.2\mu\text{m} \times 0.8\mu\text{m}$ ). (b) Measurement on magnetic stability for uniaxial switching along the long axis of the SDT element. (c) Result on the magnetic stability for rotational switching.







# Chapter 9

## Summary and outlook

Concepts of programmable digital logic based on spin dependent tunneling elements have been reviewed. Furthermore, own concepts of programmable digital logic have been introduced.

An infrastructure has been developed for fabricating and characterizing basic logic gates and single spin dependent tunneling elements.

The impact of shape anisotropy on the switching behaviour of the soft magnetic layers of SDT elements has been investigated. The measured astroids follows the theories of shape anisotropy and magnetostatic interactions within the tunneling stack. Deviations from the Stoner and Wohlfarth theory are explained by the incorporation of magnetic domains in the magnetization reversal process.

The programmable magnetic reference layer system Ru/Co<sub>50</sub>Fe<sub>50</sub> has been investigated. The measurements performed indicate that the high coercivity (up to 45 kAm<sup>-1</sup>) of Co<sub>50</sub>Fe<sub>50</sub> sputtered on Ru is due to its crystal structure impressed by the Ru-buffer.

The adjustability of the Néel coupling by the thickness of the reference layer has been successfully demonstrated.

The feasibility of basic logic gates realized with micron sized spin dependent tunneling elements has been shown for three different concepts.

The concept of spin-logic has been identified as a promising candidate for a commercial logic device.

The feasibility of spin–logic gates realized with micron sized SDT elements has been verified for the first time.

The perspective for the use of a programmable reference layer system in spin–logic gates is good, as concluded from the measured magnetic stability of the programmable Ru/CoFe reference layer system.

The perspective of spin–logic is still under investigation. A final judgement on the advantages and reliability of spin–logic is only possible if one draws conclusions of a FPGA–like complex logic circuit consisting of spin–logic gates and MRAM.

The breakthrough of spin–logic as a commercial product is closely connected to the success of MRAM. It will be probably seen in the next years, if the technological problems of MRAM are solvable.

# Bibliography

- [1] W. Thomson *Proc. R. Soc.*, vol. 8, p. 546, 1857.
- [2] M. N. Baibich, J. M. Broto, A. Fert, F. N. van Dau, F. Petroff, P. Eitenne, G. Creuzet, A. Friederich, and J. Chazelas *Phys. Rev. Lett.*, vol. 61, p. 2472, 1988.
- [3] G. Binasch, P. Grünberg, F. Saurenbach, and W. Zinn *Phys. Rev. B*, vol. 39, p. 4828, 1989.
- [4] S. S. P. Parkin *Phys. Rev. Lett.*, vol. 66, p. 3598, 1991.
- [5] S. A. Wolf, D. D. Awschalom, R. A. Buhrman, J. M. Daughton, S. von Molnár, M. L. Roukes, A. Y. Chtchelkanova, and D. M. Treger *Science*, vol. 294, p. 1488, 2001.
- [6] J. M. Daughton *J. Magn. Magn. Mater.*, vol. 66, p. 3598, 1999.
- [7] G. A. Prinz *Talk ME T1 Magnetoelectronics, Symposium on Metallic Multilayers, MML 01 Aachen, Germany*, 2001.
- [8] T. Miyazaki and N. Tezuka *J. Magn. Magn. Mater.*, vol. 139, p. L231, 1995.
- [9] J. S. Moodera, L. R. Kinder, T. M. Wong, , and R. Meservy *Phys. Rev. Lett.*, vol. 74, p. 3273, 1995.
- [10] S. S. P. Parkin, K. P. Roche, M. G. Samant, P. M. Rice, R. B. Beyers, R. E. Scheuerlein, E. J. O'sullivan, S. L. Brown, J. Bucchigano, D. W. Abraham, Y. Lu, M. Rooks, P. L. Trouilloud, R. A. Wanner, and W. J. Gallagher *J. Appl. Phys.*, vol. 85, p. 5828, 1999.
- [11] R. von Helmolt, J. Wecker, B. Holzapfel, L. Schultz, and K. Samwer *Phys. Rev. Lett.*, vol. 71, p. 2331, 1993.
- [12] A. Hubert and R. Schäfer, *Magnetic Domains*. Berlin: Springer, 1998.
- [13] N. P. Vasil'eva and S. I. Kasatkin *Russ. Microelectron.*, vol. 26, p. 406, 1997.

- [14] M. M. Hassoun, W. C. B. Jr., E. K. F. Lee, and R. L. Geiger *IEEE Tran. Magn.*, vol. 33, p. 3307, 1997.
- [15] J. Shen *IEEE Tran. Magn.*, vol. 33, p. 4492, 1997.
- [16] A. T. Hanbicki, R. Magno, S.-F. Cheng, Y. D. Park, A. S. Bracker, and B. T. Jonker *Appl. Phys. Lett.*, vol. 79, p. 1190, 2001.
- [17] R. Richter, H. Boeve, L. Bär, U. K. Klostermann, J. Wecker, and G. Reiss *J. Magn. Magn. Mater.*, vol. 240, p. 126, 2002.
- [18] R. Richter and J. Bangert *Patent Publication No. DE0010053206C1*, January 17, 2002.
- [19] R. Richter and J. Bangert *Patent Publication No. WO2002035704A1*, May 2, 2002.
- [20] R. Spitzer *Integrated Microelectronics Corporation, Berkeley, CA 94709*.
- [21] R. Richter and J. Wecker *Patent Publication No. DE0010113787C1*, September 5, 2002.
- [22] A. Franck, G. F. Marette, and B. I. Parsegyan *Proceedings of the eastern joint computer conference*, p. 28, 1959.
- [23] Datasheet ProAsic<sup>TM</sup> 500k Family, Core Logic Tile, Actel Corporation, Sunnyvale, CA 94086.
- [24] T. Gerrits, H. A. M. van den Berg, J. Hohlfeld, L. Bär, and T. Rasing *Nature*, vol. 418, p. 509, 2002.
- [25] W. C. Black, Jr., and B. Das *J. Appl. Phys.*, vol. 87, p. 6674, 2000.
- [26] W. Nolting, *Grundkurs: Theoretische Physik–Quantenmechanik, Teil 1*. Ulmen: Verlag Zimmermann–Neufang, 1994.
- [27] W. Nolting, *Grundkurs: Theoretische Physik–Quantenmechanik, Teil 2*. Ulmen: Verlag Zimmermann–Neufang, 1994.
- [28] J. G. Simmons *J. Appl. Phys.*, vol. 34, p. 1793, 1963.
- [29] J. G. Simmons *J. Appl. Phys.*, vol. 35, 1964.
- [30] J. G. Simmons *J. Appl. Phys.*, vol. 34, p. 2581, 1963.
- [31] W. F. Brinkman, R. C. Dynes, and J. M. Rowell *J. Appl. Phys.*, vol. 41, p. 1915, 1970.

- [32] J. J. Åkerman, R. Escudero, C. Leighton, S. Kim, D. A. Rabson, R. W. Dave, J. M. Slaughter, and I. K. Schuller *J. Magn. Magn. Mat.*, vol. 240, p. 86, 2002.
- [33] R. Meservey, P. M. Tedrow, and P. Fulde *Phys. Rev. Lett.*, vol. 25, p. 1270, 1970.
- [34] R. Meservey, P. M. Tedrow, and P. Fulde *Phys. Rev. Lett.*, vol. 26, p. 192, 1971.
- [35] M. Jullière *Phys. Lett.*, vol. 54, p. 225, 1975.
- [36] R. Meservey, P. M. Tedrow, and P. Fulde *Phys. Rev. B*, vol. 7, p. 318, 1973.
- [37] S. K. Upadhyay, A. Palanisami, R. N. Louie, and R. A. Buhrman *Phys. Rev. Lett.*, vol. 81, p. 3247, 1998.
- [38] J. Callaway and C. S. Wang *Phys. Rev. B*, vol. 7, p. 1096, 1983.
- [39] J. M. D. Teresa, A. Barthlmy, A. Fert, J. P. Contour, F. Montaigne, and P. Seneor *Science*, vol. 286, p. 507, 1999.
- [40] J. S. Moodera and G. Mathon *J. Magn. Mat.*, vol. 200, p. 248, 1999.
- [41] J. C. Slonczewski *Phys. Rev. B*, vol. 39, p. 6995, 1989.
- [42] L. D. Landau and E. Lifshitz *Phys. Z. Sowjetunion*, vol. 8, p. 153, 1935.
- [43] R. H. Koch, G. Grinstein, G. A. Keefe, Y. Lu, P. L. Trouilloud, W. J. Gallagher, and S. S. P. Parkin *Phys. Rev. Lett.*, vol. 84, p. 5419, 2000.
- [44] S. Ingvarsson, G. Xiao, S. S. P. Parkin, W. J. Gallagher, G. Grinstein, and R. H. Koch *Phys. Rev. Lett.*, vol. 85, p. 3289, 2000.
- [45] W. F. B. Jr. *Phys. Rev.*, vol. 58, p. 736, 1940.
- [46] M. Donahue and D. Porter, “Oommf,” <http://math.nist.gov/oommf/>, 2002.
- [47] M. R. Scheinfein, “Landau–lifshitz–gilbert micromagnetics simulator,” <http://llgmicro.home.mindspring.com/>, 2001.
- [48] E. C. Stoner and E. P. Wohlfarth *Philos. Trans. R. Soc. London, Ser. A*, vol. 240, p. 599, 1948.
- [49] L. Néel *Comptes. Rendus*, vol. 255, p. 1676, 1962.
- [50] S. Cardoso, P. P. Freitas, C. de Jesus, P. Wei, and J. C. Soares *Appl. Phys. Lett.*, vol. 76, p. 610, 2000.
- [51] T. Dimopoulos, C. Tiusan, V. da Costa, and K. Ounadjela *Appl. Phys. Lett.*, vol. 77, p. 3624, 2000.
- [52] J. Schmalhorst, H. Brückl, G. Reiss, M. Vieth, G. Gieres, and J. Wecker *J. Appl. Phys.*, vol. 87, p. 5191, 2000.

- [53] T. Dimopoulos, C. Tiusan, K. Ounadjela, M. Hehn, H. A. M. van den Berg, Y. Henry, and V. da Costa *J. Appl. Phys.*, vol. 87, p. 4685, 2000.
- [54] J. Wecker private communication, 2002.
- [55] S. Gider, B.-U. Runge, A. C. Marley, and S. S. P. Parkin *Science*, vol. 281, p. 797, 1998.
- [56] R. Richter, L. Bär, J. Wecker, and G. Reiss *J. Appl. Phys.*, vol. 91, p. 8402, 2002.
- [57] U. K. Klostermann, *Submicrometer sized magnetic tunnel junctions*. PhD thesis, University of Regensburg, Department of Physics, 2001.
- [58] H. van den Berg, W. Clemens, G. Gieres, G. Rupp, M. Vieth, J. Wecker, and S. Zoll *J. Magn. Magn. Mat.*, vol. 165, p. 524, 1997.
- [59] P. Günberg, R. Schreiber, Y. Pang, M. B. Brodsky, and H. Sowers *Phys. Rev. Lett.*, vol. 57, p. 2442, 1986.
- [60] S. S. P. Parkin, N. More, and K. P. Roche *Phys. Rev. Lett.*, vol. 64, p. 2304, 1990.
- [61] N. Persat, H. A. M. van den Berg, and A. Dinia *J. Magn. Magn. Mat.*, vol. 165, p. 446, 1997.
- [62] T. Dimopoulos, *Transport Polarisé en Spin dans les Jonctions Tunnel Magnétiques: Le Rôle des Interfaces Métal/Oxyde dans le Processus Tunnel*. PhD thesis, L'Université Louis Pasteur de Strasbourg, 2002.
- [63] H. Boeve, L. Esparbe, G. Gieres, L. Bär, H. Brückl, and J. Wecker *J. Appl. Phys.*, vol. 91, p. 7962, 2002.
- [64] R. S. Sousa, J. J. Sun, V. Soares, P. P. Freitas, A. Kling, M. F. da Silva, and J. C. Soares *Appl. Phys. Lett.*, vol. 73, p. 3288, 1998.
- [65] H. Boeve, J. D. Boeck, and G. Borghs *J. Appl. Phys.*, vol. 89, p. 482, 2001.
- [66] S. Cardoso, V. Gehanno, R. Ferreira, and P. P. Freitas *IEEE Trans. Magn.*, vol. 35, p. 2952, 1999.
- [67] J.-P. Hwang, J.-C. Wu, and F. B. Humphrey *IEEE Trans. Magn.*, vol. 22, p. 217, 1986.
- [68] R. J. Spain and H. I. Jauvtis *J. Appl. Phys.*, vol. 38, p. 1201, 1967.
- [69] R. J. Spain and H. I. Jauvtis *J. Appl. Phys.*, vol. 37, p. 2584, 1966.
- [70] R. P. Cowburn and M. E. Welland *Science*, vol. 287, p. 1466, 2000.
- [71] R. P. Cowburn, D. A. Allwood, G. Xiong, and M. D. Cooke *J. Appl. Phys.*, vol. 91, p. 6949, 2002.

- [72] D. A. Allwood, G. Xiong, M. D. Cooke, C. C. Faulkner, D. Atkinson, and N. V. and R. P. Cowburn *Science*, vol. 296, p. 2003, 2002.
- [73] M. Johnson, B. R. Bennett, M. J. Yang, M. M. Miller, and B. V. Shanabrook *Appl. Phys. Lett.*, vol. 71, p. 974, 1997.
- [74] M. Johnson, B. R. Bennett, P. R. Hamar, and M. M. Miller *Solid State Electronics*, vol. 44, p. 1099, 2000.
- [75] E. Goto *Proceedings of the IRE*, vol. August, p. 1304, 1959.
- [76] C.-Y. You and S. D. Bader *J. Appl. Phys.*, vol. 87, p. 5215, 2000.
- [77] M. Johnson *IEEE Trans. Magn.*, vol. 36, p. 2758, 2000.
- [78] D. Wang, M. Tondra, A. V. Pohm, C. Nordman, J. Anderson, and J. M. Daughton *J. Appl. Phys.*, vol. 87, p. 6385, 2000.
- [79] L. I. Maissel and R. Glang, *Handbook of Thin Film Technology*. New York: McGraw–Hill, 1983.
- [80] L. Bär *private communication*, 2001.
- [81] M. S. Rzchowski and X. W. Wu *Phys. Rev. B*, vol. 61, p. 5884, 2000.
- [82] R. J. Pederson and F. L. Vernon *Appl. Phys. Lett.*, vol. 10, p. 29, 1967.
- [83] J. C. Lee, I. Chen, and C. Hu *IEEE Trans. Electron Devices*, vol. 35, p. 2268, 1988.
- [84] A. Olbrich, B. Ebersberger, and C. Boit *Appl. Phys. Lett.*, vol. 73, p. 3114, 1998.
- [85] A. Olbrich, B. Ebersberger, C. Boit, J. Vancea, H. Hoffmann, H. Altmann, G. Gieres, and J. Wecker *Appl. Phys. Lett.*, vol. 78, p. 2934, 2001.
- [86] Y. Ando, H. Kameda, H. Kubota, and T. Miyazaki *J. Appl. Phys.*, vol. 87, p. 5206, 2000.
- [87] Bronstein, Semendjajew, Musiol, and Mühlig. Thun und Frankfurt am Main: Verlag Harri Deutsch, 1993.
- [88] J. H. Lee, I.-W. Chang, S. J. Byun, T. K. Hong, K. Rhie, W. Y. Lee, K.-H. Shin, C. Hwang, S. S. Lee, and B. C. Lee *J. Magn. Magn. Mat.*, vol. 240, p. 137, 2002.
- [89] W. Nolting, *Grundkurs: Theoretische Physik–Elektrodynamik*. Ulmen: Verlag Zimmermann–Neufang, 1993.
- [90] J. A. Osborn *Phys. Rev.*, vol. 67 (11, 12), p. 351, 1945.
- [91] A. Hubert and R. Schäfer, *Magnetic Domains Equation 3.23*. Berlin: Springer, 1998.

- [92] K. J. Kirk, J. N. Chapman, and C. D. W. Wilkinson *J. Appl. Phys.*, vol. 85, p. 5237, 1999.
- [93] M. Rührig, B. Khamsehpour, K. J. Kirk, J. N. Chapman, P. Aitchison, S. McVitie, and C. D. W. Wilkinson *IEEE Trans. Magn.*, vol. 32, p. 4452, 1996.
- [94] J. Shi, T. Zhu, M. Durlam, S. Tehrani, Y. F. Zheng, and J.-G. Zhu *IEEE Trans. Magn.*, vol. 34, p. 997, 1998.
- [95] T. Kimura, F. Wakaya, and K. Gamo *Jpn. J. Appl. Phys.*, vol. 40, p. 6357, 2001.
- [96] J. Gadbois, J.-G. Zhu, W. Vavra, and A. Hurst *IEEE Trans. Magn.*, vol. 34, p. 1066, 1998.
- [97] A. Anguelouch, B. D. Schrag, G. Xiao, Y. Lu, P. L. Trouilloud, R. A. Wanner, W. J. Gallagher, and S. S. P. Parkin *Appl. Phys. Lett.*, vol. 76, p. 622, 2000.
- [98] C. L. Platt, M. R. McCartney, F. T. Parker, and A. E. Berkowitz *Phys. Rev. B*, vol. 61, p. 9633, 2000.
- [99] X. Portier and A. K. Petford-Long *Appl. Phys. Lett.*, vol. 76, p. 754, 2000.
- [100] J. D. Jackson, *Classical Electrodynamics, Second Edition*. New York: Wiley, 1975.
- [101] S. Therani, M. Durlam, M. DeHerrera, J. M. Slaughter, N. Rizzo, B. Engel, and G. Grynkowich presented at the 46th Conference on Magnetism and Magnetic Materials, Session BZ-01, Seattle, 2001.
- [102] H. A. M. van den Berg private communication, 2000.
- [103] Webelements <http://www.webelements.com/webelements/elements/text/Ru/xtal.html>.
- [104] M. Pakala, Y. Huai, G. Anderson, and L. Miloslavsky *J. Appl. Phys.*, vol. 87, p. 6653, 2000.
- [105] K. Bal private communication, 2001.
- [106] K. Kopitzki, *Einführung in die Festkörperphysik*. Stuttgart: B. G. Teubner Verlag, 1993.
- [107] S. Heitmann and H. Brückl private communication, 2001.
- [108] International Centre for Diffraction Data – Powder Diffraction, <http://www.icdd.com/>, 2002.
- [109] G. Gieres, CT MM1, Siemens AG, private communication, 2002.
- [110] A. Rucki CT MM7, Siemens AG, private communication, 2001.



- [111] N. W. Ashcroft, *Solid State Physics*. Fort Worth: Saunders College Publishing, 1976.
- [112] Y.-P. Zhao, R. M. Gamache, G.-C. Wang, T.-M. Lu, G. Palasantzas, and J. T. M. D. Hosson *J. Appl. Phys.*, vol. 89, p. 1325, 2001.
- [113] R. M. Bozorth, *Ferromagnetism*. New York: The institute of electrical and electronics engineers, Inc., 1993.
- [114] K. J. Davies, S. Wells, R. V. Upadhyay, S. W. Charles, K. O'Grady, M. E. Hilo, T. Meaz, and S. Mørup *J. Magn. Magn. Mater.*, vol. 149, p. 14, 1995.
- [115] M. Dumm, M. Zöfl, R. Moosbühler, M. Brockmann, T. Schmidt, and G. Bayreuther *J. Appl. Phys.*, vol. 87, p. 5457, 2000.
- [116] F. Perjeru, M. M. Schwickert, T. Lin, A. Anderson, and G. R. Harp *Phys. Rev. B*, vol. 61, p. 4054, 2000.
- [117] M. C. Saint-Lager, D. Raoux, M. Brunel, M. Piecuch, E. Elkaim, and J. P. Lauriat *Phys. Rev. B*, vol. 51, p. 2446, 1995.
- [118] D. Spišák, R. Lorenz, and J. Hafner *Phys. Rev. B*, vol. 63, 2001.
- [119] J. Zhang and R. M. White *IEEE Trans. Magn.*, vol. 32, p. 4630, 1996.
- [120] J. C. S. Kools and W. Kula *J. Appl. Phys.*, vol. 85, p. 4466, 1999.
- [121] J. Schmalhorst, H. Brückl, G. Reiss, R. Kinder, G. Gieres, and J. Wecker *Appl. Phys. Lett.*, vol. 77, p. 3456, 2000.
- [122] M. R. McCartney, R. E. Dunin-Borkowski, M. R. Scheinfein, D. J. Smith, S. Gider, and S. S. P. Parkin *Science*, vol. 286, p. 1337, 1999.
- [123] L. Thomas, M. G. Samant, and S. S. P. Parkin *Phys. Rev. Lett.*, vol. 84, p. 1816, 2000.



## Curriculum Vitae

Ralf Richter

Geschwister-Scholl-Str. 10

91058 Erlangen

Born in Fulda (Germany), April 27, 1973

|             |  |
|-------------|--|
| 1979–1983   | Grundschule Florenberg (Primary School)                    |
| 1983–1992   | Marianum Fulda (Secondary School and High School)          |
| 05/92       | Allgemeine Hochschulreife                                  |
| 07/92–06/93 | Obligatory military service                                |
| 11/93–03/99 | Physics at the University of Würzburg                      |
| 08/96–08/97 | Physics at the State University of New York, Buffalo, USA  |
| 07/99–08/02 | PhD student (University of Bielefeld, Siemens AG Erlangen) |
| 09/97       | Degree: Master of Arts (M.A.) in Physics                   |
| 03/99       | Degree: Diplom-Physiker Univ.                              |



## List of publications and presentations

- M. J. Naughton, J. P. Ulmet, A. Narjis, S. Askenazy, M. V. Chaparala, R. Richter. "Demonstration of cantilever magnetometry in pulsed magnetic fields", *Physica B*, Volume 246–247 (1998), page 125
- R. Richter, K. Attenkofer, W. A. Caliebe. "Non-resonant magnetic X-ray diffraction of ferromagnetic EuO", HasyLab annual report (1998)
- K. Attenkofer, W. A. Caliebe, R. Richter. "XMCD magnetometer measurements in the hard X-ray regime on a Gd-metal foil", HasyLab annual report (1998)
- Talk at the 4<sup>th</sup> International Symposium on Metallic Multilayers (MML 01), Aachen, June 2001. "Field programmable spin-logic realized with tunnelmagnetoresistance devices"
- Talk at the 46<sup>th</sup> annual Conference on magnetism and magnetic materials (MMM), Seattle, November 2001. "Field programmable spin-logic gates"
- R. Richter, L. Bär, J. Wecker, G. Reiss. "Nonvolatile spin-logic for reconfigurable computing", *Applied Physics Letters*, Volume 80 (2002), page 1291.  
Response to this article:  
⇒ *Electronic Engineering Times*, February 22 2002  
⇒ *Cern Courier*, Volume 42 (2002), No. 3  
⇒ *MRS Bulletin*, March 2002
- Poster at the 269. WE-Heraeus-Seminar, Bad Honnef, January 2002.
- Talk at the Frühjahrstagung der Deutschen Physikalischen Gesellschaft, Regensburg, March 2002.
- R. Richter, H. Boeve, L. Bär, J. Bangert, G. Rupp, G. Reiss, J. Wecker. "Field programmable spin-logic realized with tunnelling-magnetoresistance devices", *Solid State Electronics*, Volume 46 (2002), page 639.
- R. Richter, L. Bär, J. Wecker, G. Reiss. "Tunneling systems for field programmable spin-logic gates", *Journal of Applied Physics*, Volume 91 (2002), page 8402.
- R. Richter, H. Boeve, L. Bär, U. K. Klostermann, J. Wecker, G. Reiss. "Field programmable spin-logic based on magnetic tunnelling elements", *Journal of Magnetism and Magnetic Materials*, Volume 240 (2002), page 126.
- 4 patents submitted (1999–2001)